I-53134

SERI/STR-211-3230
DE88001122

November 1987

DR-0374-3

Cadmium Sulfide/Copper Ternary Heterojunction Cell Research

Final Subcontract Report
1 October 1984-31 May 1987

W.E. Devaney
R.A. Mickelsen
W.S. Chen
B.J. Stanbery
J.M. Stewart
F.W. Lytle
A.F. Burnett
Boeing High Technology Center
Seattle, Washington

Prepared under Subcontract No. ZL-4-04068-1

SERI

Solar Energy Research Institute
A Division of Midwest Research Institute

1617 Cole Boulevard
Golden, Colorado 80401-3393

Operated for the
U.S. Department of Energy
under Contract No. DE-AC02-83CH10093

DISTRIBUTION OF THIS DOCUMENT IS UNLIMITED

DISCLAIMER

This report was prepared as an account of work sponsored by an agency of the United States Government. Neither the United States Government nor any agency thereof, nor any of their employees, makes any warranty, express or implied, or assumes any legal liability or responsibility for the accuracy, completeness, or usefulness of any information, apparatus, product, or process disclosed, or represents that its use would not infringe privately owned rights. Reference herein to any specific commercial product, process, or service by trade name, trademark, manufacturer, or otherwise does not necessarily constitute or imply its endorsement, recommendation, or favoring by the United States Government or any agency thereof. The views and opinions of authors expressed herein do not necessarily state or reflect those of the United States Government or any agency thereof.

DISCLAIMER

Portions of this document may be illegible in electronic image products. Images are produced from the best available original document.

SERI/STR--211-3230

DE88 001122

Cadmium Sulfide/Copper Ternary Heterojunction Cell Research

Final Subcontract Report
1 October 1984-31 May 1987

W.E. Devaney
R.A. Mickelsen
W.S. Chen
B.J. Stanbery
J.M. Stewart
F.W. Lytle
A.F. Burnett
Boeing High Technology Center
Seattle, Washington

MASTER

November 1987

SERI Technical Monitor: H.S. Ullal

Prepared under Subcontract No. ZL-4-04068-1

Solar Energy Research Institute
A Division of Midwest Research Institute

1617 Cole Boulevard
Golden, Colorado 80401-3393

Prepared for the
U.S. Department of Energy
Contract No. DE-AC02-83CH10093

DISCLAIMER

This report was prepared as an account of work sponsored by an agency of the United States Government. Neither the United States Government nor any agency thereof, nor any of their employees, makes any warranty, express or implied, or assumes any legal liability or responsibility for the accuracy, completeness, or usefulness of any information, apparatus, product, or process disclosed, or represents that its use would not infringe privately owned rights. Reference herein to any specific commercial product, process, or service by trade name, trademark, manufacturer, or otherwise does not necessarily constitute or imply its endorsement, recommendation, or favoring by the United States Government or any agency thereof. The views and opinions of authors expressed herein do not necessarily state or reflect those of the United States Government or any agency thereof.

EB

NOTICE

This report was prepared as an account of work sponsored by the United States Government. Neither the United States nor the United States Department of Energy, nor any of their employees, nor any of their contractors, subcontractors, or their employees, makes any warranty, expressed or implied, or assumes any legal liability or responsibility for the accuracy, completeness or usefulness of any information, apparatus, product or process disclosed, or represents that its use would not infringe privately owned rights.

Printed in the United States of America
Available from:
National Technical Information Service
U.S. *Department of Commerce*
5285 Port Royal Road
Springfield, VA 22161

Price: Microfiche A01
Printed Copy A07

Codes are used for pricing all publications. The code is determined by the number of pages in the publication. Information pertaining to the pricing codes can be found in the current issue of the following publications, which are generally available in most libraries: *Energy Research Abstracts, (ERA); Government Reports Announcements* and Index (*GRA* and I); *Scientific and Technical Abstract Reports (STAR);* and publication, NTIS-PR-360 available from NTIS at the above address.

Abstract

This is the Final Technical Progress Report on a thirty-two month research program on $CuInSe_2$ and $CuInGaSe_2$ based thin-film polycrystalline heterojunction solar cells. $CuInGaSe_2$ films incorporating Ga fractions (x in $CuIn_{1-x}Ga_xSe_2$) from 0.04 to 1.0 have been prepared and characterized. $CuInGaSe_2$/CdZnS heterojunction devices have been fabricated for a range of Ga contents and show the expected variations in Voc and spectral response with Ga content. An efficiency of 10.2% (SERI test, ASTM87) has been measured for a cell with Ga fraction of 0.23, the highest efficiency reported for this material. A $CuInSe_2$/CdZnS monolithically interconnected four cell series string of 91 cm^2 area has been fabricated with a total area efficiency of 9.5% (SERI test, ASTM87). Results are presented on Ion-Assisted Deposition of the selenide and sulfide, on a new design for the Se evaporation source, on ITO reactive sputter deposition, and on CdZnS films prepared from an E-Gun Evaporation source. Spectral Response and I-V characteristic variations with selenide composition before and after heat-treatment are discussed for the $CuInSe_2$/CdZnS devices. The highest AM1 total area efficiency for the $CuInSe_2$/CdZnS cell is now 11.9% (Boeing test, AM1 spectrum) with five cells measured over the previously reported high of 10.9%. Room Temperature Photoluminescence, Voltage Contrast Imaging of junction cross sections, Raman Spectroscopy, and EXAFS measurements on the $CuInSe_2$/CdZnS devices are also presented and discussed.

TABLE OF CONTENTS

6.0 Appendices

LIST OF FIGURES

LIST OF FIGURES(cont.)

LIST OF TABLES

1.0 SUMMARY

This is the Final Technical Progress Report of a thirty-two month research program entitled "Cadmium Sulfide/Copper Ternary Heterojunction Cell Research." It covers the period October 1, 1984 through May 31, 1987. The work was supported under SERI Contract ZL-4-04068. This contract continues the work done under several previous contracts (1-5) and has been the subject of five interim reports (6-10).

The work reported here has resulted in six published papers by the principal research group (11-16) as well as one dissertation (17), two theses (18,19), and several published papers by the subcontractors.

The system used to prepare the $CuInGaSe_2$ films has been essentially rebuilt during the contract period, replacing the large planetary fixturing with a small rotating substrate holder. This has allowed much improved control of the selenide deposition process at the higher temperatures (550°C - 600°C) needed for the gallium containing films

The mixed selenide cells continued to improve in efficiency. During this contract the largest number of $CuInGaSe_2$ films and $CuInGaSe_2$/CdZnS devices were made using films containing 23% Ga ($x = 0.23$ in $CuIn_{1-x}Ga_xSe_2$). The best of these 23% Ga cells, after antireflection coating, measured 10.6% in tests at Boeing and 10.2% in tests under standard conditions (ASTM85 or ASTM87, 100 mW/cm^3) at SERI. This is essentially the same efficiency as SERI tests of the best $CuInSe_2$/CdZnS under the same test conditions. Pushing to higher Ga contents and further film quality and device structure improvements are expected to result in still higher values for the $CuInGaSe_2$ based cells. An absorption edge value near 1.14 eV was obtained from spectral response measurements for these films.

Films and devices were also made over a range of Ga contents but primarily at x values of 0.25, 0.50 and 1.0. This data along with data previously taken showed a relationship

$$E_g = 1.00 + 0.67x + 0.14x(x-1) \qquad [eV]$$

for the band gap variation of the $CuIn_{1-x}Ga_xSe_2$ with composition. Voc variation showed the expected increase with Ga content and bandgap but no simple relationship was observed.

Major problems with adhesion and electrical contact properties are still being encountered at the Mo/Selenide interface in these devices. I-V characteristics in high Ga content devices show extremely poor diode characteristics. This behavior has been assumed related to these contact problems, however no direct proof of this exists.

One major goal of this program was the demonstration of 9.0% efficient, large (near 100 cm^2) area $CuInSe_2$/CdZnS devices. This has been done by using a novel monolithically integrated four cell series string design. In addition these high efficiency (9.5%) cells were fabricated on low cost glass substrates and used a design scalable to even larger sizes without increased area dependent losses. Fabrication of 20 cm^2 (2x2 inch square, two series connected elements) and 90 cm^2 (4x4 inch square, four series connected elements) $CuInSe_2$ cells is described in section 3.2 below, in appendix D, and in the previous contract reports (8-10). The best 4 x 4 inch cell was measured as 9.5% efficient in both tests at Boeing and tests under standard conditions at SERI. If the end collector tab area is included for the device, thereby fulfilling the SERI "module" definition, the efficiency is 9.1% for this device.

Several Basic Measurement tasks were undertaken under this contract. The low temperature (12°K) Photoluminescence measurements made under the previous contract were extended to room temperature. However only broad emission peaks were seen in all samples investigated, with no apparent correlation with film properties.

Voltage Contrast Imaging of junction cross sections was used as a complementary measurement to the normal EBIC studies to determine the location and motion of the electric field region in the device. Good voltage contrast could be obtained with the sample at 1 to 5 volts reverse bias. In direct comparisons the equivalence of the Voltage Contrast and EBIC techniques were shown. On the major question of junction location our studies demonstrated the voltage transition region in efficient $CuInSe_2$/CdZnS devices to be within the system measurement error (0.15-0.5μm) of the metallurgical junction between the sulfide and selenide. However, in devices without the normal oxygen heat treatment many of the effects seen in the EBIC on similar samples could be reproduced

Studies of the short range ordering in these materials are considered extremely important, especially for the $CuInGaSe_2$. We have attempted to explored these questions through two methods, Raman Spectroscopy and Extended X-Ray Absorption

Fine Structure (EXAFS). Initial Raman Scattering data have been taken on the $CuInSe_2$ films and on a p-type single crystal $CuInSe_2$ sample. These initial data are limited by poor signal to noise ratios and by experimental artifacts. However two possible $CuInSe_2$ lines have been identified.

We are exploring the new techniques of X-Ray Absorption measurements and of Extended X-Ray Absorption Fine Structure (EXAFS) in conjunction with Farrel W. Lytle of the Boeing Physics Technology Laboratory. His introduction to the techniques and discussion of initial results are contained in Appendix C.

Ion-Assisted deposition of the $CuInSe_2$ films, ion etching of the selenide prior to sulfide deposition, and ion-assisted deposition of the sulfide and of ITO films have all been explored using an Ion-Tech Ion Beam Source mounted in the selenide and sulfide deposition chambers. These subjects are discussed in section 3.8 below and in several previous reports (6,7,9,10).

CdZnS and CdS films have been prepared by direct evaporation of the mixed sulfide powder using the newly installed E-gun evaporation source. Good optical and structural quality and excellent uniformity have been obtained. However, in both cases the films prepared were of higher resistivity than those produced by thermal evaporation from apertured crucibles.

Spectral Response and I-V characteristic data have been obtained for a set of $CuInSe_2$ cells with deliberately varied selenide composition. Curves were taken both with the cells in the as-fabricated state and after the normal 225°C heat treatment in oxygen. The data clearly show a loss in spectral response in the long wavelength region and corresponding short circuit current loss with long heat treatment. This long wavelength response loss is strongly dependent on the selenide composition.

As a result of the continued development of the $CuInSe_2$/CdZnS devices the best device efficiency measured at Boeing increased from the 10.9% of the previous contract to 11.9% as measured at Boeing. This increase was not reflected in any appreciable increase in the efficiency as measured at SERI for several reasons, including problems with area definition and measurement, and changes in the standard test conditions. These devices are discussed below.

Reports from two subcontractors, A. Rothwarf of Drexel University and L. C. Olsen of the Joint Center for Graduate

Study/University of Washington have been included in previous reports under this contract (6-10). These reports detail the results of the individual one year contracts on modeling of the $CuInSe_2/CdZnS$ devices.

Data sheets for the $CuInSe_2$ and $CuInGaSe_2$ films and devices delivered to SERI over the period of the contract have also been included in the previous contract reports. These give both preparation and performance data and can be referred to for a good cross section of the samples made during this contract period.

2.0 INTRODUCTION

This is the Final Technical Progress Report of a two year research program entitled "Cadmium Sulfide/Copper Ternary Heterojunction Cell Research." This work continues the research done under several previous contracts (1-5) and focuses on further development of thin-film polycrystalline heterojunction solar cells using Copper Indium Diselenide ($CuInSe_2$) or the mixed alloy Copper Indium Gallium Diselenide ($CuIn_{1-x}Ga_xSe_2$) as the p-type layer and Cadmium Sulfide (CdS) or the mixed alloy Cadmium Zinc Sulfide ($Cd_{1-z}Zn_zS$) as the n-type layer.

As a result of the previous work done at Boeing, an 11% efficient (AM1 Spectrum) $CuInSe_2$/CdZnS thin-film polycrystalline solar cell has been experimentally demonstrated. These cells have been subjected to severe life-testing and have been found to be stable over thousands of test hours. A simple, high rate deposition process has been developed for the selenide using vacuum evaporation from elemental sources, making this an attractive technology for large area applications.

The general goals of the present program were to further improve the efficiency of these cells and to develop improved preparation processes for them. The specific objectives of the program included:

- Preparation and evaluation of $CuIn_{1-x}Ga_xSe_2$/CdZnS cells
- Preparation of $CuInSe_2$ films and $CuInSe_2$/CdZnS cells by ion-assisted deposition processes
- Assessment of Se vapor species effects during $CuInSe_2$ film deposition
- Investigation of alternative n-type window materials
- Studies of interface states and defect levels
- Alternate selenide and sulfide deposition technique investigations
- Development of film/cell analytical measurement methods
- Demonstrate large (20-100 cm^2), high-efficiency (9%) cells

- o Theoretical Modeling of cell performance
- o Attainment of greater than 13% efficiencies

These objectives have been discussed individually in the five reports issued under this contract (6-10). Results obtained during this contract are also discussed in detail in these five reports.

As part of the theoretical modeling effort in this contract, two subcontracts have been included for the first year of the contract, one with Professor L. C. Olsen of the Joint Center for Graduate Studies, University of Washington and a second with Professor A. Rothwarf of Drexel University.

3.0 TECHNICAL DISCUSSION

3.1 $CuInGaSe_2$ Films and Devices

3.1.1 Preparation

During the past contract period the $CuInGaSe_2$ deposition process has undergone a number of significant changes. At the start of the contract the planetary system had a commercially manufactured substrate holder system capable of holding a large number of substrates and using true planetary (epicyclic) motion. To heat the large area involved, a total of 8 kW of power was required. This resulted in high heat loads throughout the deposition system and interfered with accurate monitoring of the deposition rates. Se rates could not be monitored accurately with a quartz crystal monitor due to heating of the detector and re-evaporation of the Se from the detector. Additional problems encountered with the original approach were severe limitations on how quickly the substrates could be heated, and the rather lengthy time to cool.

Additional significant changes were made to the evaporation sources for the Cu,Ga and In. The original sources were alumina coated tungsten boats. These were subject to a rapid loss of the Al_2O_3 barrier-coating and to distortion upon heating.

The present $CuInGaSe_2$ deposition chamber is shown schematically in Fig. 3.1-1. The system is pumped by a CHA Model SE-1000 system with a 10 inch diffusion pump rated at 5300 l/sec.

The large substrate area originally used has now been reduced to a 7 inch diameter flat plate rotating about a single fixed axis. Two substrates are heated by 4 quartz lamps situated on the back side of the rotating substrate holder. Direct radiant heating of the substrates occurs through openings in the substrate holder onto the back side of the substrates. If desired the substrates can reach a temperature of 450°C in less than 5 minutes. With the present configuration, substrate temperatures can approach 600°C. The substrate temperature is calibrated by placing a partially selenide coated substrate into the holder with the selenide coating facing the deposition sources. A thermocouple is fastened to the selenide film. While the substrate is being heated, the

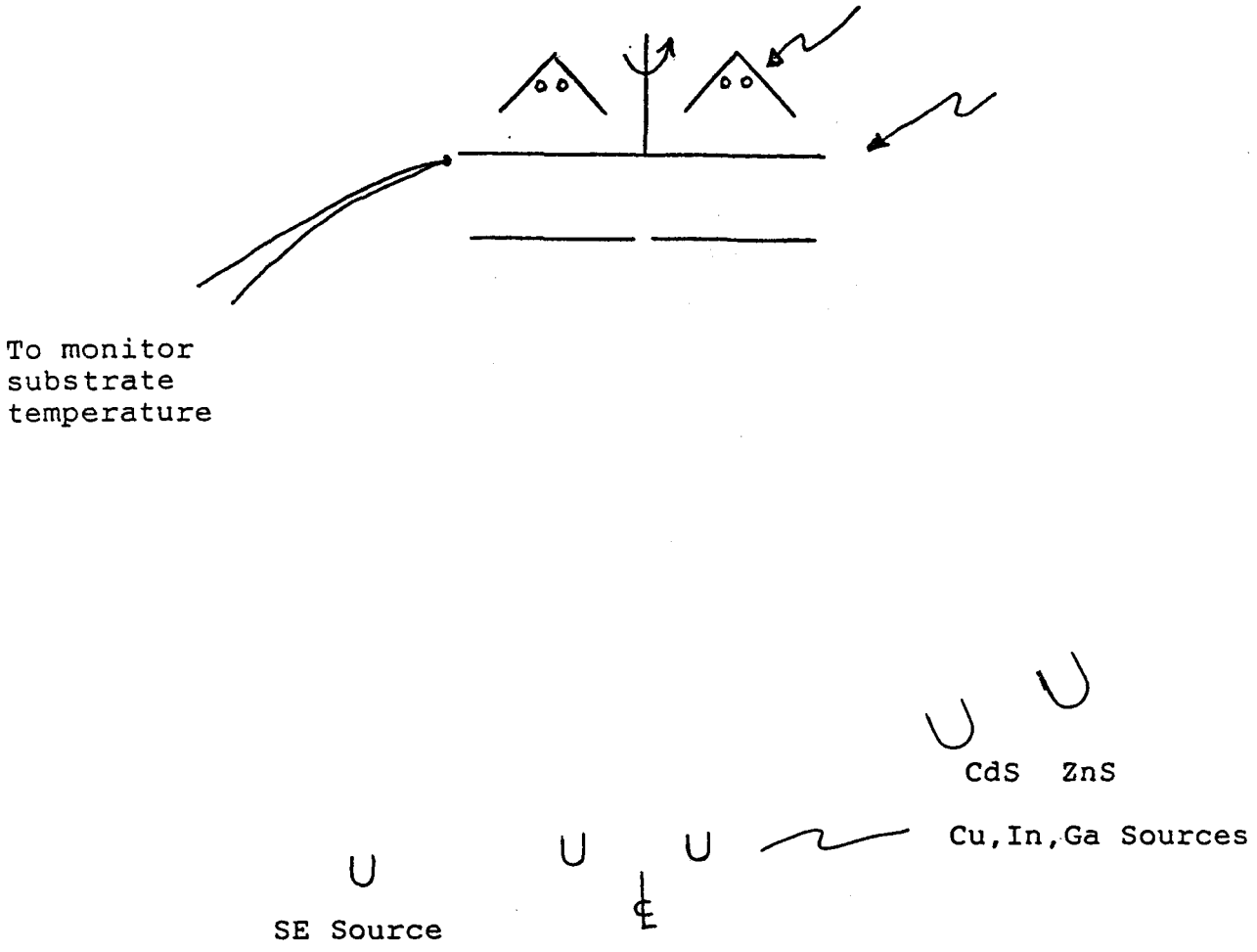

Figure 3.1-1 Schematic of $CuInGaSe_2$ Evaporation Chamber

planet is rotated forward and in reverse so the thermocouple lead is not dislodged. Comparison is then made with the system thermocouple. The new substrate heater configuration requires approximately 800 watts of power whereas the previous design used 8 kW.

New evaporation sources for the Cu, In and Ga have been designed. The sources are of furnace type with a boron nitride crucible to hold the evaporant. It is essential the crucible be rigidly mounted to give run-to-run reproducibility. A schematic of the source is shown in Fig. 3.1-2. The sources are mounted in positions and orientations so as to maximize uniformity across the substrate and maintain sensitivity of the rate controller.

The Cu, In and Ga deposition rates are monitored by EIES sensors. The Se rate is controlled by a quartz crystal. The Cu and In sources are placed close to each other so they can be monitored by the same EIES sensor. A separate EIES sensor controls the Ga deposition rate. In the ideal case a single EIES sensor head would be used to control all of the Cu, In and Ga sources to avoid possible drift between the separate sensors.

Separate CdS and ZnS LUXEL sources have been mounted in the chamber for the in-situ formation of CdZnS doped with In. These sources are controlled by a quartz crystal monitor and are fully operational.

The deposition process is performed by preheating the sources and substrates simultaneously. The procedure is to have the substrate reach the desired temperature simultaneously with the Cu,In,Ga and Se sources reaching the appropriate rates. This allows the Mo back contact to be exposed to a minimum amount of Se. Exposure of the Mo surface to Se for long periods of time without the formation of the selenide film results in reduced adhesion of the film. The usual procedure is to heat the substrate to 450°C during the formation of the first layer, then raise the temperature to 550°C for the second layer. In forming the second layer, the Cu is reduced by approximately 30%. After the second layer is formed the substrate temperature is reduced. During this entire run the In, Ga and Se rates remain constant. While the substrate temperature is dropping the CdS and ZnS sources are preheated. At a substrate temperature of 200°C the sulfide layer is deposited.

Overall the vacuum chamber runs with good reproducibility from run-to-run. The reproducibility is comparable to or better than that experienced in the fixed substrate vacuum

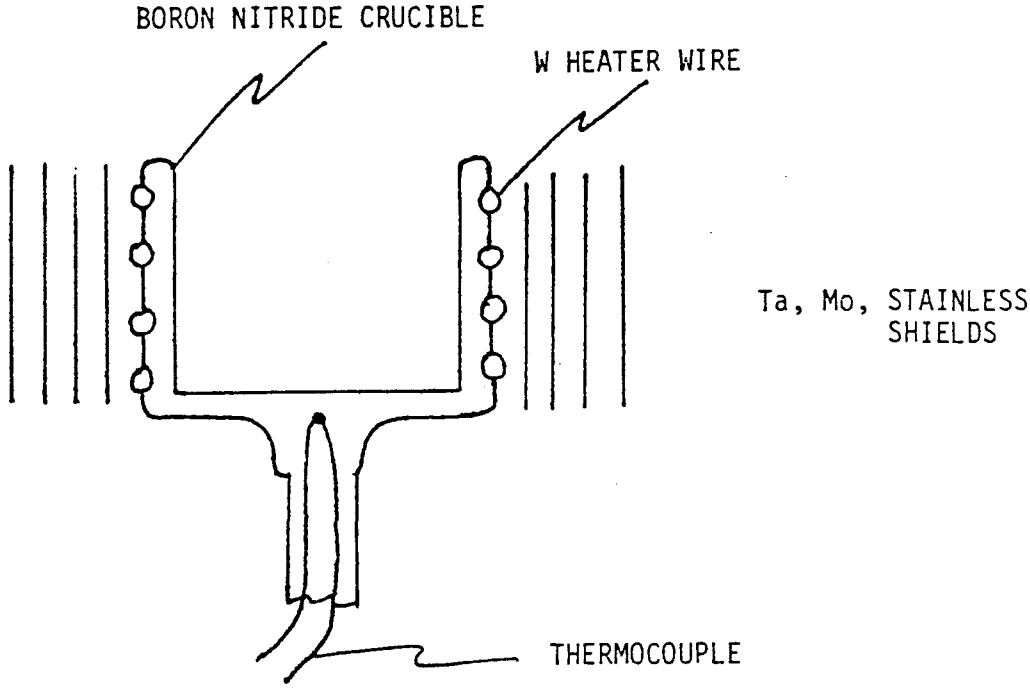

Figure 3.1-2 SCHEMATIC OF EVAPORATION SOURCE FOR Cu, In, Ga

system for $CuInSe_2$. The reasons for this have mainly to do with the rigidly mounted evaporation sources. Some difficulties yet to be resolved are the indication that as the Ga content is increased, the substrate temperature must be increased. If the substrate temperature is too high then there is a possibility of the selenide film peeling from the substrate. A tungsten film has been sputtered over the Mo back contact to see if that will help the adhesion problem. To date the results are negative. In the future Pt will be tried. Other possibilities for resolution of this problem are the use of a new Se source that will control the selenium vapor species. This could allow one to achieve the same results selenide formation but at a lower substrate temperature.

$CuIn_{1-x}Ga_xSe_2$ material has been made with x varying from 0.04 to 1.0. In the initial "tuneup" of the chamber, $CuInSe_2$ material was made for comparison to material made in the fixed substrate systems. $CuInSe_2$ material made with a substrate temperature of 600°C had the interesting feature that it showed grains varying up to 5 μm in size (8). Cells made from this material showed efficiencies up to 9.8% (AM1) without AR coatings.

It appears that as the Ga content of the film is increased, there must be some increase in the substrate temperature above that required to make $CuInSe_2$. If the substrate temperature is too low, poor cell performance is observed and the cell surface shows a non-uniform morphology (8).

3.1.2. Device Analysis

During the contract period, $CuIn_{1-x}Ga_xSe_2/Cd_{1-z}Zn_zS$ cells of 1 cm^2 area were made using mixed selenide films with composition index "x" values from 1.0 (100% in Ga content, i.e., $CuGaSe_2$) to 0.25 (25% in Ga content) and the mixed sulfide films with fixed Zn content (z = 0.12). All cells were tested under simulated AM1.5 illumination (ELH lamp, 100 mW/cm^2). The cells showed improvement after being heat treated at 225°C in an oxygen environment for 5 to 20 minutes. The performance of the best cell has been verified by SERI measurement.

The photovoltaic characteristics of non-AR coated cells of various Ga content are shown in Fig. 3.1-3 and summarized in Table 3.1-1.

The extremely low fill factor of the cell with "x"=1 affects the short circuit current. The light generated current of

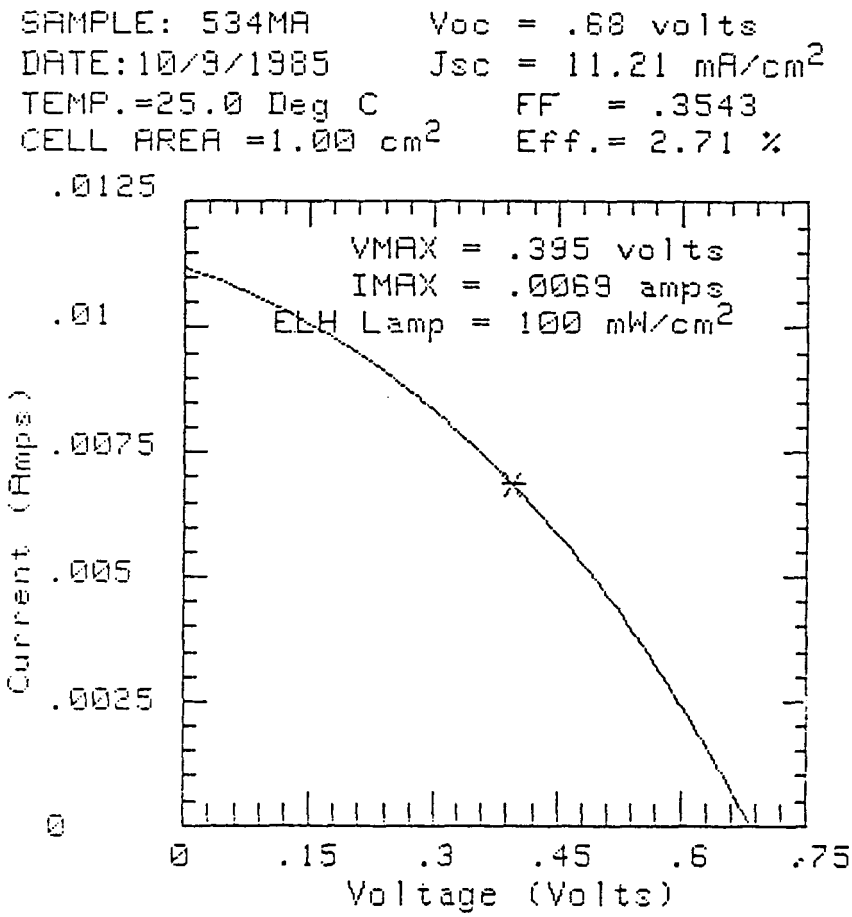

Figure 3.1-3a Illuminated I-V Characteristic for $CuIn_{1-x}Ga_xSe_2/CdZnS$ Cell with x = 1.0

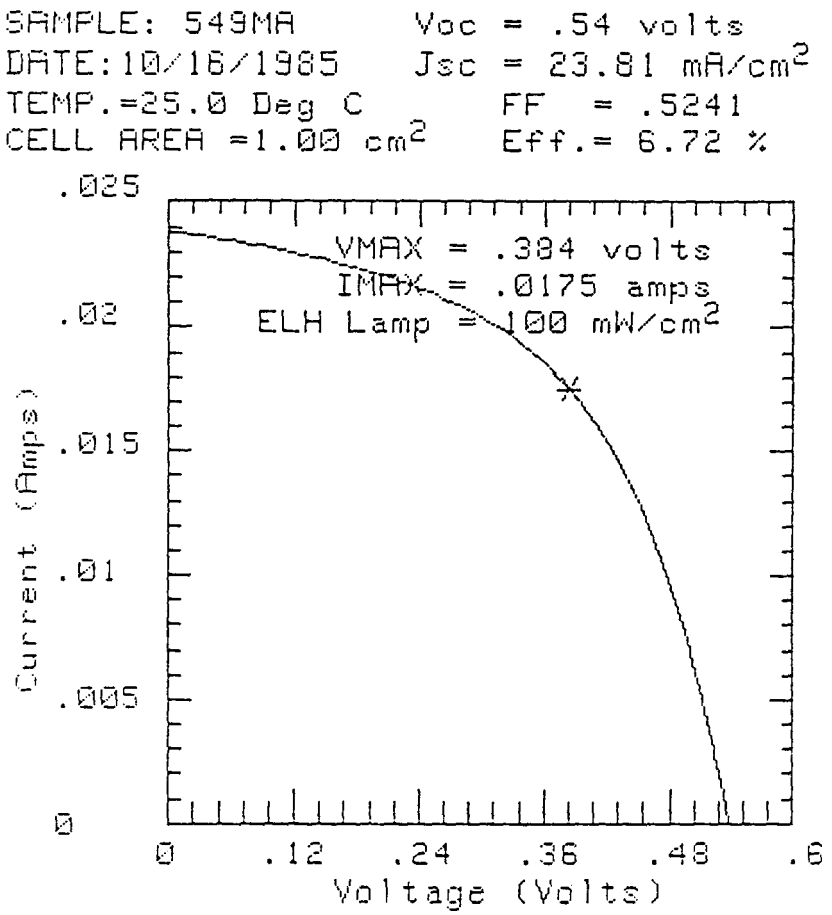

Figure 3.1-3b Illuminated Characteristic for $CuIn_{1-x}Ga_xSe_2/CdZnS$ Cell with x = 0.50

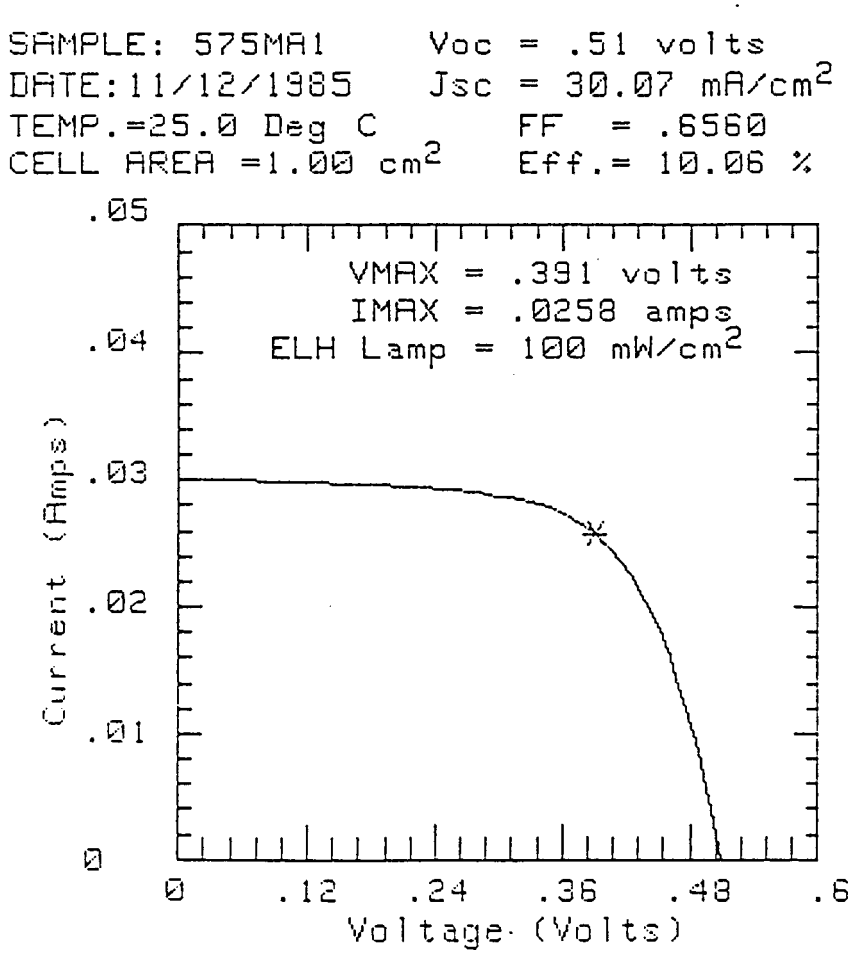

Figure 3.1-3c Illuminated I-V Characteristics for $CuIn_{1-x}Ga_xSe_2$/CdZnS Cell with x = 0.25

this cell is actually near 15 mA/cm^2, but the cell must be back biased to over 1 volt to attain current saturation. The open circuit voltage is lower than the one reported by Arndt,et al (20). This may be due to our mixed sulfide having much less Zn than that of the Stuttgart group.

Table 3.1-1: Photovoltaic Characteristics of Cells with Various Ga Content in The Selenide Layer

Composition Index"x"	Open Circuit Voltage	Short Circuit Current	Fill Factor	Eff.
1.0	0.68 Volt	11.21 mA/cm^2	0.35	2.71 %
0.5	0.54	23.81	0.52	6.72
0.25	0.51	30.37	0.66	10.06

The fill factor significantly improves as the Ga content is reduced. Although the efficiency of the 50% Ga cell is near 7%, the fill factor is still poor compared with our normal $CuInSe_2$ cells. The reverse bias saturated light generated current is about 26 mA/cm^2, slightly above the short circuit current. The poor fill factor of cells with high Ga content selenide is attributed to either a high resistance at Mo/Selenide contact or a non-ohmic back contact as discussed in the first annual report.(9)

Cells made from the selenide films with approximately 25% Ga have shown conversion efficiencies greater than 10%, comparable to the best $CuInSe_2$ cells. Efficiencies of the as-deposited cells were over 9%. Improvement in both open circuit voltage and fill factor has been observed after only a 5 minutes bake at 225°C in oxygen. The illuminated I-V characteristics before and after the heat treatment are shown in Fig.3.1-4. The cell has also been measured under ASTM-85 Global, 1000 W/m^2 conditions at SERI, which gives:

Area=1.033 cm^2, V_{oc}=0.5043 V, I_{sc}=29.05 mA, F.F.=0.6559 Eff.=9.3%.

The major differences between our measurements and SERI are the area definition and the light calibration.

Recently, we developed a process to deposit an optimized two layer, SiN:H and SiO:H, antireflection coating on our cells by a low temperature PECVD technique. The reflectance of a cell before and after the AR coating are shown in Fig.3.1-5.

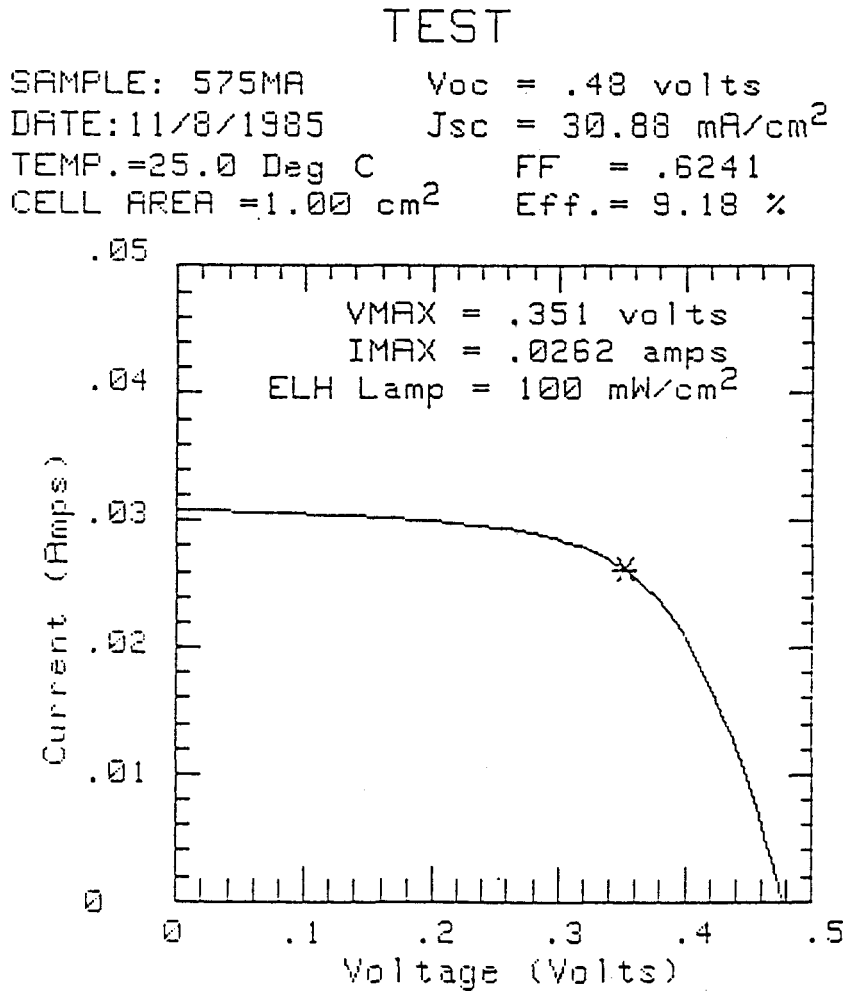

Figure 3.1-4 Illuminated I-V Characteristics of
with Selenide Film Containing 25% Ga. (a) as deposited

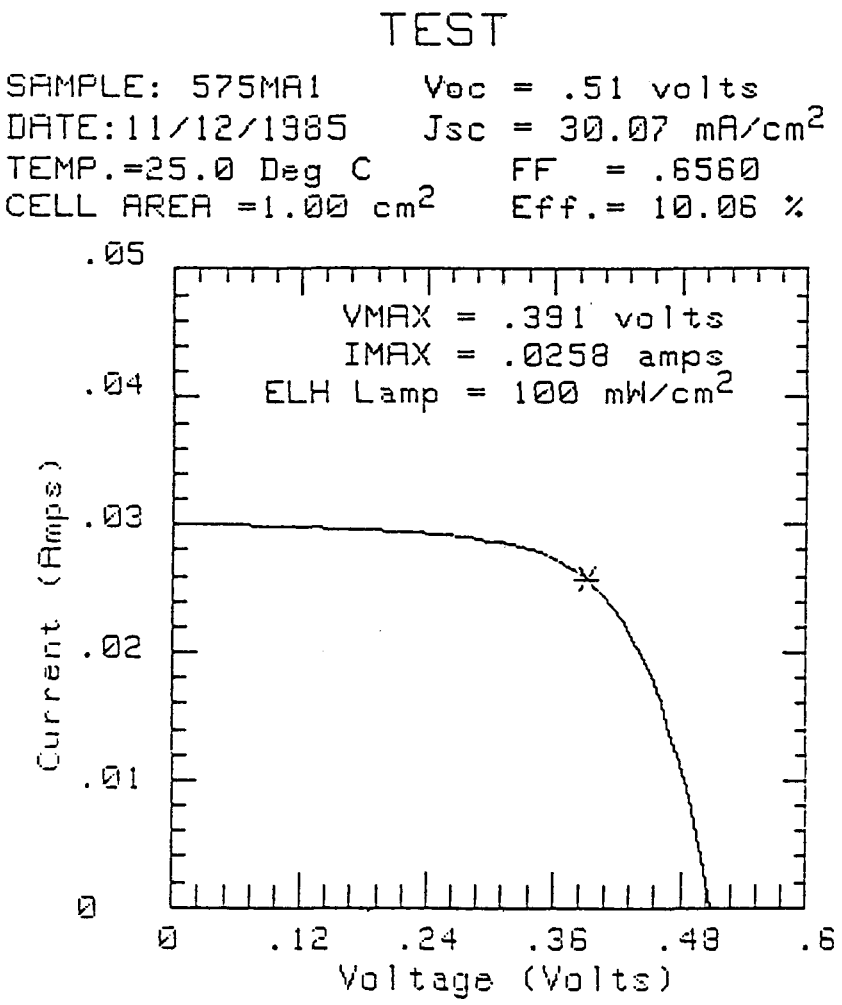

Figure 3.1-4 (b) After 5 minutes, 225°C Bake in O_2.

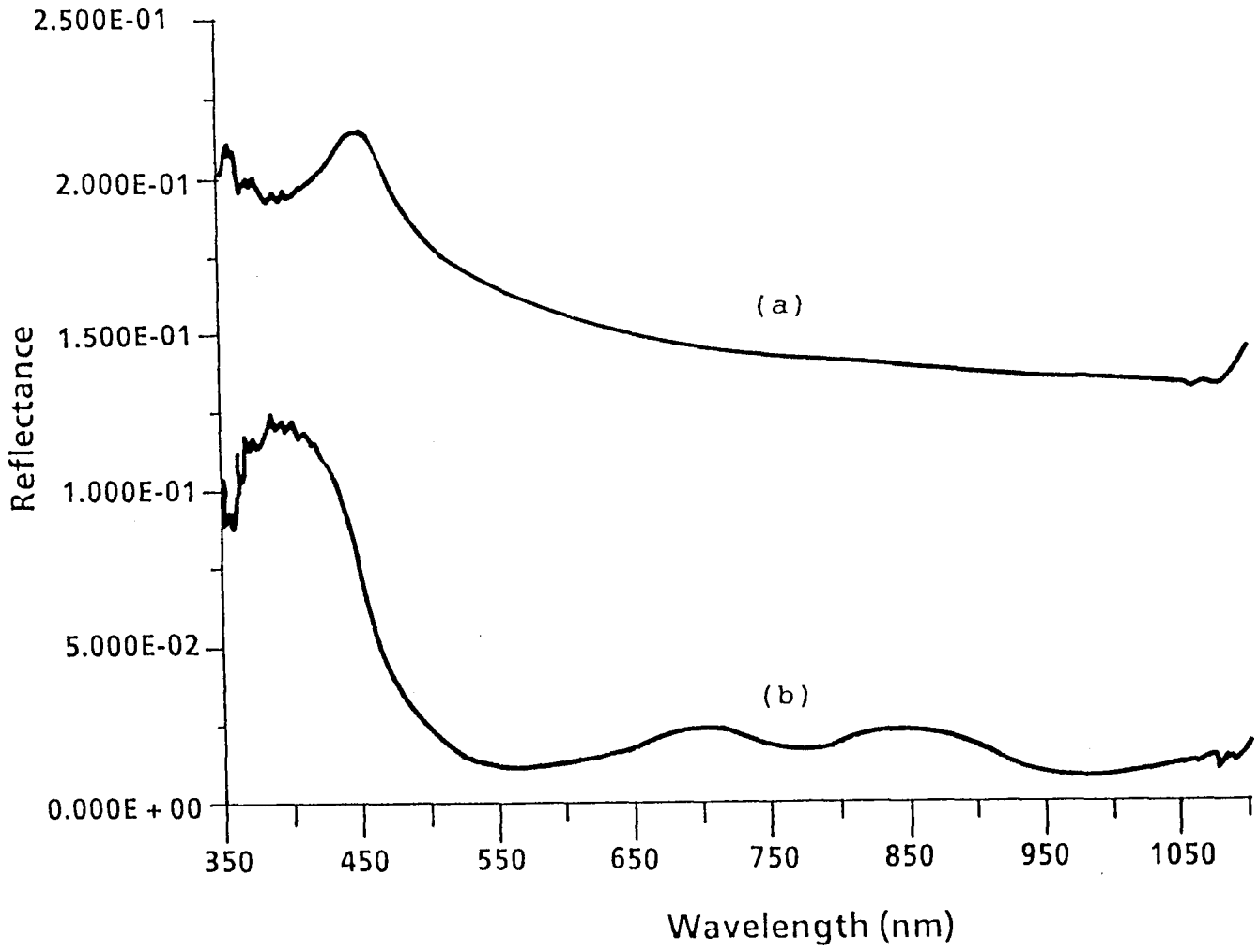

FIGURE 3.1-5 REFLECTANCE OF A $CUIN_{0.77}GA_{0.23}SE_2$/ZnCdS CELL

(a) BEFORE AR (b) AFTER AR

TEST
11/19/1986 13:30:07
BAC SAMPLE: 746MA
TEMPERATURE: 25.0 Deg C
UNIT CELL Area 1.000 cm^2
Total CELL Area 1.000 cm^2
No. cell in series = 1.00
No. of cell in parallel = 1.00
Base type is P type
REMARK: BEFORE AR

CURVE#	INTENSITY (mW/cm^2)	EFFICIENCY (%)	VOC (Volt)	ISC (Amp)	VMAX (Volt)	IMAX (Amp)	FILL FACTOR
1	100.00	9.23	.4982	2.7375E-02	.386	2.391E-02	.6769

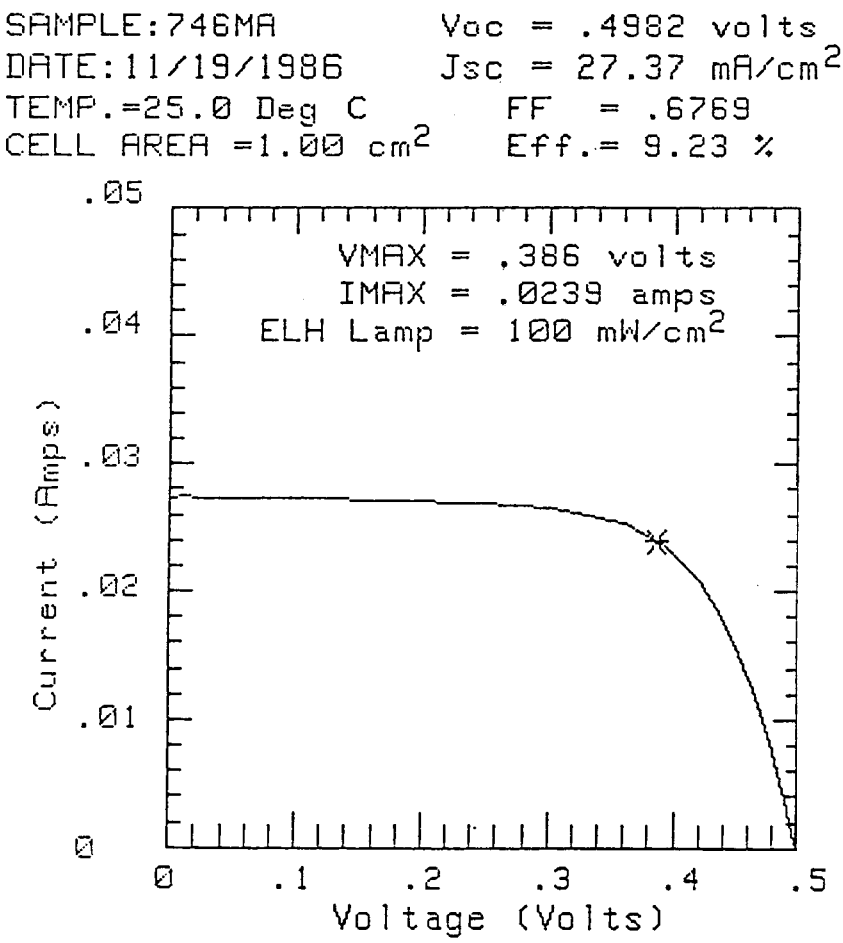

(a)

Figure 3.1-6a Illuminated I-V Characteristics of $CuIn_{0.77}Ga_{0.23}Se_2$/ZnCdS Cell
(a) before AR

TEST
12/1/1986 08:34:43
BAC SAMPLE: 746MA
TEMPERATURE: 25.0 Deg C
UNIT CELL Area 1.000 cm^2
Total CELL Area 1.000 cm^2
No. cell in series = 1.00
No. of cell in parallel = 1.00
Base type is P type
REMARK:

CURVE#	INTENSITY (mW/cm^2)	EFFICIENCY (%)	VOC (Volt)	ISC (Amp)	VMAX (Volt)	IMAX (Amp)	FILL FACTOR
1	100.00	10.71	.5010	3.2092E-02	.384	2.790E-02	.6663

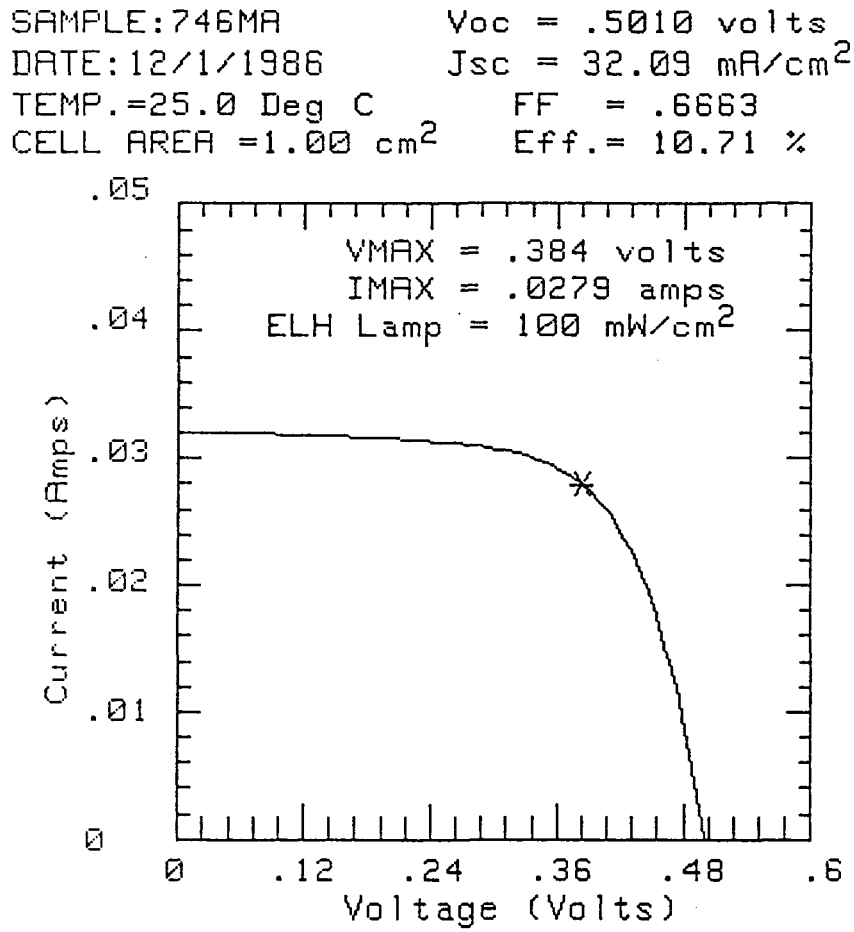

Figure 3.1-6b After AR

Short circuit currents have increased more than 16% on a cell made with a selenide film of 23% Ga. The characteristics of the best cell before and after the AR coating are shown in Fig.3.1-6 and summarized in Table 3.1-2.

Table 3.1-2: Characteristics of Cell Before and After AR coating.

	V_{oc} (Volt)	I_{sc} (mA)	F.F.	Eff.(%)
Before	0.4982	27.38	.6769	9.23
After	0.5010	32.09	.6663	10.71

The I-V characteristics of this cell measured by SERI under ASTM85 GLOBAL, 1000W/m^2 condition is shown in Fig.3.1-7. The only major error in our measurement is our underestimation of the cell area. We use 1 cm^2 as our nominal cell area. The 10.2% efficiency of this cell is comparable to the SERI measured efficiency of our best AR coated $CuInSe_2$ cell.

The selenide band gap energy for different Ga content can be estimated from the long wavelength cutoff of the spectral response measurements as shown in Fig. 3.1-8. Results are plotted in Fig.3.1-9 as a function of composition index "x". In this figure the dots represent experimental points and the solid line is a best fit to the data using the equation:

$$E_g = 1.02 + 0.67x + 0.14x(x-1) \quad eV.$$

There is a distinct bowing to the curve . The data is very similar to the one reported for single crystal $CuInS_{2x}Se_{2-2x}$ (21) but is not in agreement with the data of Bachmann (22).

3.2 Large Area Cells

The large scale application of CIS based photovoltaics for power generation depends on system costs being reduced sufficiently to make them competitive with other generation techniques. In addition to the direct economy of scale, the interconnection and assembly costs are a significant fraction of the total system costs which are directly reduced by increased device size if efficiency does not suffer.

Demonstrating scalability of the CIS/CdZnS cell from the 1cm^2 research devices was, therefore, a major program goal. The

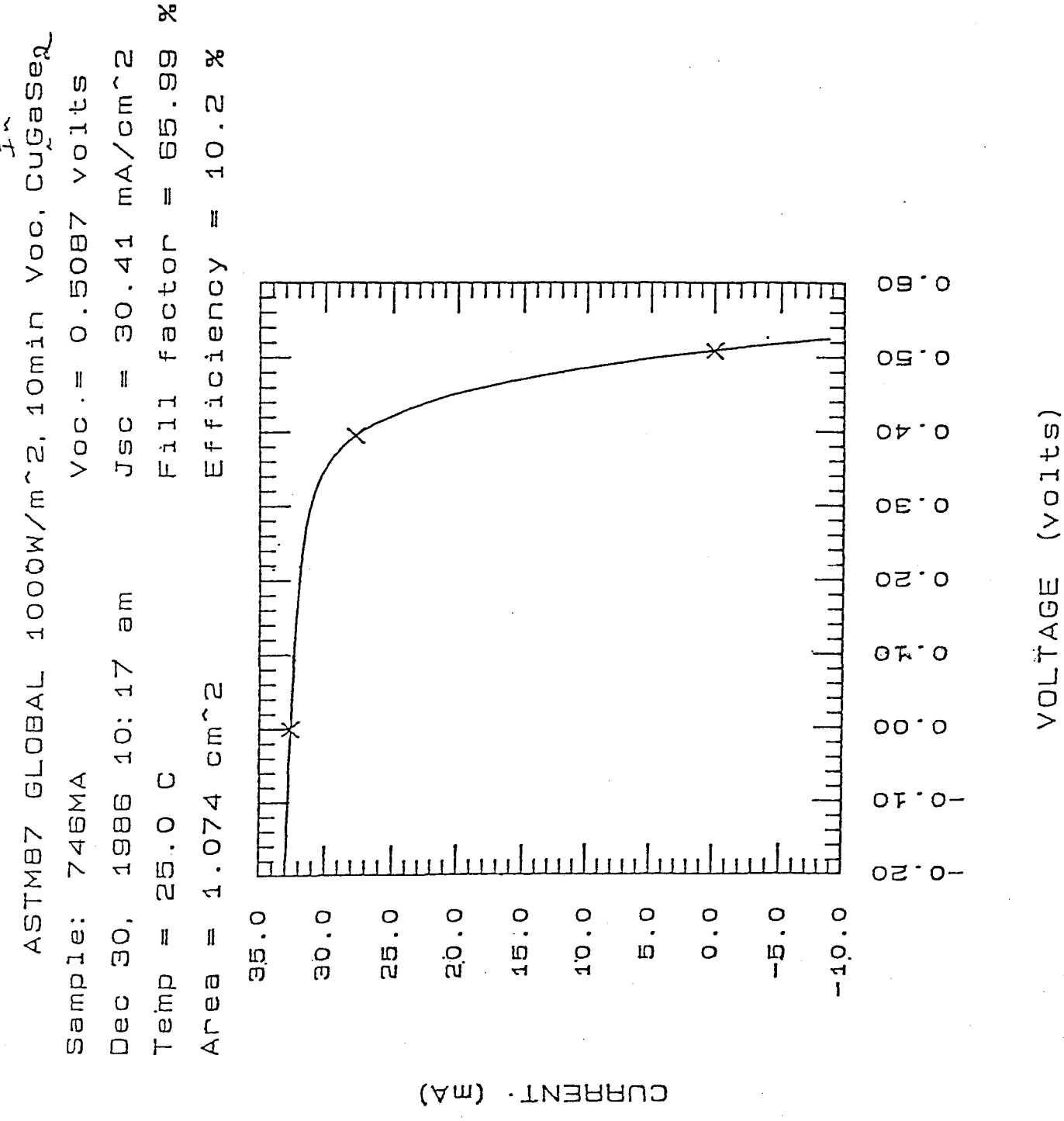

Figure 3.1-7 Characteristics of the $CuIn_{0.77}Ga_{0.23}Se_2/250$ Measured at SERI

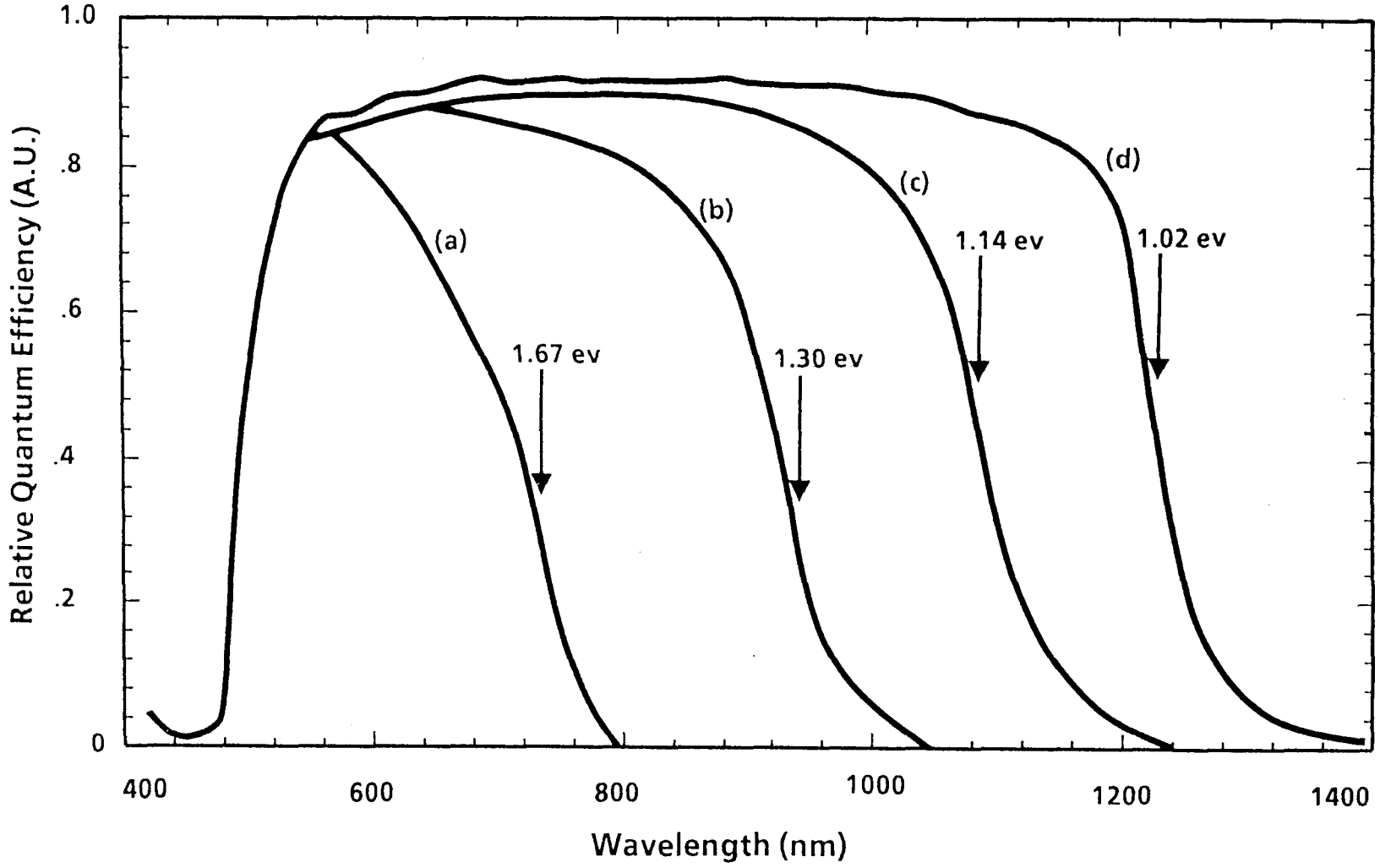

Figure 3.1-8 Relative Spectral Response of Cells with Different Selenide Composition (a) X = 1.0, (b) X = 0.5, (c) X = 0.25, (d) X = 0

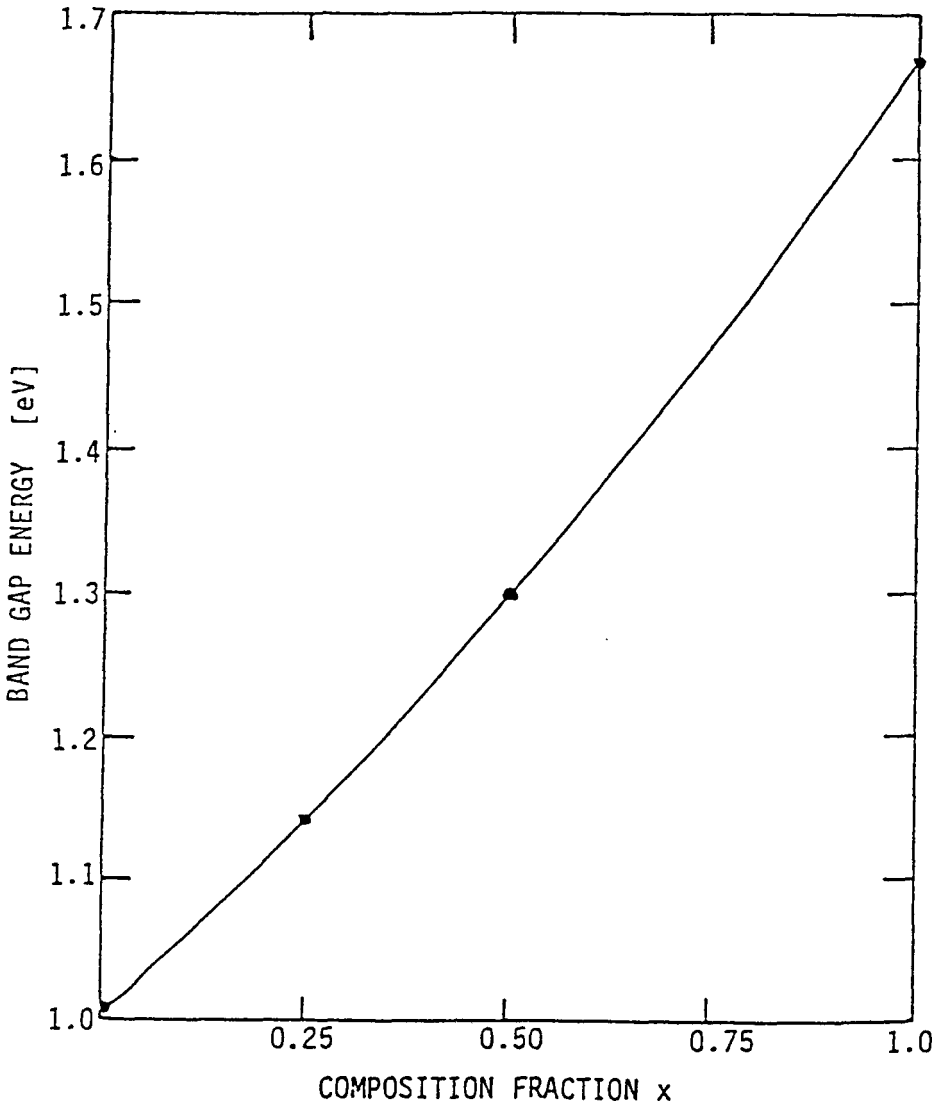

Figure 3.1-9 Band Gap Energy of $CuIn_{1-x}Ga_xSe_2$ Films at Room Temperature Versus Composition Fraction x.

approach, cell design, fabrication methods, and resulting cell performances relating to the achievement of the large area cells, were summarized in a paper presented at the 19th IEEE Photovoltaic Specialists Conference (12). In addition, many of the processing details for the large cells are discussed in references (7,8,9).

The spectral response curve has been measured for module S376, the sample for which the I-V data is reported in reference 12. This curve is shown in Fig. 3.4-1. The quantum efficiency is essentially flat from the selenide band edge to the onset of sulfide window absorption.

Also remarkable is the degree of matching shown by the four individual cells in the series string. Fig. 3.4-2 shows I-V curves for each of the cells in the string, taken by driving the entire string and measuring the voltage across each of the cells. Fig. 8 of reference 12 was derived from the data of Fig. 3.4-2.

3.3 Basic Measurements

Section 3.3.1 Photoluminescence Measurements

The photoluminescence of polycrystalline thin-film $CuInSe_2$ samples has previously been observed and reported by Boeing (4,5). These measurements were made at low temperature (10-60°K) using a low power (15 mW) HeNe laser as the exciting source. The emission showed two or three broad bands in the spectral region between 1300 and 1440 nm. Occasionally a sharper emission band at a wavelength near 1265 nm. was detected in non-heat treated samples along with the broad band emission. The features of the emission spectrum were also found to be temperature dependent.

Although a good correlation was found between high efficiency cell response and some features of the photoluminescence emission, the limited size capability and the uncertain effects of the low temperature testing on the selenide excluded routine testing of cell material. The major bar to higher temperature measurements was found to be the weak emission available even at the lowest temperatures with the excitation power available. Over the first three quarters of this contract therefore a new photoluminescence measurement system was constructed to investigate the emission of the $CuInSe_2$ near room temperature and at higher excitation power levels. A block diagram of the system is shown in figure 3-9

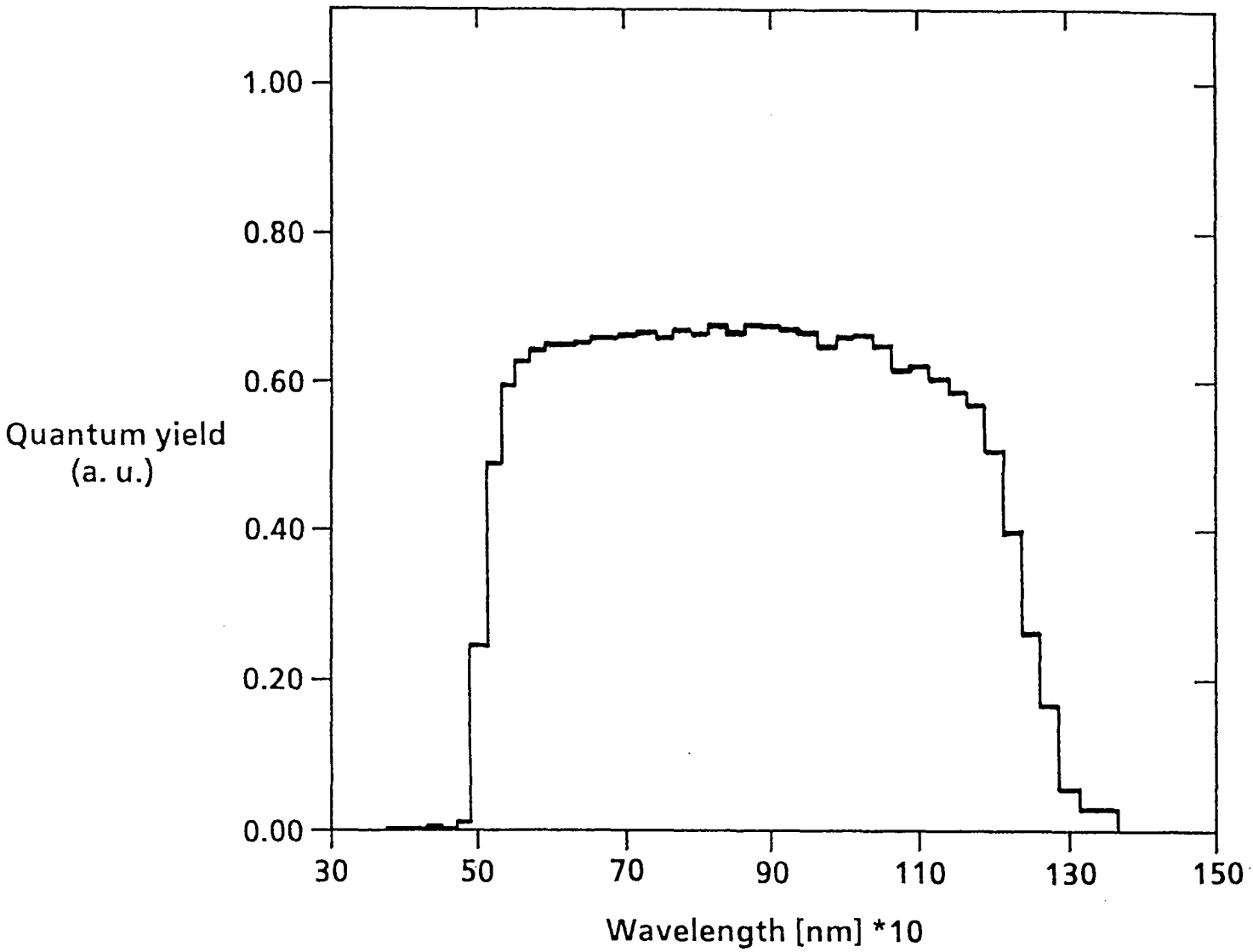

Figure 3.2-1 Spectral Response of S376, 4" x 4" submodule. Response of single cell was identical.

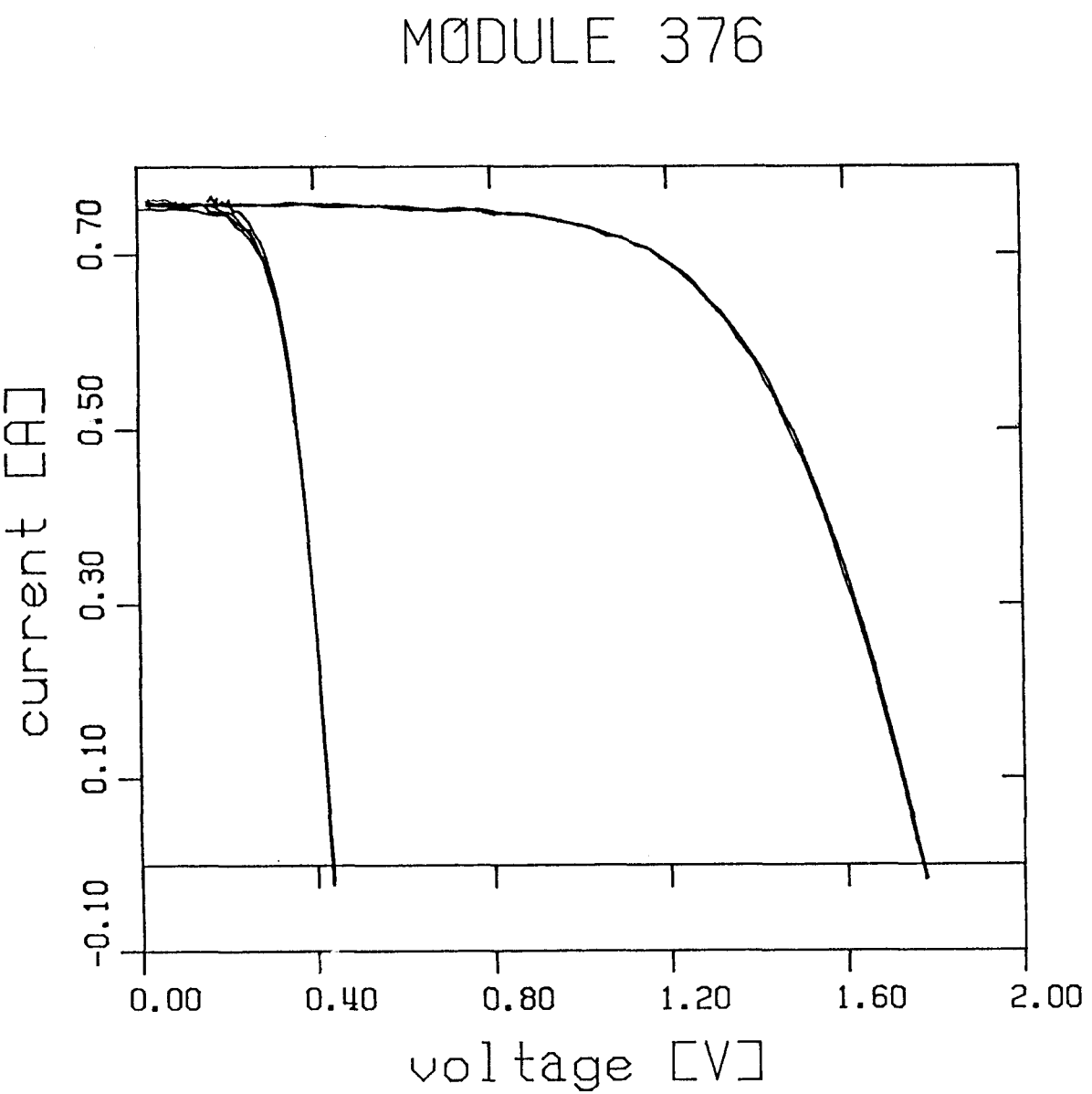

Figure 3.2-2

Original I-V data of 4 individual cells in submodule S376 plus Full Module Curves taken before and after individual cell curves

of reference (8) and is described in more detail in that report. The excitation source is now a Krypton laser (150 mW at 647 nm). A lead sulfide detector and mechanical light chopper are being used. At present data can either be taken on an X-Y recorder or directly using an IBM-XT computer when the data analysis requirements warrant.

During this contract measurements were made on several $CuInSe_2$/CdS thin-film samples at room temperature, including sample BAC799B for which 12°K photoluminescence data is included in reference (5). All of these samples showed essentially similar characteristics in the room temperature emission spectrum. A typical photoluminescence spectrum is shown in Figure 3.3-1. A single broad emission peak is seen at 1265 nm, near the selenide absorption edge. The actual intensity was highly variable from sample to sample and did not seem to correlate strongly with cell characteristics. On $CuInSe_2$ layers without CdS the emission peak was similar but the emission intensity was much lower. Isolated CdS or CdZnS layers showed no emission.

These results seem to indicate little prospect for using the room temperature luminescence as a non-destructive film characterization tool. It is suggested that future work explore the temperature dependence of the emission over the full temperature range from 12°K to room temperature to determine the relationship between the broad emission seen at room temperature and the low temperature peaks seen in previous work.

3.3.2 Voltage Contrast Measurements

Recent EBIC studies of $CuInSe_2$/CdS devices in cross section (23) have clearly demonstrated current collection in regions isolated from the apparent metallurgical junction and have therefore raised serious questions concerning the location of the rectifying junction in both as-fabricated and heat-treated $CuInSe_2$/CdS devices. While related, the issues are somewhat different in the two cases. In heat-treated, high efficiency devices the EBIC results raised the possibility of a p-$CuInSe_2$/n-$CuInSe_2$ (or i-$CuInSe_2$)/n-CdS structure with the n-$CuInSe_2$ region perhaps 0.1 -0.5 μm thick. This issue is critical to the Boeing research program since approaches to device modeling and the methods tried to increase V_{oc} depend strongly on the junction structure assumed.

Several basic tests have been proposed to resolve the issues raised. We have pursued one technique in particular, Voltage

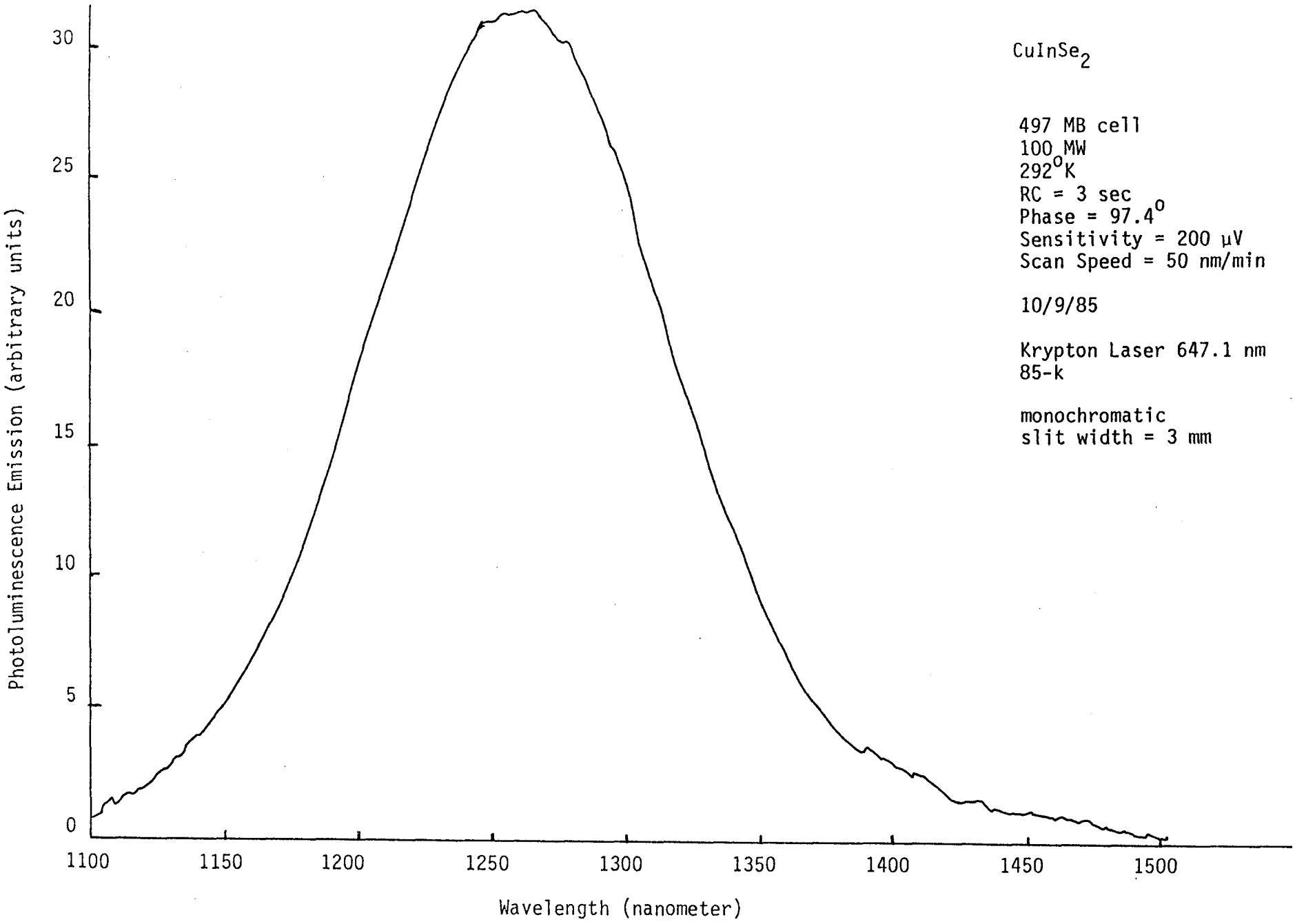

Figure 3.3-1 Thin Film Photoluminescence Emission at Room Temperature

Contrast Imaging in a Scanning Electron Microscope (24), both because it is particularly suitable for directly imaging the collection junction and because Boeing has particular expertise in this technique.

Figure 3.3-2 shows a comparison of the standard Secondary Electron (SEI), EBIC, and Voltage Contrast images for one heat treated sample from a substrate producing good, high current, high efficiency cells. The pictures were taken on an ISI S3A SEM. The Voltage Contrast images were taken with the selenide biased at -5 volts with respect to the sulfide; that is, in far reverse bias. The image shows a sharp brightness transition not present in the SEI corresponding to the voltage bias difference. The correspondence between the collection region in the EBIC image and the negatively biased region in voltage contrast is clear. The apparent metallurgical junction between selenide and sulfide shows clearly in the Secondary Electron image. The arrows indicate several features identifiable in all three images. There is a clear offset of 0.15 - 0.25 μm between the voltage transition region and EBIC collection region edge, which agree, and the metallurgical junction in the SEI. We have, therefore, been able to reproduce the offset effect seen by the previous experimenters and establish a correspondence with the voltage transition region.

However, this result was not the common behavior in the samples tested, although this particular device was itself uniform. In some samples the voltage contrast could not be distinguished from intrinsic differences in image brightness between the sulfide and selenide. Most common was an inability to accurately determine the location of the metallurgical junction. EDX elemental scans showed only spatially smeared transitions, without obvious causes. Figure 3.3-3 shows an attempt to determine the exact location of the metallurgical junction by using the step produced when the CdS layer is etched away. In this sample the EBIC signal shows no detectable offset from the metallurgical junction at this edge. Note the lack of a clear junction discontinuity away from the step.

All samples discussed so far have been prepared by fracturing working devices. Following a suggestion made by R. Matson of SERI, we tried etching samples in bromine methanol after fracturing, both to identify the metallurgical junction location and to remove surface damage.

These samples were prepared by fracturing small diodes from substrate S234-2. The 1 cm^2 cell from this section was a high voltage, high efficiency cell discussed elsewhere in

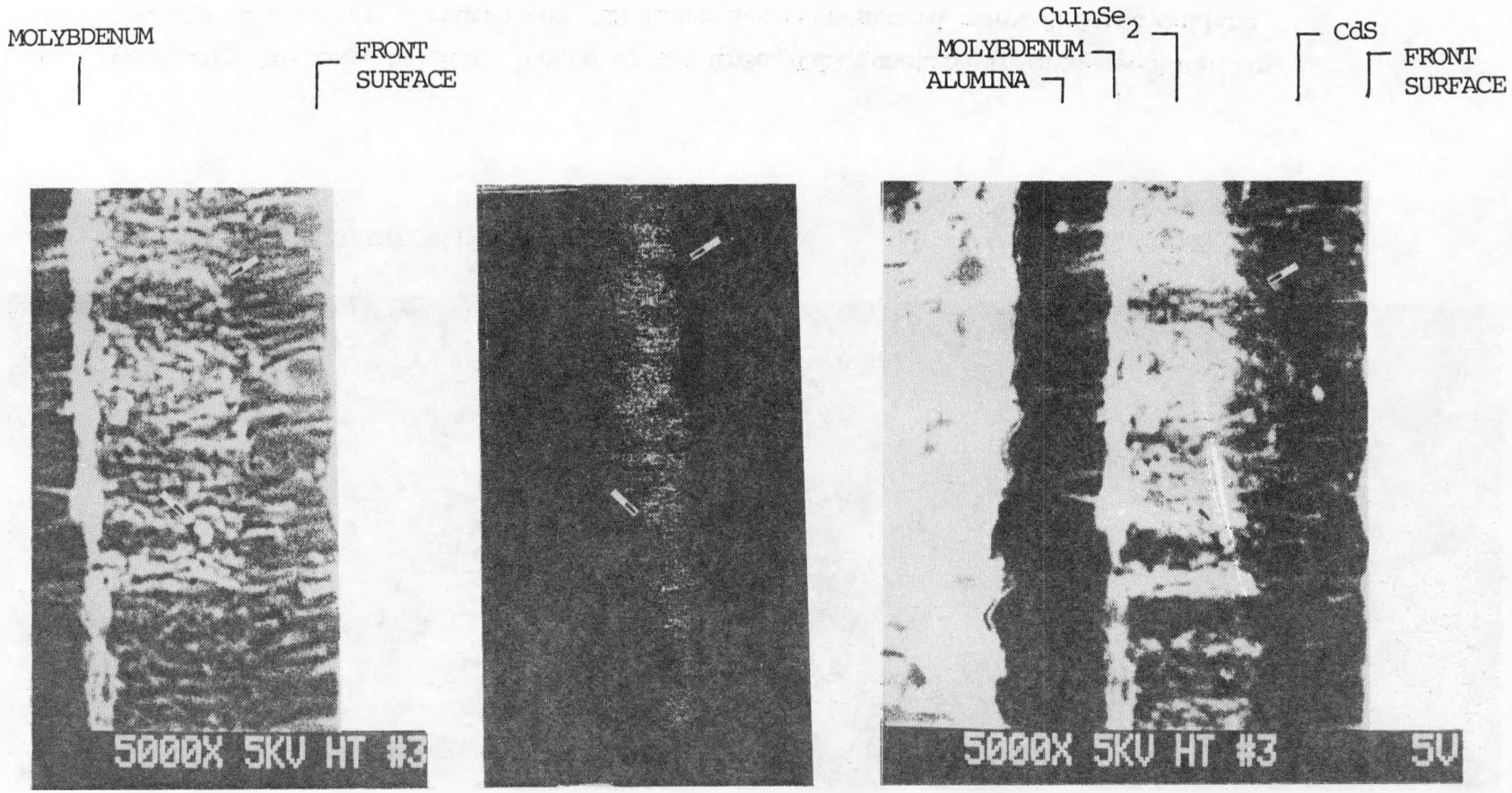

SECONDARY ELECTRON IMAGE

EBIC IMAGE

VOLTAGE CONTRAST IMAGE. SELENIDE BIASED AT -5 V. WITH RESPECT TO SULFIDE.

Figure 3.3-2 Comparison of Secondary Electron, EBIC, and Voltage Contrast images for a heat-treated $CuInSe_2$/CdS cell. Arrows point to features common to all three images

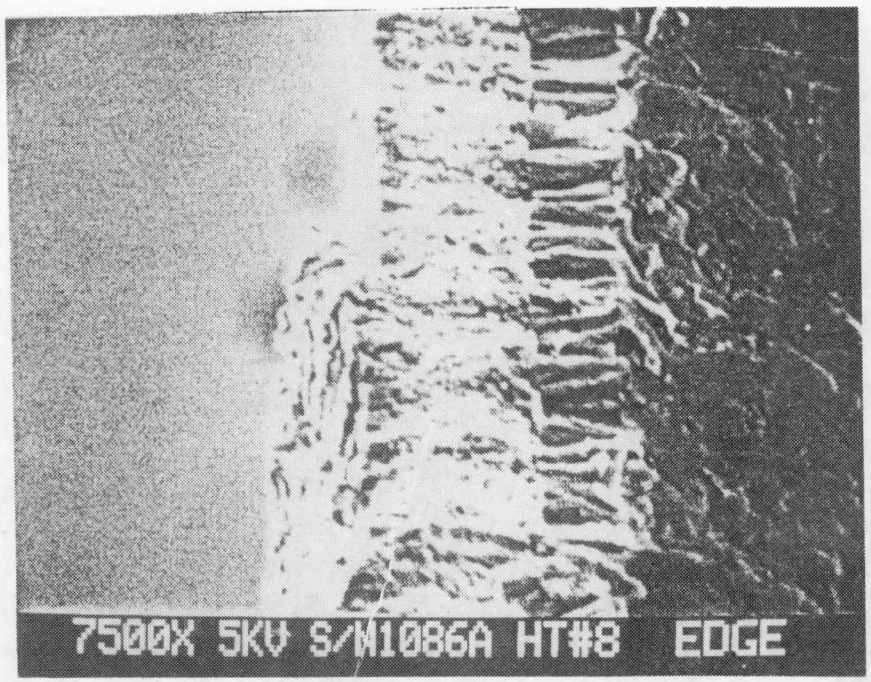

SECONDARY ELECTRON IMAGE

EBIC IMAGE

Figure 3.3-3 Secondary Electron and EBIC images of a $CuInSe_2/CdS$ junction in cross section. In the top half of the pictures the CdS layer has been etched away. A faint outline in the EBIC image locates the step and is marked with an arrow.

this report. Various etch strengths were tried, with a light etch consisting of 3 seconds in 0.1% (Vol) Bromine in Methanol giving a satisfactory image without removing excessive selenide.

Cross sections from S234-2 without etch showed no clear junction location in SE images, see Figure 3.3-4. The light etch described above resulted in an easily imaged step as also seen in Figure 3.3-4.

Secondary Electron and Voltage Contrast images of this lightly etched sample taken at an accelerating voltage of 2KV are shown in Figure 3.3-5. The voltage contrast image shows the intensity transition corresponding to the high field region to be at the base of the etch step at the metallurgical junction, within the resolution of the image. The high field region in this sample is therefore located no more than 0.2 μm from the selenide/sulfide transition. We conclude therefore that for typical Boeing high efficiency, heat treated devices the heterojunction model is still required. The details of the field distribution in the $CuInSe_2$ near the heterojunction were beyond the resolution limit of this voltage contrast equipment.

Some voltage contrast and EBIC measurements were made on non-heat-treated samples. In general, these showed a filamentary or random distribution of both the collection/no collection and the high voltage/low voltage regions in the selenide, consistent with the granular model proposed by Sites (25).

While the work to this point was mainly aimed at addressing questions of junction location in the $CuInSe_2$/CdZnS devices, during the contract a new, more capable voltage contrast system became available at Boeing. The new equipment consists of a Cambridge Instruments S250 Mark 3 SEM with a PGT System 4 Digital Imaging system. The direction of the work was therefore changed toward exploring the possibility of directly imaging the voltage distribution in the junction-near region of the device in cross section and, if possible, determining depletion region width and location from such voltage plots.

Initial voltage contrast results obtained with the new equipment confirmed several effects recently reported in EBIC imaging of the $CuInSe_2$/CdZnS junction cross sections by Matson et al.(23,26). Since the EBIC and Voltage Contrast are actually imaging very different effects, collected current in the case of EBIC and voltage distribution in the case of voltage contrast, the correspondence can be very significant.

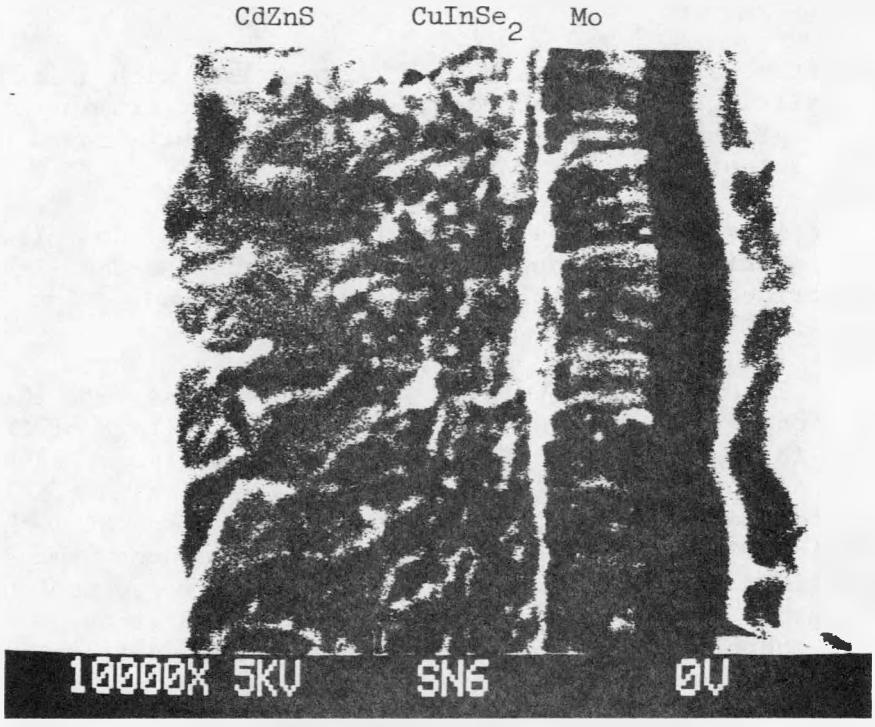

(A) Unetched Junction Cross Section of Sample from S234-2.

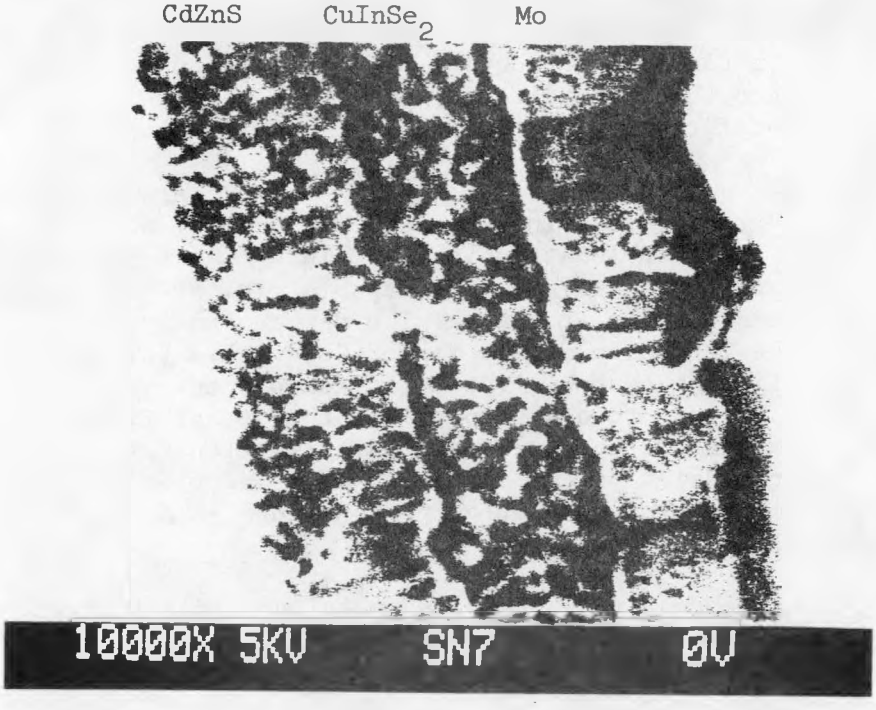

(B) Etched Junction Cross Section of Sample f om S234-2.

Figure 3.3-4 Cross Sections of Etched and Unetched Samples

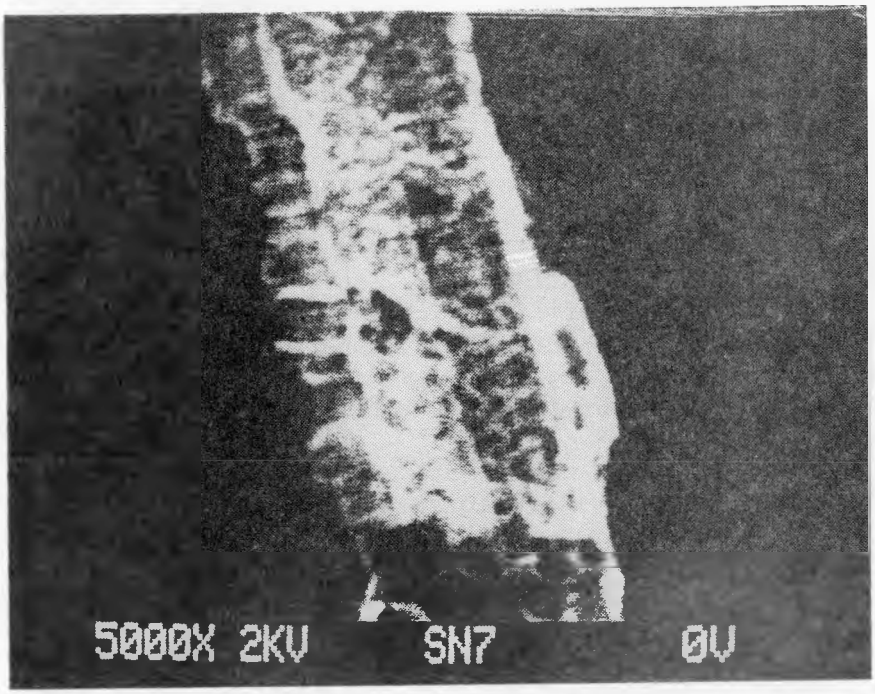

(A) Secondary Electron Image with no sample bias

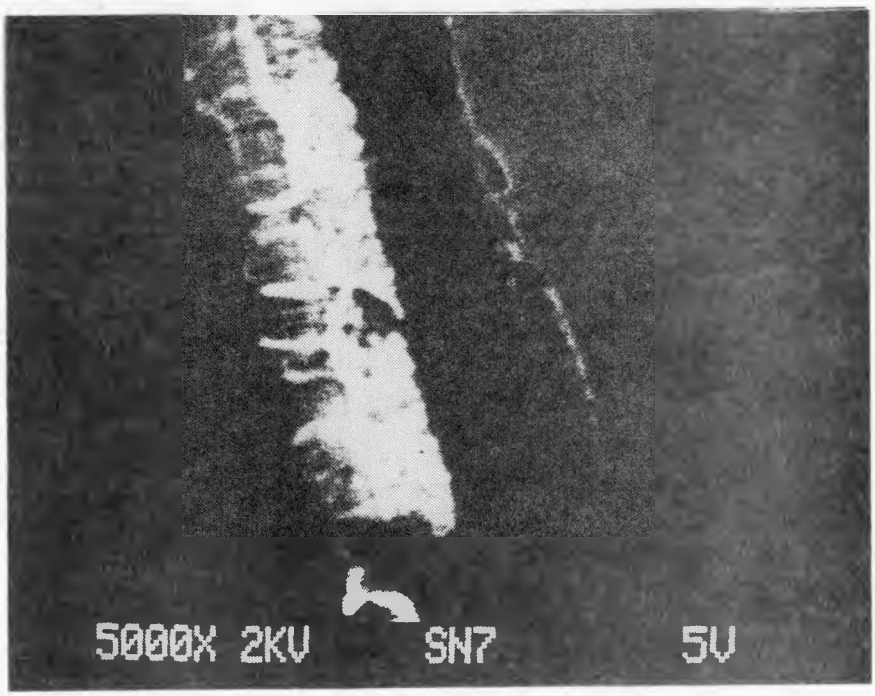

(B) Secondary Electron Image with CdZnS biased at +5V

Figure 3.3-5 Voltage Contrast Images of Etched Sample from S234-2

In as-fabricated devices not yet given the 225°C heat treatment in Oxygen the voltage contrast shows the voltage transition region corresponding to the electrical junction to be buried deep in the selenide and away from the metallurgical junction between the sulfide and selenide. Figure 3.3-6 shows a sequence of voltage contrast images of a $CuInSe_2$/CdZnS junction cross section taken at several different reverse bias voltages for a sample before any heat treatment. Both the offset of electrical from metallurgical junction and the indefinite voltage transition location are clear, agreeing with the EBIC data reported by Matson et al. Junction motion with increased reverse bias is large and the junction moves further into the selenide.

Although not shown in this figure, both the junction motion into the $CuInSe_2$ with repeated scans and the long persistent memory effects of the beam on the sample reported by Matson were also seen in the voltage contrast images. Images were taken at low beam currents so as to minimize (although it did not eliminate) these artifacts

After the 225°C oxygen bake the sample behavior is much clearer. Figure 3.3-7 shows a series of voltage contrast images taken on such a $CuInSe_2$/CdZnS sample after a 5 minute heat treatment. Cells made from this substrate were normal high efficiency devices (>9% without AR). In the figure the electrical junction, while not planar, is sharp and located close to the metallurgical junction. The beam sensitivity, while not eliminated, was much reduced.

Attempts to quantify the voltage distribution profiles in such images and thereby obtain field region width versus bias have not been successful. On cleaved single crystal silicon diodes reasonable qualitative results can be obtained versus voltage but with the rough surfaces and non-uniform junction locations observed on the $CuInSe_2$/CdZnS samples no quantitative data was possible. Other problems such as sample charging and image shifts also become important when line profile comparisons are attempted.

All samples used were cleaved as described in the previous work. No etch or other surface preparation was used since we have had difficulty with the etched samples deteriorating in storage.

One problem with the voltage contrast is the requirement of at least 1-5 volts bias on the sample for detectable contrast. Images can only be obtained therefore in relatively far reverse bias, as seen in figure 3.3-7. Perhaps the greatest drawback of the voltage contrast technique is the

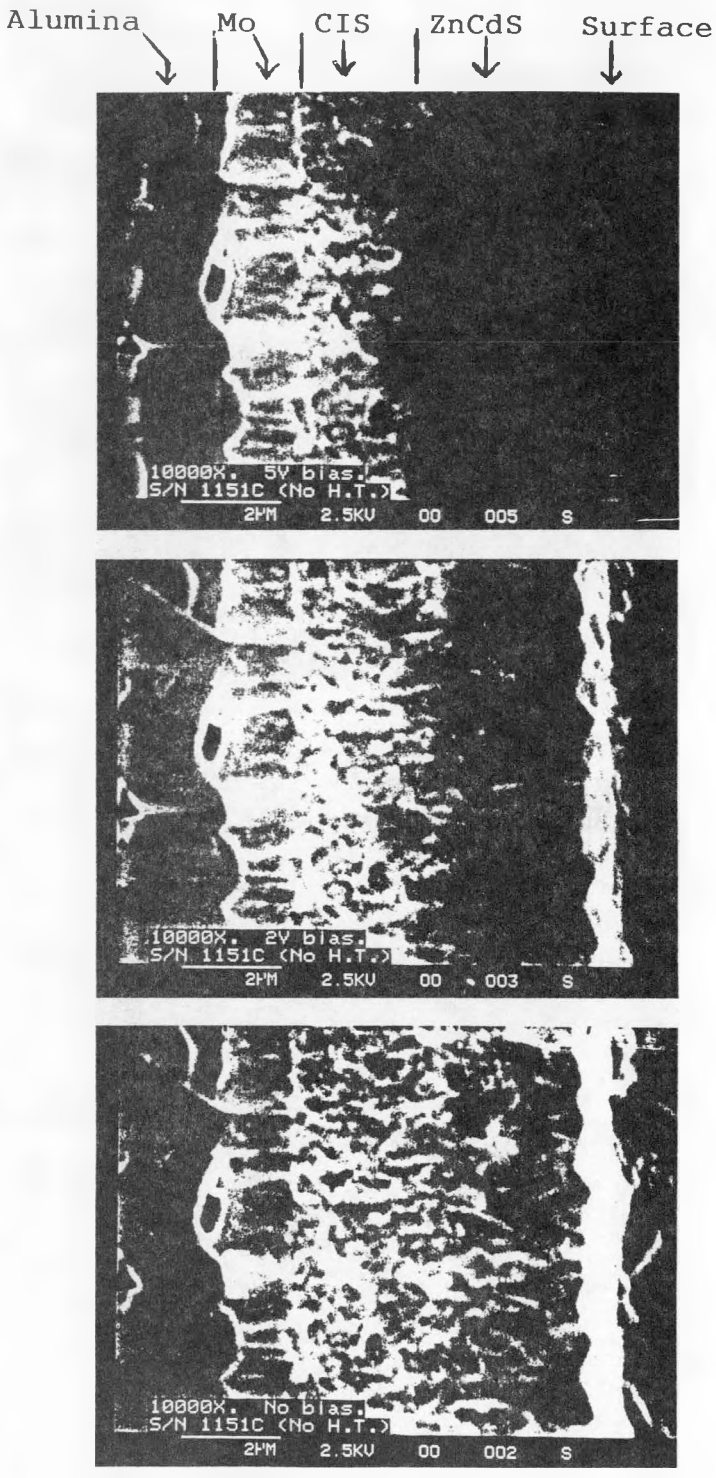

Figure 3.3-6 Voltage Contrast Images of Junction Cross Section for Sample Given No Heat Treatment. Three Voltage Biases are Shown.

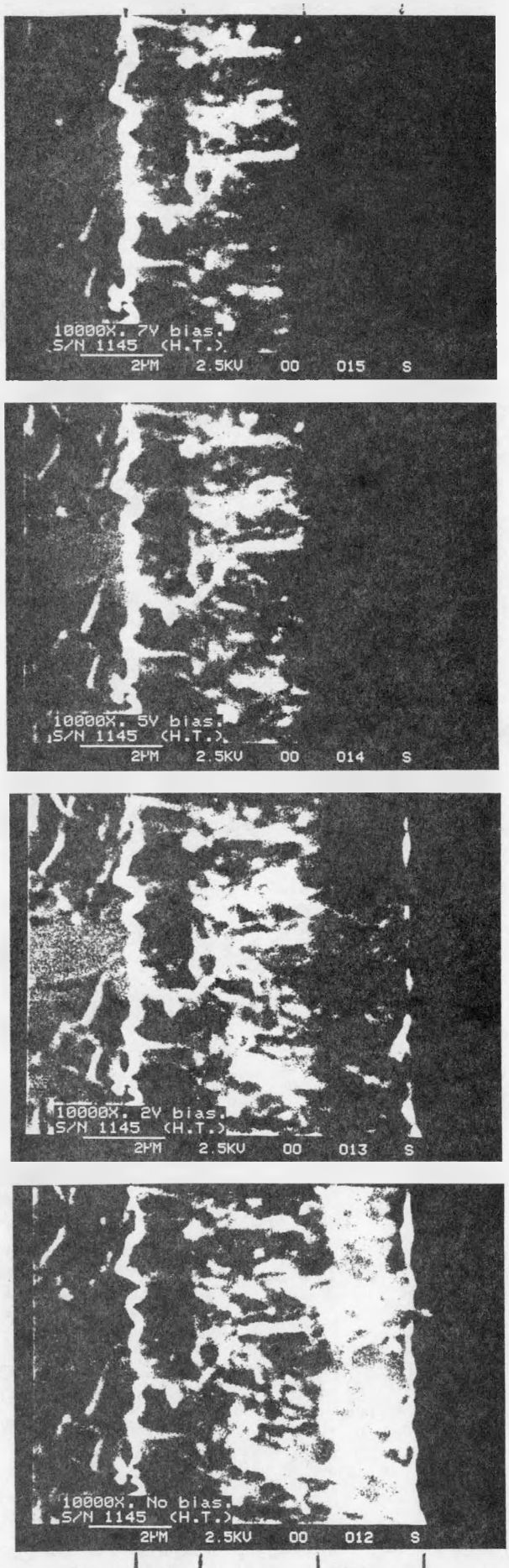

Figure 3.3-7 Voltage Contrast Images of Sample Given Oxygen Heat Treatment. Four Bias Voltages are Shown.

trade-off between image resolution and the contrast change obtainable. At the low electron beam voltages necessary to clearly see contrast changes using a few volts applied to the samples, typically 1-3 kV, image resolution is seriously degraded from that available with the 10-20 kV used for normal secondary electron or EBIC imaging. For this reason although the voltage contrast images are much improved with the new equipment we have not been yet able to refine our estimates of the offset of the electrical junction location, as shown by the voltage transition region, from the metallurgical junction. As in our previous work, however, we still see no offset of greater than 0.5 μm between the two, this being the effective resolution of the voltage contrast images plus the uncertainty in the actual metallurgical junction location.

These measurements show good promise for obtaining more quantitative results from the voltage imaging technique. Further work would have to concentrate on obtaining better cross sections to work with and using the digital image processing capability to obtain true voltage profiles across the junction near region.

In conclusion, we believe that these voltage contrast measurement on etched samples support a heterojunction model for high efficiency, heat treated Boeing $CuInSe_2$/CdZnS cells. Further Voltage Contrast work to define in more detail the voltage profile near the junction will be undertaken when and if equipment capable of resolving the near junction becomes available.

3.3.3 X-ray Absorption, EXAFS and Raman Spectroscopy

One of the major issues in the $CuInGaSe_2$ films is the identity of the nearest neighbors for each of the elements. We has considered two methods during the contract period to explore this question, Raman Spectroscopy and Extended X-Ray Absorption Fine Structure (EXAFS).

The EXAFS measurements on $CuInSe_2$ and $CuInGaSe_2$ samples have been undertaken at Boeing by Farrel W. Lytle of the Boeing Physics Technology Laboratory with the measurements being made at the Stanford Syncrotron Radiation Laboratory. In addition to the EXAFS for near neighbor studies, X-Ray absorption is also valuable as a tool for chemical composition and composition gradient determinations. These techniques and the measurements made to date on both $CuInSe_2$ and $CuInGaSe_2$ are discussed by Farrel Lytle in Appendix C below.

The utility of Raman Spectroscopy for the study of semiconductors derives from its basis in an inelastic phonon-phonon scattering process. An incident excitation photon is absorbed by the material and a photon of different wavelength is subsequently emitted with the difference in energy between the two corresponds to the energy of a lattice phonon which has either been created (Stokes shift) or annihilated (anti-Stokes shift) in the process. Thus Raman spectroscopy provides a purely optical technique for probing the phonon structure of semiconductors.

The technique has been successfully used in the study of a wide range of materials, e.g.: c-Si, μc-Si, α-Si, α-Ge, GaAs, GaAlAs, GaInAs, GaSb, Ge, CdTe, and HgCdTe. It has been applied to many different structures, e.g.: interfaces, epitaxial films, multiple quantum wells, and heterojunctions. Some of the more interesting applications include the study of stress, alloy composition, crystallinity, ion induced damage, and composition fluctuations in alloys. An excellent review article is that of Pollak and Tsu (27).

To our knowledge there is has been only one prior study of Raman scattering from single crystal $CuInSe_2$ surfaces (28) and the results of these measurements appear to be inconsistent with the results of IR absorption measurements subsequently performed by other researchers (29,30).

We have collaborated with Dr. K. J. Ward of Sandia National Laboratories, utilizing the Raman spectroscopy facilities of Professors R. E. Connick and L. Brewer of Lawrence Berkeley Laboratories to perform preliminary measurements on thin film $CdS/CuInSe_2$ heterostructures.

The Stokes emission spectrum acquired is shown in Figure 3.3-8. It clearly shows spectral features at 67, 78, 117, 305, and 607 cm^{-1} from the excitation line, which was at 514.5 nm. The higher energy features at 305 and 607 cm^{-1} have been assigned to the CdS L_0 phonon emission peak and an overtone (31,32,33). The two bands at 78 and 117 cm^{-1} correspond to features previously reported in the single crystal $CuInSe_2$ spectrum (28). The line at 67 cm^{-1} is previously unreported and assignment is still uncertain.

Subsequent to these initial measurements we collaborated with Professor T. M. Loehr of the Oregon Graduate Center for further studies. In view of the inconsistencies between the published Raman and IR data for $CuInSe_2$ the first samples examined in this new study was a piece of p-type single crystal $CuInSe_2$ provided to us by SERI to be used originally

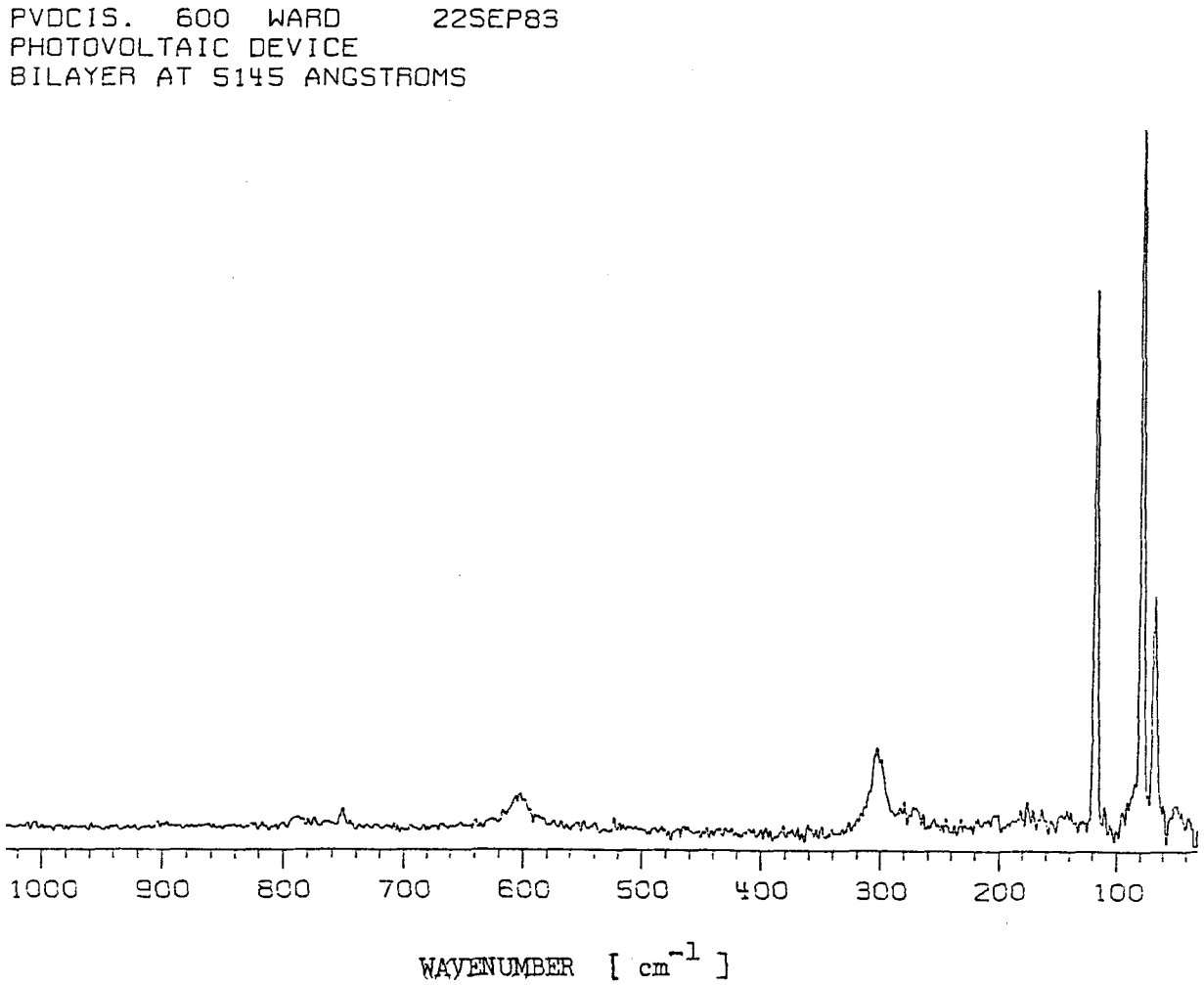

Figure 3.3-8 Raman Scattering Spectrum for Thin Film $CuInSe_2$ Device. The Stokes Spectrum is Shown. Exitation Wavelength was 514.5 nm.

for EDX calibration.

Figure 3.3-9 shows the Stokes spectrum for this single crystal sample acquired under very similar experimental conditions to those used to generate the data of figure 3-6 except that the excitation wavelength was changed to 488.0 nm. Measurements were also performed with excitation wavelengths of 457.9 nm., 514.5 nm, and at 514.5 nm using a 1 nm. bandwidth bandpass filter in the laser output beam. Comparison of the emission spectra in these last two cases showed the complete elimination of the 78 and 117 cm^{-1} peaks when this blocking filter was present in the exciting beam, while both higher and lower energy features persisted. The absence of both lines from spectra taken at e.g. 488 nm. as shown in figure 3-7 also unequivocally identifies them as plasma emission lines from the laser.

We are also dubious of the identification of the 67 cm^{-1} feature in Figure 3.3-8 as a Raman peak since it also corresponds to a tabulated plasma emission line from the Ar_+ laser. However a peak persists in this general wavelength region both when the narrow bandpass filter is used and when the excitation wavelength is changed. We are forced to conclude therefore that a true Raman emission line exists in this region.

The most pronounced spectral peak in Figure 3.3-9 is at ~174 cm^{-1}. Its persistence in all $CuInSe_2$ spectra identifies it as a true Raman scattering peak. We believe it corresponds to the lowest energy A_1 mode of $CuInSe_2$ reported in reference (28) at 186 cm^{-1}. As noted by those authors, since the A_1 mode depends solely on the group VI atom, this transition should be near that of $AgGaSe_2$, reported at 179 cm^{-1} (34).

Further effort to improve the signal to noise ratio in the spectra by extended signal averaging and better collection optics should enable us to determine which of the features of Figure 3.3-9 are Raman scattering peaks characteristic of the $CuInSe_2$. This work would require access to a suitable Raman apparatus for a more extended period than is presently possible. The work will be resumed if such arrangements can be made.

3.3.5 Other Measurements

Extension of the spectral response system to absorption edge intercept (Fowler Plot) studies has shown absorption edge intercepts for the thin-film $CuInSe_2$ devices at energies below 0.95 eV. These results are discussed in detail in the

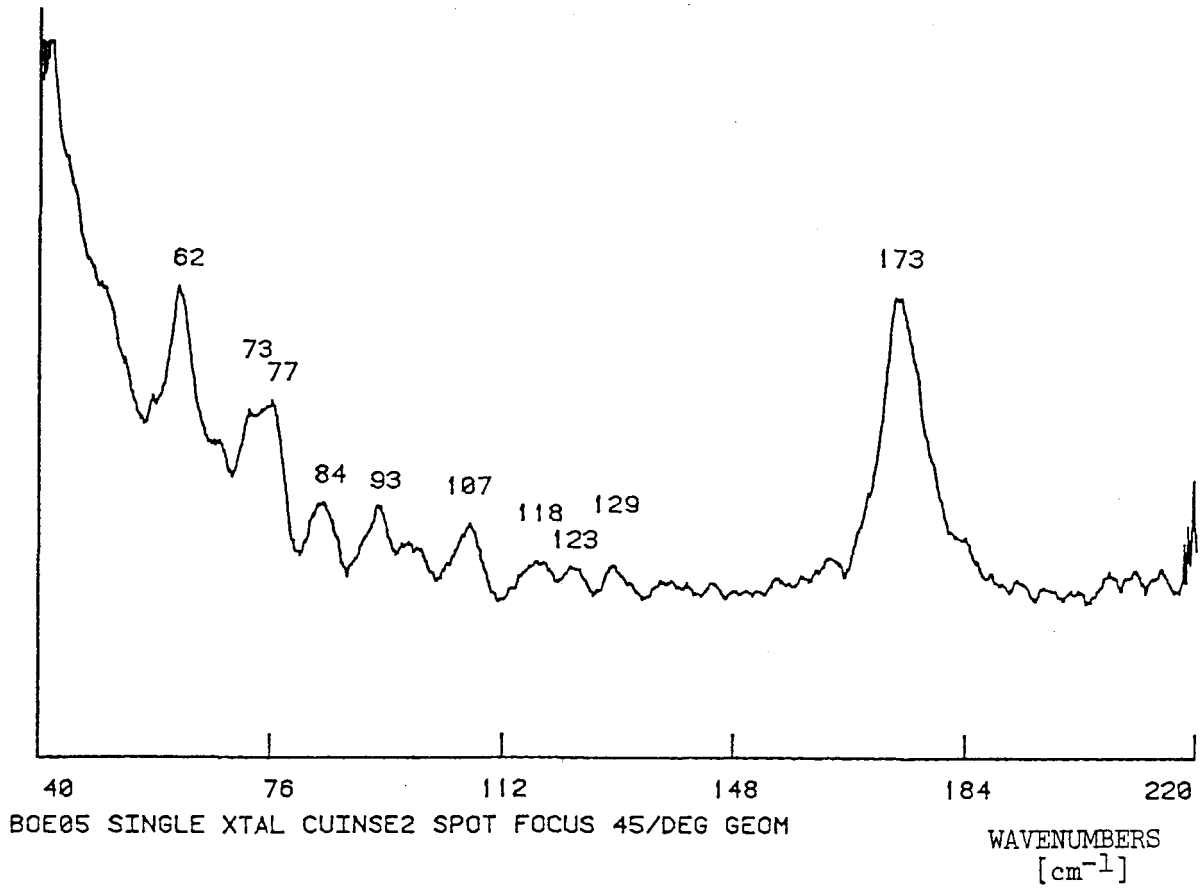

Figure 3.3-9 Raman Scattering Spectrum for p-type $CuInSe_2$ Single Crystal Sample (Stokes Spectrum). Excitation Wavelength was 488 nm. Note that Scale is Reversed From Figure 3-8.

second and third quarterly reports (7,8). Junction modification experiments using cesium treatments, ion etching, and chemical etching are described in the semiannual report (7).

3.4 Selenium Vapor Composition Effects

The electronic transport properties of the present $CuInSe_2$ films and $CuInSe_2$/CdZnS devices are known to be far from optimum. Improvements in, e.g., electron mobility or in molybdenum/selenide contact properties would lead directly to better device performance.

Attempts to influence selenide film properties using parameters of the deposition process have met with mixed success. Film conduction type and resistivity is controlled using the Cu/In flux ratio during deposition to vary that same ratio in the films. However attempts to systematically vary film properties using the selenium source have been much less successful. At present the selenium is thermally evaporated from an open, resistively heated tungsten boat. The selenium charge is only partially liquid, the evaporation is occurring from the liquid at its melting point.

Previous experiments at Boeing have attempted to use several other vapor source designs for the selenium. In spite of nominally identical deposition conditions and final sample compositions for the $CuInSe_2$ films, these alternate sources resulted in very different photovoltaic performance in the final devices. In particular, experience showed that good films could not be made using a radiantly heated solid selenium source,the deposition process being otherwise unchanged from the normal. These results when coupled with the well known allotropy of selenium vapor suggest that the molecular species incident on the growing surface may depend on details of source design and in turn profoundly effect the electronic transport properties. Ample precedent for such an effect is available from experience with Molecular Beam Epitaxy (MBE) grown GaAs, both experimental (35,36) and theoretical (37,38). The use of a high temperature "cracking cell" in series with the effusion type arsenic sources is now common in commercial MBE systems for GaAs.

The effusion cell is one limiting case where equilibrium thermodynamics can be used to gain insight into the distribution of molecular species in the vapor. In the limit where the emission orifice is small compared to the area of the vapor/container interface then the vapor loss through the

orifice does not significantly effect the equilibrium within the cell. Detailed modeling for Se was done by Rao (39) with the result that the heavy polymers Se_6, Se_5, and Se_7 predominate for temperatures less than approximately 700°C, well above the temperatures at which we operate the present sources.

The reaction of Cu and In adatoms on the growing film surface with these large selenium polymers is probably very complex but their dissociation prior to incorporation into the lattice is a necessary step in any likely mechanism. The apparent sensitivity of the growth process to the molecular distribution of the selenium vapor incident on the surface is evidence that this dissociation step may represent an activation energy barrier to the overall reaction. Modification of the distribution to favor smaller molecules or the monomer may then reduce that barrier.

Various methods have been explored for predissociating the selenium. Calculations using Rao's model indicate that very high temperatures would be required to thermally dissociate the selenium with resulting problems of source design and control. Optical dissociation, while possible, was considered impractical and not easily scaled. Electron Dissociative Attachment in the chalcogenides has been utilized by Fain and Schrott (40) to induce low temperature thermal nitridation of silicon in UHV. A detailed study by W. Simon (41) of the energy dependence of the cross section for electron capture in sulfur and selenium showed that the higher polymers of both elements had large cross sections for thermal electrons in the gas phase. Rather than attempt to build a practical source using crossed electron and molecular beams as these researchers did, however, it was decided that a plasma discharge could be utilized as the electron source and interaction medium.

Two plasma excitation techniques exist applicable where a high density of thermal electrons ($E \leq 4$ eV) is desired. RF heating as used by Chang and coworkers at Bell Laboratories (42) has the advantage of direct coupling to the plasma ions but is complicated to implement. We have chosen to use an experimentally simpler method employing a thermal electron emitter to sustain a DC plasma discharge.

The source design used to test these concepts is shown in figure 3-10. It is modeled closely on the design employed by Rockett and coworkers (43) for a solid-metal ion source intended for accellerated-ion doping experiments in MBE. The accelerating grid will not be used in our initial experiments. The source is constructed from tantalum, nickel,

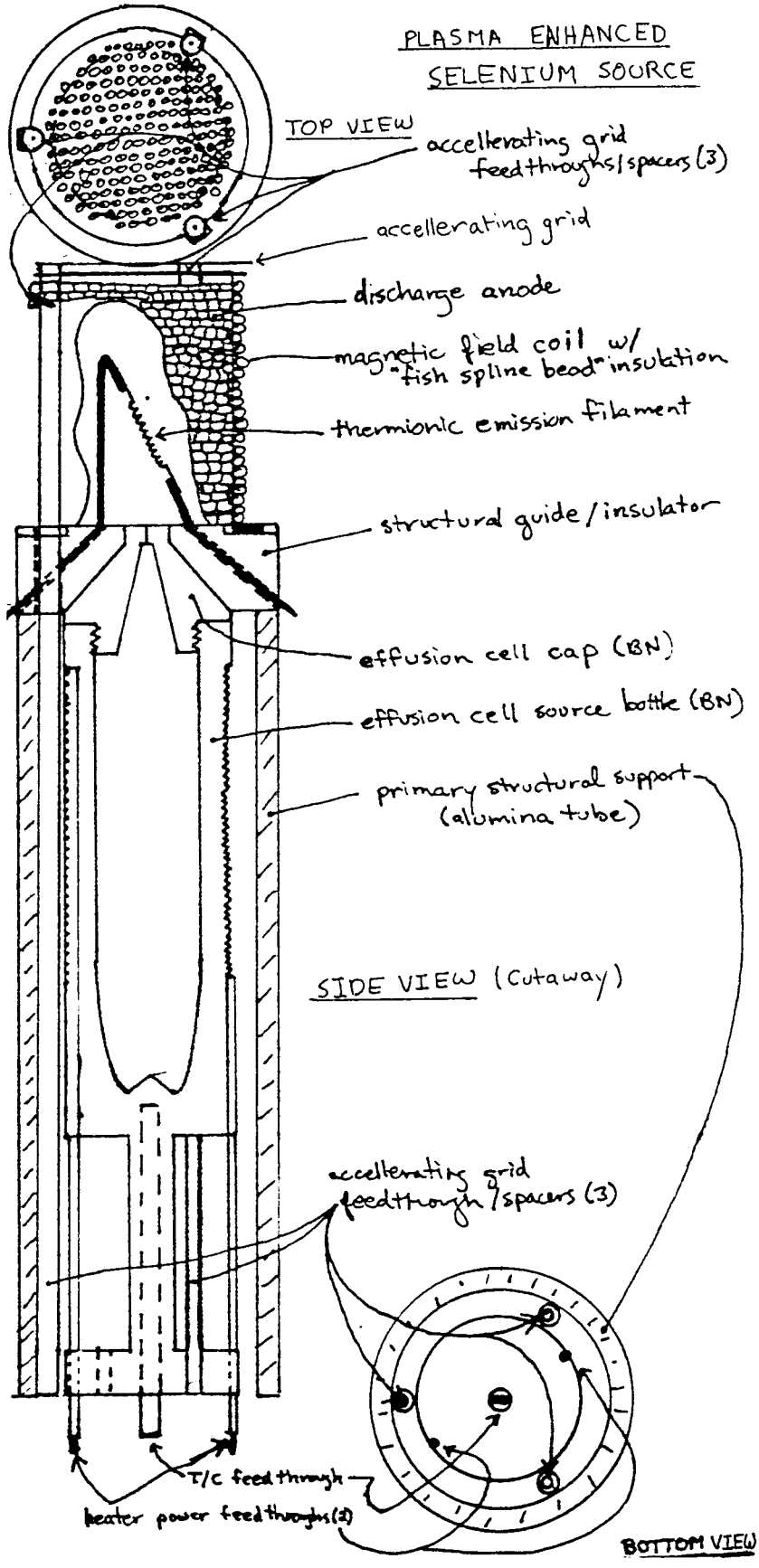

Figure 3.4-1 Drawing of Proposed Selenium Source Design

alumina, boron nitride, and a thoriated tungsten filament. Graphite was deliberately excluded to avoid potential problems from CSe_2 formation.

Only initial tests of the source were completed during this contract period. The source easily achieved the rates desired for use in the CIS deposition process. However it was found that excessive system pressures were required to sustain the plasma discharge in the source. Decoupling the plasma discharge chamber pressure from the system pressure will require the design and fabrication of a new accelerating grid. Further development work on this Se source has therefore be delayed until this can be done. Subsequent research plans then call for a source of this type to be incorporated into one of the $CuInSe_2$ deposition systems and used to prepare $CuInSe_2$ films.

3.5 Electron Gun Evaporated Films

Besides sputtering, the film preparation technique which would appear to have the greatest applicability to the deposition of reproducible mixed CdZnS films, alternate window layer materials, composite window layers, and antireflection coatings is that of electron gun evaporation. As the materials for these device applications are all compounds, normal thermal evaporation leads to dissociation and formation of non-stoichiometric films. Electron gun evaporation has been found to minimize the dissociation problem and has been successfully utilized in the preparation of complex alloy and compound thin-film layers. The technique has the additional advantage, in comparison to sputtering, of minimal substrate heating associated with the deposition process and the relative ease of controlling the substrate temperature at some predetermined value. Low as well as controllable substrate temperatures were especially important due to possible diffusion into the selenide layer.

A large pocket, multi-hearth electron gun source was acquired and installed in the vacuum chamber used for the thermal evaporation of the mixed sulfide films. Provisions for X-Y beam sweeping were included to aid in the evaporation of semiconductor or dielectric materials. Furthermore, to minimize excessive particulate emission and outgassing problems during the electron gun evaporation process, all source materials were acquired in the form of large sintered chunks instead of the more usual powders or small diameter particles.

The first material evaporated with the gun was CdS. A rather low deposition rate of 5nm/sec was used in an effort to avoid random shutdowns of the gun during the deposition of the 3 micrometer thick film. The films were deposited onto alumina and Corning type 0211 glass substrates heated to 175-200°C.

The e-gun deposition CdS films were found to be of very good optical and structural quality. Sheet resistivity was, however, higher than for films prepared by the normal thermal evaporation process and could not be measured with the standard four-point probe. In spite of this observation, development of the e-gun process was continued by investigating films co-deposited with In for a low resistivity dopant. Films with sheet resistivities of less than 20 ohm/square were readily produced with good repeatability and control.

As a further indicator as to the quality of the e-gun deposited CdS, these films were used to fabricate CIS/CdS cells. Like the standard process, the initial CdS in contact with the selenide (~0.6 micrometer thickness) was deposited without In. Other cell fabrication steps were identical to those used for the standard CdS process.

The I-V performance under ELH lamp illumination ($100mW/cm^2$) of a $1cm^2$ cell resulting from e-gun CdS deposition is shown in Figure 3.5-1. The performance is seen to be very good with a 8.8% conversion efficiency. The voltage and current were also excellent for a straight CdS cell and compare very favorably with the thermally evaporated sulfide. Since the e-gun evaporation process for CdS deposition was successful, the more significant development of CdZnS deposition was initiated using mixed CdZnS source material with 20% Zn content.

As was the case for the e-gun evaporated CdS, the resulting mixed sulfide films were of good optical and structural quality with excellent thickness uniformities over large areas (4x8 inches) but were of higher sheet resistivities than films produced by thermal evaporation from apertured crucibles. The process appeared to be quite reproducible and the film composition was determined to closely track that of the source material. EDX composition measurements on films deposited with the 20% ZnS source material revealed a ZnS concentration of 21%.

Further experimentation with the material did, however, uncover a serious limitation with respect to the intended device application. Unlike the CdS depositions, the In-doping process was not found capable of preparing the

10/9/1985 09:44:59
BAC SAMPLE: S250-4C
TEMPERATURE: 25.0 Deg C
UNIT CELL Area 1.000 cm^2
Total CELL Area 1.000 cm^2
No. cell in series = 1.00
No. of cell in parallel = 1.00
Base type is P type
REMARK:

CURVE#	INTENSITY (mW/cm^2)	EFFICIENCY (%)	VOC (Volt)	ISC (Amp)	VMAX (Volt)	IMAX (Amp)	FILL FACTOR
1	100.00	8.82	.4211	3.2138E-02	.314	2.805E-02	.6515

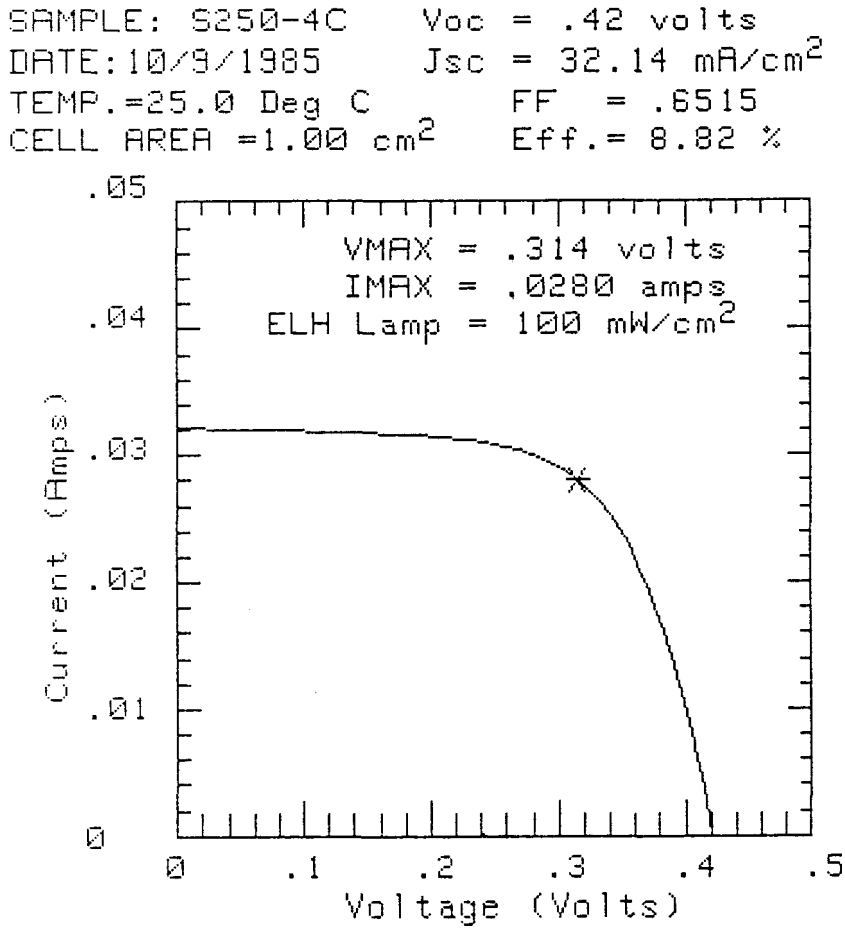

Figure 3.5-1 I-V Characteristic of Non-AR-Coated $CuInSe_2$ Cell with Electron-Gun Evaporated CdS.

mixed sulfide films with the required sheet resistivities of less than 25 ohm/square. The lowest attainable resistivity even with substrate temperature, deposition rate, and In concentration variations was around 60 ohm/square.

To overcome the high resistivity problem, new material was acquired with a lower Zn content (13% ZnS). Processes were subsequently developed which demonstrated the preparation of In-doped films with sheet resistivities of 15-25 ohm/square. Consequently, this material and process were adopted as the standard for the majority of the cell preparation activities. The general ease of the process, compositional uniformity within and normal to the film plane, reproducibility, and thickness uniformity were believed to greatly outweigh such negative factors as source material costs and a higher, undoped resistivity.

In addition to the sulfide studies, the electron gun was used to deposit SiO_2 films for antireflection coatings. Fused quartz disks served as source material and the films were deposited at a 1nm/sec deposition rate onto unheated substrates.

Since films of 100nm thickness deposited onto glass substrates displayed excellent optical clarity and uniformity, the process was applied to CIS/CdS and CIS/CdZnS cells. After completing a series of depositions of varying film thicknesses and observing the particular color generated by the AR-layer, a 93nm thick deposit was selected as producing the desired, deep magenta color. Films of this thickness were then deposited onto cells of reasonably good quality to determine how effective these AR films were and whether the gun deposition process resulted in any cell degradation. Before and after results from one $1cm^2$ are shown in Figures 3.5-2 and 3.5-3 for xenon lamp simulator illumination at a $135mW/cm^2$ intensity. The current increase of 15% was comparable to the increase obtained previously with reactively evaporated SiO and in no instance was the process detected to cause cell degradation.

3.6 Fabrication of High Efficiency $CuInSe_2$/CdZnS Devices

3.6.1 Antireflection Coatings for CdZnS/$CuInSe_2$

Attainment of the highest efficiencies that the $CuInSe_2$/CdZnS cell is capable of requires effective antireflection coatings on the exposed CdZnS surface. In the simplest planar optical

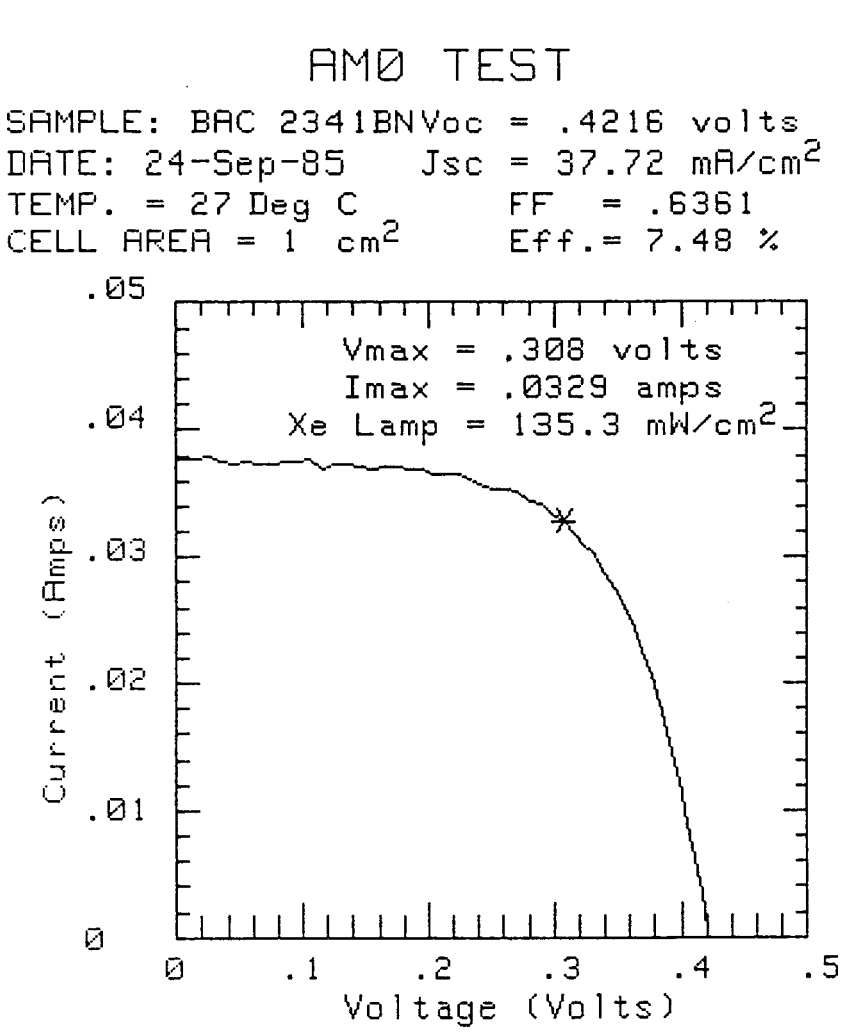

Figure 3.5-2 I-V Characteristic of $CuInSe_2$/ZnCdS Cell Before AR Coating.

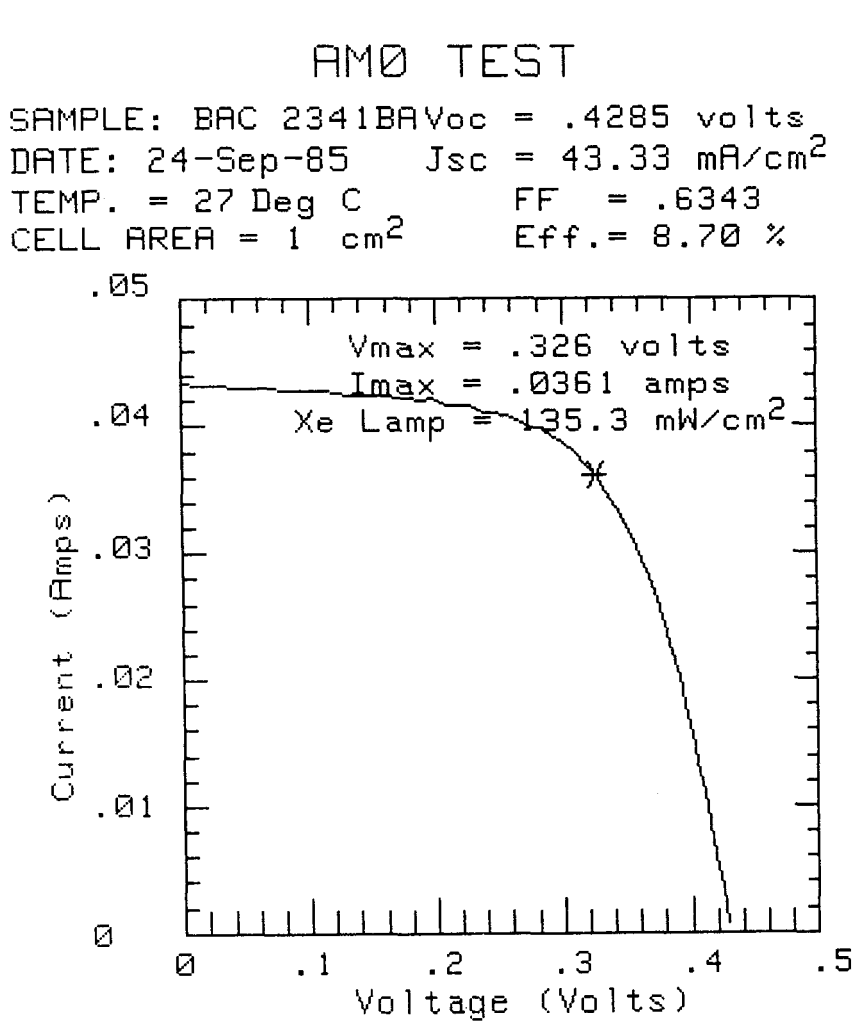

Figure 3.5-3 I-V Characteristics of $CuInSe_2$/ZnCdS Cell After Coating with SiO_2 AR.

model (44) the reflection losses of an uncoated air/CdZnS interface are expected to be approximately 17%, varying slightly with the sulfide composition and the assumed weighing functions for the incident spectrum and the device internal spectral response. In this initial survey of AR systems these effects can be ignored, although they become important when actually optimizing the coatings. The optical model of the cell can also be simplified by ignoring the additional reflection at the CdZnS-$CuInSe_2$ interface since the refractive index mismatch between the sulfide (n = 2.4 - 2.6) and the selenide ($n^2 + k^2 \sim 2.8 - 3.0$) is small. Because the sulfide is thick in our cells (~3.0 μm) and the CdZnS-$CuInSe_2$ interface is irregular the refection at the sulfide-selenide interface is incoherent with respect to that at the sulfide-air interface and the two can be treated independently.

We believe the present Boeing cells are well described by the planar air-sulfide interface model described above. Therefore, if we ignore the dependence of open circuit voltage and fill factor on light generated current density the correction for the reflection loss would be a 20% increase in short circuit current and efficiency for these cells. However, since surface contamination or texturing can significantly reduce the reflection losses, it is not very convincing to simply assume this correction. To accurately assess the actual reflection correction for a device would require measurement of the diffuse and specular reflection losses versus wavelength, correction of these results for the reflection from the grid and bus structure, and convolution with the incident light spectrum and device internal spectral response. At present this is not possible with the accuracy necessary for an effect as large as 20%. The alternative and more practical procedure is to apply an effective antireflection coating to the cell and directly measure a close approximation to the zero reflection case.

Table 3.6-1 lists several AR systems which have either been used on CdZnS/$CuInSe_2$ cells in the past or have been considered during this work. Fig. 3.6-1 shows the calculated reflectance versus wavelength curves for these systems using the simple non-dispersive planar multilayer model reflection model (45). Also included are optimized one and two layer AR coatings for a substrate of refractive index 2.4. All layers are of optical thickness $\lambda_0/4$. λ_0, or equivalently layer thickness, is a parameter available for actual film optimization. For a given double layer AR system unequal optical thickness for the two layers are a possibility but in general will not improve on the equal thickness case. We will consider only the simpler, equal layer thickness case here.

Table 3.6-1

Possible Antireflection Systems for Use on $ZnCdS/CuInSe_2$ Cells

Single Layer Systems	Index of Refraction
Optimum	1.55
SiO_x (slow deposition)	1.6
MgF_2	1.38
Double Layer Systems	**Indices of Refraction**
Optimum (see ref. 8)	1.34/1.80
MgF_2/SiO_x	1.38/1.76
MgF_2/ITO	1.38/2.0

Table 3.6-2

Results of Single Layer MgF_2 AR Coating, Thickness 1100A. MgF_2 Deposition Done at SERI, I-V Tests Done at SERI Testing at AM1½ Equivalent, 28°C

	I_{SC} (mA)	V_{OC} (Volts)	FF	R_{SHUNT} (K)	E_{FF} (%)
1117A					
Before AR	33.04 mA	.4305	.671	.754	9.2
After AR	36.67 mA	.433	.665	.411	10.2
	I_{SC} increase:	11.0%			
1114B					
Before AR	34.68	.408	.628	80	8.6
After AR	38.83	.408	.626	145	9.6
	I_{SC} increase:	12.0%			
1113C					
Before AR	34.95	.402	.621	.271	8.4
After AR	38.80	.406	.625	.285	9.5
	I_{SC} increase:	11.0%			

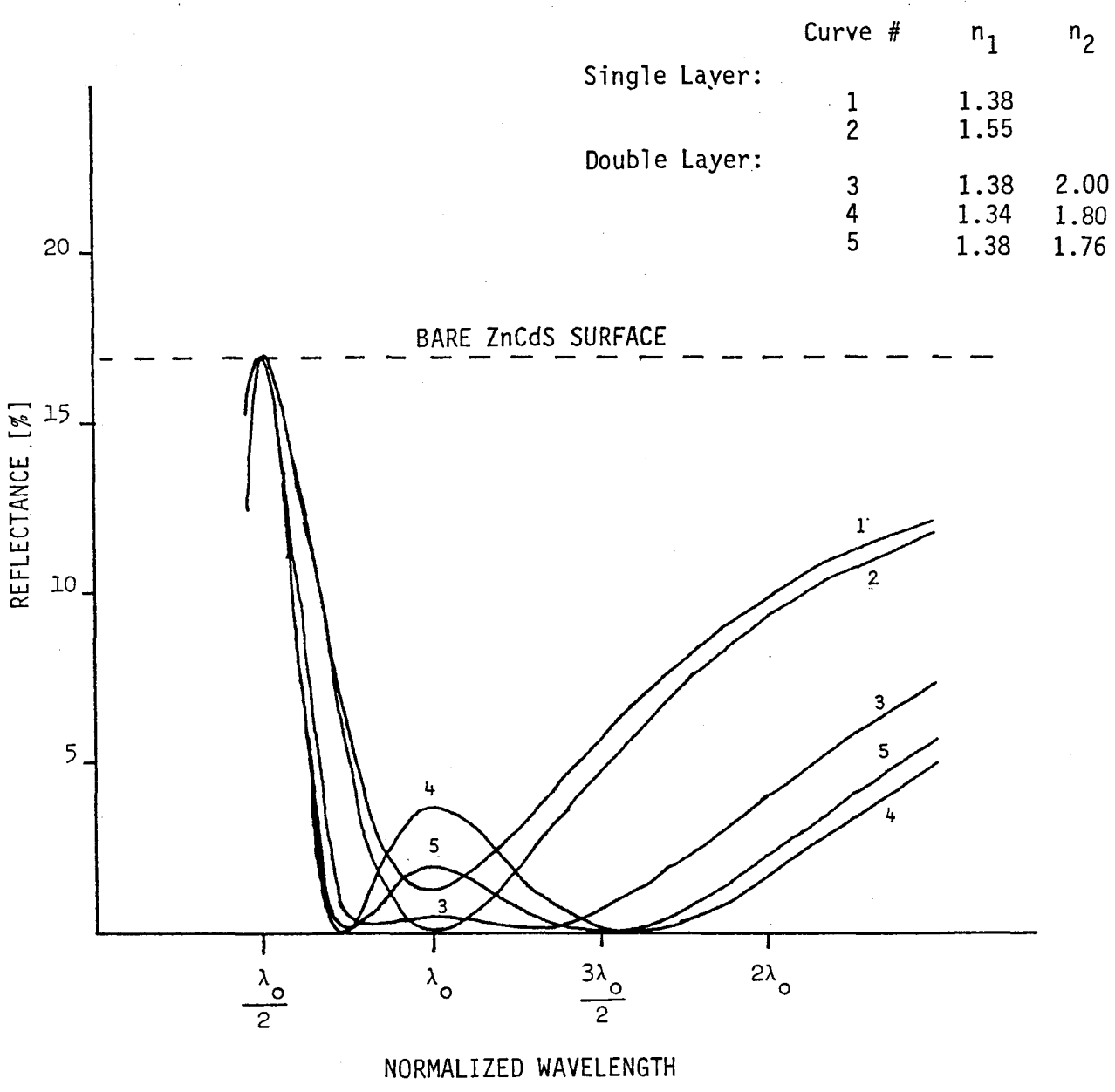

Figure 3.6-1 Reflectance as given by the multilayer thin film model of Reference 9, section 4.9 versus incident wavelength, for the single and double layer AR systems of Table 3-1. Single layers and both layers of double layers are of optical thickness $\lambda_o/4$. Substrate refractive index of 2.4 and no dispersive effects are assumed.

Single layer quarter wavelength coatings of SiO_x (2>x>1 possible but for transparent AR coating 1.76>x>1.55) have been used in the past on $CdZnS/CuInSe_2$ and gave approximately 12% increase in current, consistent with a near optimum single layer AR as shown. The highest efficiency thin film $CuInSe_2$ cell reported previous to the work here used this coating. Since the index of refraction of the SiO_x used for AR coating is variable but normally above 1.6 the actual reflectance curve of the film used probable lay somewhat above the optimum curve given.

During this contract three Boeing cells were coated with single layer MgF_2 by R. Noufi of SERI using $\lambda_0 \sim 600$ nm. The results are given in Table 3.6-2. Current increases of 11-12% were obtained and confirm that our estimate of 17% uncoated reflection losses is reasonable.

The advantage of the double layer AR coatings over the single layers is obvious from Fig. 3.6-1. We estimate that the reflection losses can be reduced to 3-4% overall with the two layer AR. Unlike the single layer case there is no unambiguous optimum indices of refraction for the two layer system when the reflectance calculation involves a weighing function. Instead, the differences among the various two layer systems are trade-offs of bandwidth versus flatness over the passband. No choice can be made among the curves of Fig. 3.6-1 based solely on the reflectance curves. The curve labeled "optimum" in Table 3.6-1 is simply that giving minima which are true zeros in reflectance and is the unweighed reflectance minimum.

The system MgF_2/ITO was tried using sputtered ITO deposited in one of the same systems used for the alternate n-layer development work but with the ITO stoichiometry adjusted to give insulating material. However cell exposure to the plasma in this system resulted in severe shunting in almost all cases.

The system MgF2/SiO_x was used on the high efficiency 1 cm^2 cells and the results will be described below.

The system SiO:H/SiN:H has recently been developed both for the large area cells and for the high efficiency $CuInGaSe_2$ devices. This system has the advantage of being deposited entirely by the PECVD process and is discussed in the sections of this report dealing with these two types of devices.

3.6.2 High Efficiency $CuInSe_2/CdZnS$ Devices

During this contract period the main effort in improving the efficiency of the $CuInSe_2/CdZnS$ devices has gone toward understanding the role played by the $CuInSe_2$ composition and composition gradients in determining device characteristics. Coupled with these issues is the effect of the 225°C bake in oxygen used in cell optimization, since the effect of this treatment depends strongly on the composition.

In the process of these studies several groups of cells have been produced which showed excellent efficiencies and therefore were further optimized by applying AR coatings after the designs given above. The results on these cells were excellent, as shown in Table 3.6-3 and will be described below.

Explanations of many of the individual experiments performed during the contract period will found in the five previous technical progress reports issued under this contract (6-10).

As the initial step in this study, a set of substrates was prepared as a deliberate selenide composition variation experiment. Table 3.6-4 lists the selenide composition as determined by EDX for the four substrates involved which, on the basis of previous experience, were within the range of composition judged to yield reasonable devices. These were therefore fabricated into cells. Also listed are the hot probe measurements made on these samples.

Substrate 1114 is, relatively, Cu rich and strongly p-type. Substrate 1113 is, relatively, Cu poor and in the as-made state was of high resistivity and spatially mixed in type. The absolute composition numbers in Table 3.6-4 are good to no better than +/-5% of reading but the data was deliberately taken under comparible conditions so relative comparisons between them are much more reliable. Table 3.6-5 shows the results of our EDX composition measurement on a polished single-crystal $CuInSe_2$ sample supplied by SERI, compared with their microprobe (WDX) data. Using the microprobe measurements as a standard, our EDX measuremets would appear to give selenium values too low (by 1.5% of total) and indium values too high (by 1.4% of total). Table 3.6-4 has not been corrected for this difference.

The selenide surface morphologies for the substrates listed in Table 3.6-4 are shown in Fig. 3.6-2a & b. These SEM images were taken after CdZnS deposition and subsequent chemical stripping. Large differences are clearly seen between 1113 and the others, consistent with the morphology differences

Table 3.6-3

I-V Characteristics for Cells from Three Substrates 1105, 1117, 1118

Cell #	Eff %	V_{oc} (V)	J_{sc} (mA/cm^2)	V_{mp} (V)	J_{mp} (mA/cm^2)	FF	R_{Shunt} (KΩ*cm^2)	Test Conditions
1105A	9.84	.418	34.6	.330	29.9	.681	57.5	25°C Xenon
1105B	9.73	.415	34.7	.309	31.5	.677	35.6	25°C Xenon
1105C	9.90	.420	34.3	.315	31.4	.689	53.8	25°C Xenon
1105D	9.85	.415	35.4	.317	31.1	.671	57.1	25°C Xenon
	Note: All after 225°C 0_2 10 min HT							
1117A	9.95	.436	33.7	.340	29.3	.678	--	25°C ELH
1117B	10.03	.429	34.3	.331	30.3	.682	57.3	25°C Xenon
1117C	10.05	.425	34.5	.331	30.3	.686	137.6	25°C Xenon
1117D	10.11	.432	34.2	.344	29.4	.684	4.9	25°C Xenon
	Note: 1117A after 225°C 0_2 20 min HT. Others 10 minutes							
1118A	9.28	.442	32.6	.331	28.0	.643	--	23°C ELH
1118B	9.62	.435	33.2	.331	29.1	.665	--	23°C ELH
1118C	9.52	.438	32.9	.331	28.8	.661	--	23°C ELH
1118D	9.65	.436	33.1	.337	28.6	.670	--	23°C ELH
	Note: 1118A after 225°C 0_2 20 min HT. Others 10 minutes							

Table 3.6-4

EDX Composition and Hot Probe Results for Four Recent Substrates
All Selenide Layers ~3.3 μm Thick

Substrate #	1113	1114	1117	1118
EDX Composition (Atomic %)				
Cu	23.2	25.1	23.4	23.9
Se	48.6	48.6	48.9	48.5
In	28.2	26.3	27.7	27.6
Hot Probe: Layer as made:	30nA _ 30nA "N" "P"	200-2000nA "P"	100nA "P"	30-60nA "P"
After device fabrication:	Not measured	Not measured	80nA "P"	70-80nA "P"

Notes: Hot probe ranges indicate variation across substrate
EDX % error: Cu 1.3 atomic %
Se 2.8 atomic %
In 1.0 atomic %

Table 3.6-5

EDX Calibration Check Against SERI Supplied $CuInSe_2$
Single Crystal Standard. In Atomic %

	SERI (10 runs)	Boeing (3 runs)
Cu	24.01-24.17	24.11-24.17
In	25.25-25.38	26.71-26.89
Se	50.49-50.68	49.00-49.12

seen before in the highly copper deficient selenide films.

Neither substrate 1113 (highly copper deficient) nor 1114 (relatively copper rich) resulted in devices as good as those made from substrates 1117 and 1118, as shown in table 3.6-6. One strong effect seen with materials like 1113 is the relatively good photovoltaic parameters in the post fabrication, before heat treatment curves when compared with those of much more p-type material like 1114. We should point out that all of this material, including 1113, will read strongly p-type on the hot probe after the 225°C oxygen bake. However, little improvement in the photovoltaic parameters is seen in cells made from 1113 after the oxygen bake, while 1114,1117 and 1118 all show improvement in V_{oc} and curve fill factor. This variation with material composition is fundamental in any heat treatment experiment.

In section 3.6.1 above we discussed several possible improved antireflection systems for the $CuInSe_2/CdZnS$ cell. One of the highest efficiency cells (1117A) was coated with MgF_2 at SERI. Figs. 3.3-3 and 3.6-4 show the I-V characteristics as taken at Boeing before and after the coating. The slight decrease in fill factor is explained by an increase in the light independent shunt leakage which the cell developed. This cell measured 11.15% efficient under the normal test conditions used at Boeing.

The two layer system MgF_2/SiO_x was applied to some of the best cells for us by Dr. John C. Fan of MIT/Lincoln Laboratories and his coworkers. The composition of the SiO_x layer deposited from thermally evaporated SiO starting material can be varied from near SiO_2 with index of refraction near 1.6 to near SiO with index above 1.9. SiO_x can be prepared with good transparency only up to an index of refraction of approximately 1.75. Films with stoichiometry closer to x=1.0 (indices above 1.75) are highly absorbing. For the MgF_2/SiO_x on CdZnS system we require the index of the SiO_x to be as high as possible. In addition, modeling of the two layer AR systems shows that while the integrated reflectance is only mildly sensitive to the exact thicknesses of the two layers, it is extremely important that the two layers be of equal optical thickness. The AR layers were therefore deposited at MIT/LL using equipment specifically set up for such optical coating work. Design simulations and reflectance measurements done at MIT/LL resulted in a design using λ_0=590 nm. and with the index of refraction of the SiO_x approximately 1.75. The index of the MgF_2 is essentially fixed at 1.38. The actual film used is therefore the same as that modeled in curve 5 of Fig. 3.6-1.

Table 3.6-6 I-V Parameters Before and After Heat Treatment for Cells Made on Substrates Listed in Table 3-4.

Before Heat Treatment

Cell		Eff	Voc [V]	Jsc [mA/cm^2]	Vmp [V]	Jmp [mA/cm^2]	FF	R Shunt [KΩ*cm^2]	Test Conditions	
1113	A		.405	34					23°C	E
	B			no test — grid problem						
	C	8.47	.398	35.4	.298	28.4	.601	0.12	25°C	X
	D	8.40	.395	35.1	.297	28.3	.607	0.18	25°C	X
1114	A		.320	34						
	B	4.67	.317	34.5	.203	23.0	.427	0.07	25°C	X
	C	2.20	.204	30.2	.118	18.7	.358	0.58	25°C	X
	D	2.49	.203	31.6	.120	20.7	.388	0.29	25°C	X
1117	A		.380	34					23°C	E
	B		.380	35					23°C	E
	C		.380	35.3					23°C	E
	D		.375	35					23°C	E
1118	A		.400	34					23°C	E
	B		.400	34					23°C	E
	C		.400	34					23°C	E
	D		.400	34					23°C	E

After Heat Treatment

1113	A	8.67	.406	32.0	.320	27.1	.668	89.0	25°C	X
	B		no test —	grid	problem					
	C									
	D									
1114	A	9.01	.412	34.9	.308	29.2	.628	74.2	25°C	X
	B	8.66	.398	34.7	.292	29.7	.626	42.3	25°C	X
	C									
	D									
1117			See	Table	3-3					
1118			See	Table	3-3					

E - ELH Tester

X - Xenon Solar Simulator

TEST
6/12/1985 13:39:05
BAC SAMPLE: 1117A
TEMPERATURE: 25.0 Deg C
UNIT CELL Area 1.000 cm^2
Total CELL Area 1.000 cm^2
No. cell in series = 1.00
No. of cell in parallel = 1.00
Base type is P type
REMARK:

CURVE#	INTENSITY (mW/cm^2)	EFFICIENCY (%)	VOC (Volt)	ISC (Amp)	VMAX (Volt)	IMAX (Amp)	FILL FACTOR
1	100.00	9.95	.4357	3.3682E-02	.340	2.927E-02	.6777

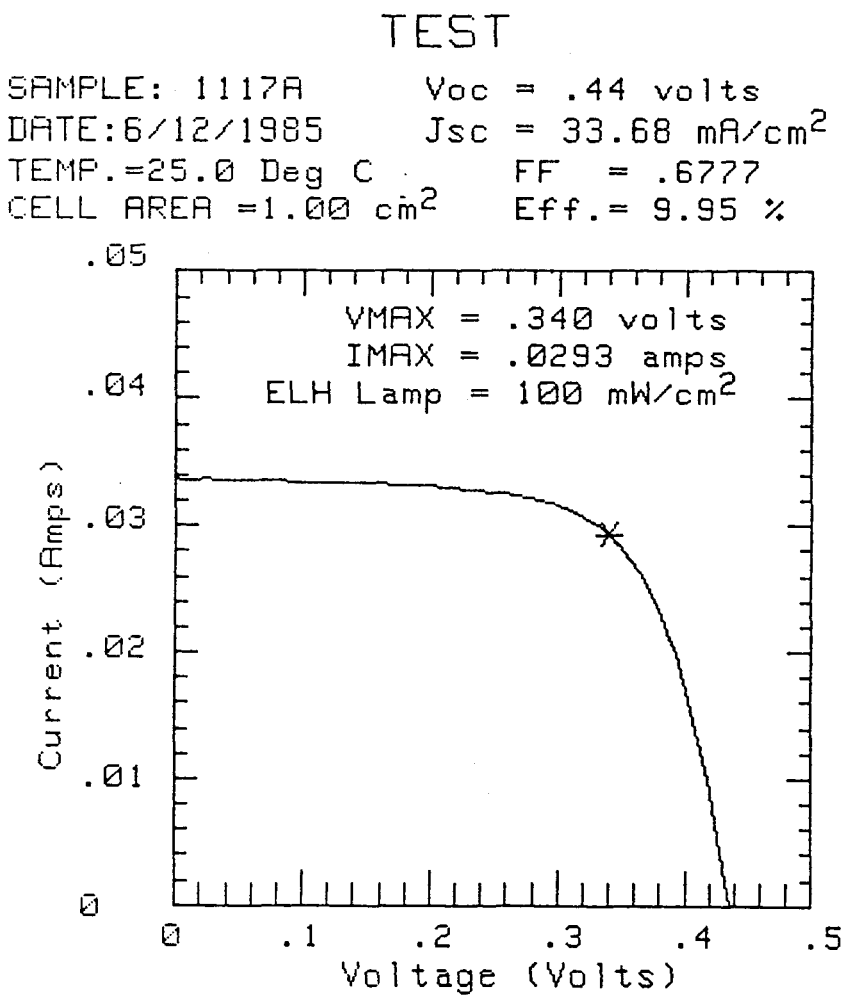

Figure 3.6-3 I-V Characteristics of Cell 1117A Before AR Coating.

TEST
7/1/1985 10:29:31
BAC SAMPLE: 1117A
TEMPERATURE: 25.0 Deg C
UNIT CELL Area 1.000 cm^2
Total CELL Area 1.000 cm^2
No. cell in series = 1.00
No. of cell in parallel = 1.00
Base type is P type
REMARK: AFTER MgF/SERI

CURVE#	INTENSITY (mW/cm^2)	EFFICIENCY (%)	VOC (Volt)	ISC (Amp)	VMAX (Volt)	IMAX (Amp)	FILL FACTOR
1	100.00	11.16	.4396	3.8064E-02	.335	3.329E-02	.6667

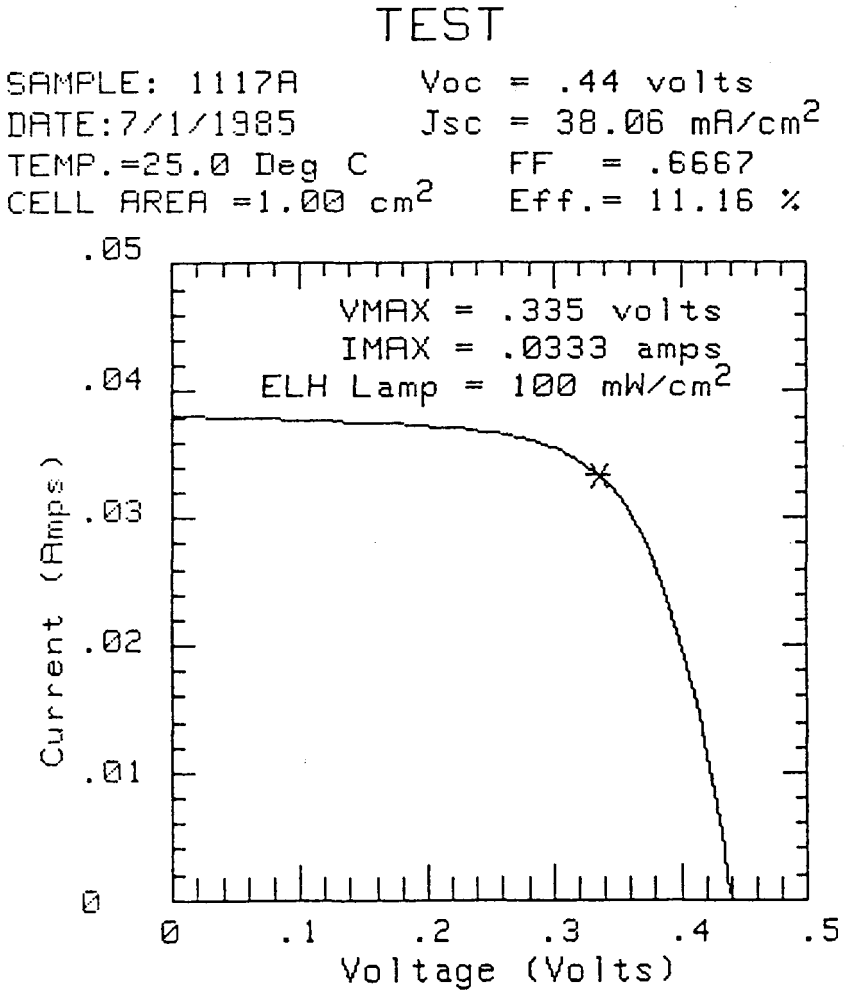

Figure 3.6-4 I-V Characteristic of Cell 1117A After MgF_2 AR Coating Done at SERI

TEST
7/24/1985 12:14:01
BAC SAMPLE: 1117B
TEMPERATURE: 25.0 Deg C
UNIT CELL Area 1.000 cm^2
Total CELL Area 1.000 cm^2
No. cell in series = 1.00
No. of cell in parallel = 1.00
Base type is P type
REMARK: AFTER MIT AR

CURVE#	INTENSITY (mW/cm^2)	EFFICIENCY (%)	VOC (Volt)	ISC (Amp)	VMAX (Volt)	IMAX (Amp)	FILL FACTOR
1	100.00	11.63	.4387	3.8811E-02	.339	3.428E-02	.6831

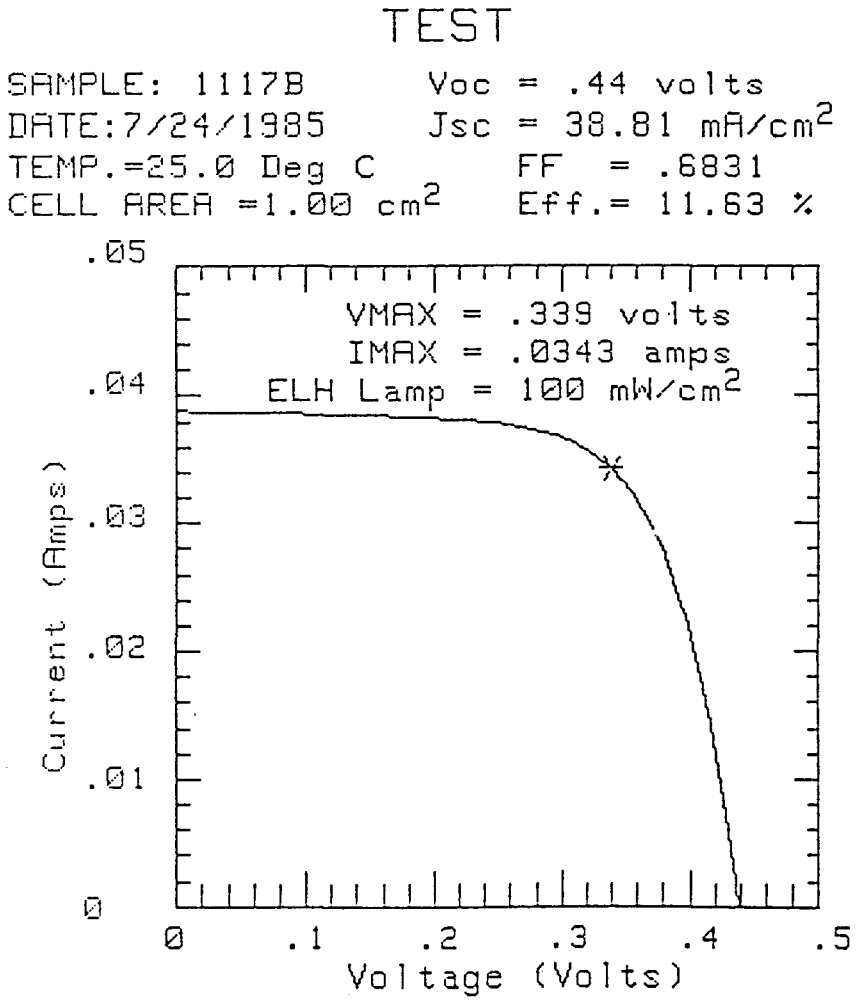

Figure 3.6-5 I-V Characteristic For Cell 1117B After AR Coating. ELH Illumination was used.

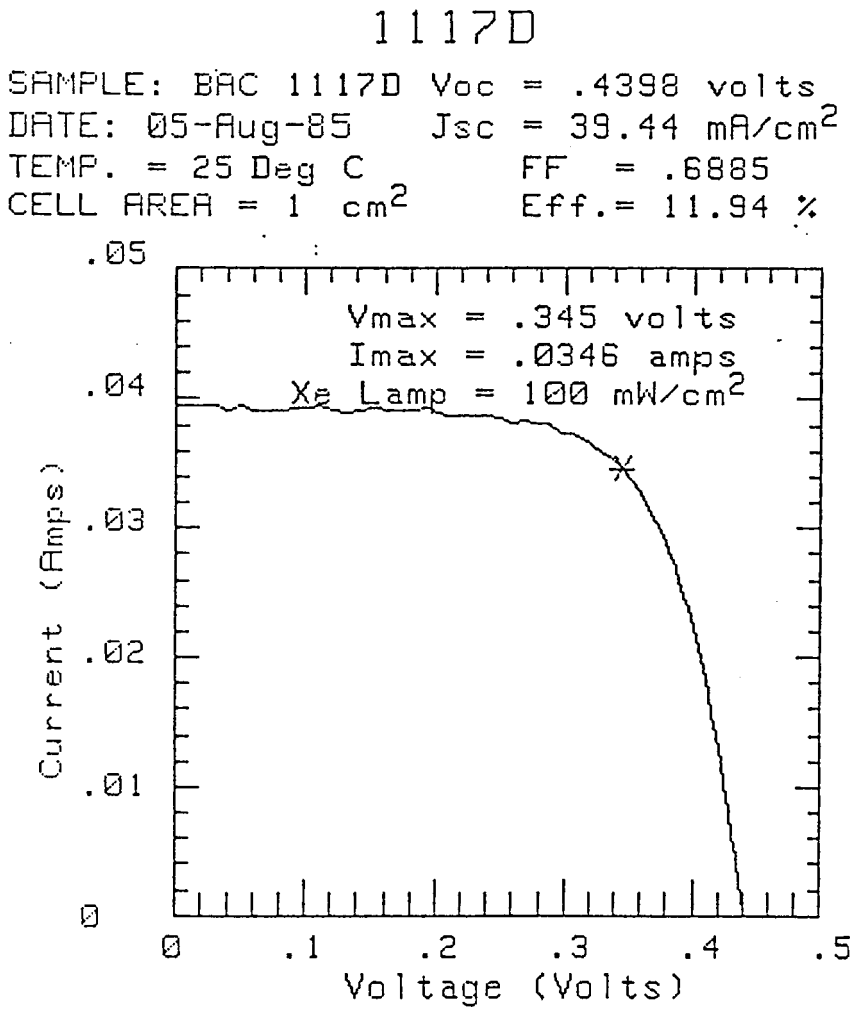

Figure 3.6-6 I-V Characteristic For Cell 1117D After AR Coating. Xenon Arc Solar Simulator was used.

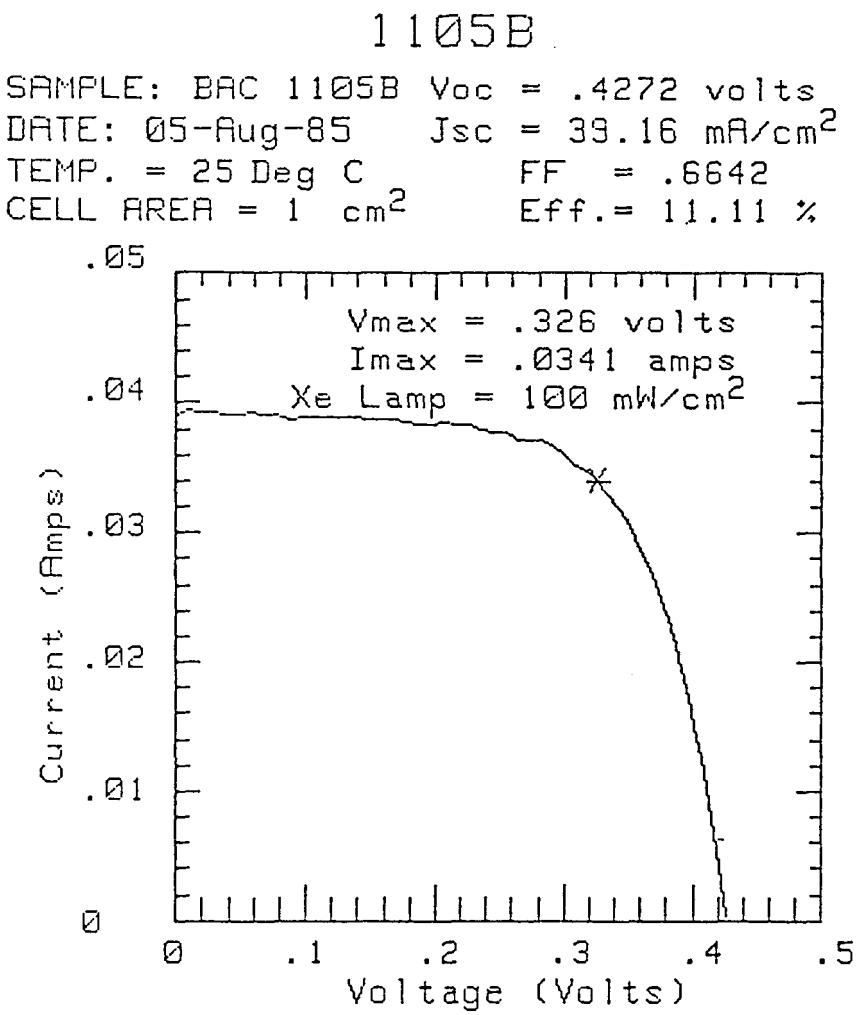

AVERAGE SHUNT Rsh= 49046.6 Ohm

Figure 3.6-7 I-V Characteristic For Cell 1105B After AR Coating. Xenon Arc Solar Simulator was used.

TEST
7/24/1985 11:48:53
BAC SAMPLE: 1105C
TEMPERATURE: 25.0 Deg C
UNIT CELL Area 1.000 cm^2
Total CELL Area 1.000 cm^2
No. cell in series = 1.00
No. of cell in parallel = 1.00
Base type is P type
REMARK: AFTER MIT AR

CURVE#	INTENSITY (mW/cm^2)	EFFICIENCY (%)	VOC (Volt)	ISC (Amp)	VMAX (Volt)	IMAX (Amp)	FILL FACTOR
1	100.00	11.33	.4330	3.8695E-02	.333	3.402E-02	.6762

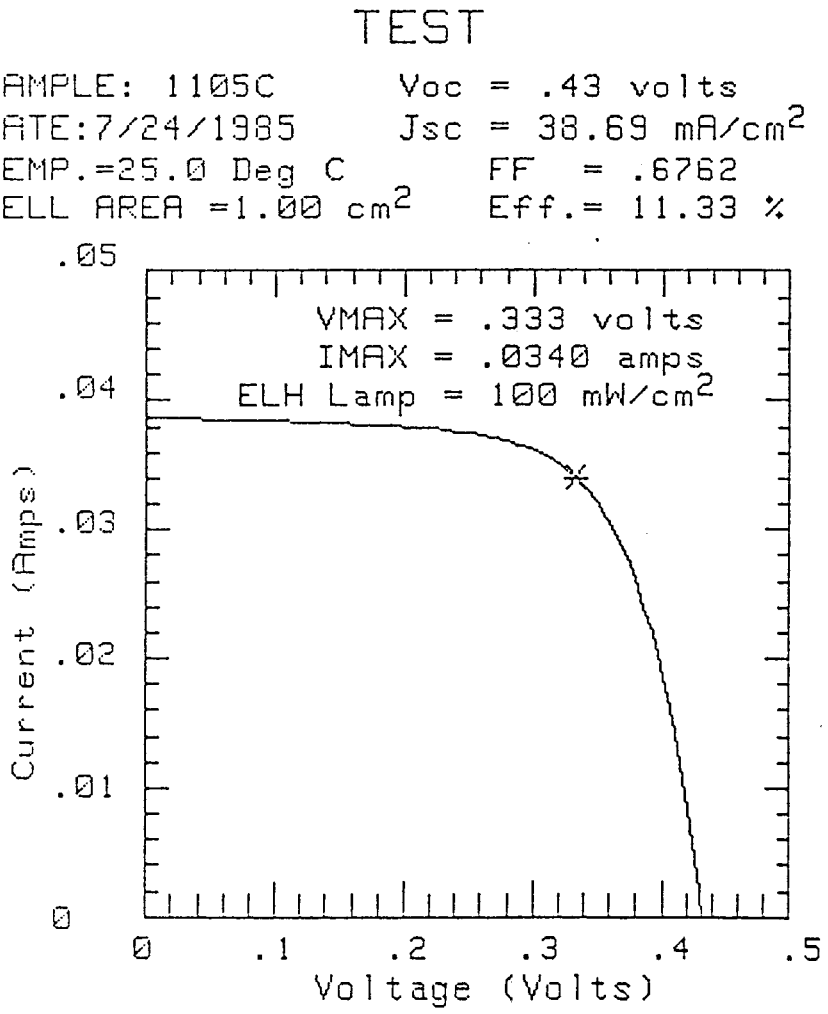

Figure 3.6-8 I-V Characteristic For Cell 1105C After AR Coating. ELH Illumination was used.

Table 3.6-7 I-V Parameters Before and After AR Coating. Xenon Arc Solar Simulator used at 100 mW/cm^2 equivalent, AM1 Spectrum.

Cell #	Eff [%]	Voc [volts]	Isc [mA]	FF	Isc Increase
1119D					
Before AR	8.90	.403	35.8	.616	
After AR	10.33	.416	40.8	.608	14.0%
1105C					
Before AR	9.80	.425	34.6	.672	
After AR	11.40	.432	39.3	.672	13.6%
1117B					
Before AR	10.03	.429	34.3	.682	
After AR	11.74	.435	39.7	.680	15.7%
1105B					
Before AR	9.33	.417	34.1	.656	
After AR	11.11	.427	39.2	.664	15.0%
1105D					
Before AR	9.42	.417	34.3	.659	
After AR	10.73	.421	39.1	.652	14.0%
1117D					
Before AR	10.24	.436	34.1	.687	
After AR	11.94	.440	39.4	.689	15.4%

Table 3.6-8 Comparison of I-V and Diode Parameters for Cells 1117B, 1117D and 857A.

Cell #	1117B	1117D	857A
Before AR Coating			
Efficiency [%]	10.0	10.2	10.0
Voc [volts]	.429	.436	.439
Isc [mA]	34.3	34.2	34.7
Fill Factor	.682	.687	.656
After AR Coating			
Efficiency [%]	11.7	11.9	11.0
Voc [volts]	.435	.440	.437
Isc [mA]	39.7	39.4	38.5
Fill Factor	.680	.689	.653
Ideal Diode Parameters (Taken After AR Coating)			
I_0 in Light [Amps]	2.5E-8	4.5E-8	3.2E-8
A Factor in Light	1.21	1.26	1.22
R_{shunt} in Light [KOHM]	89.4	8.78	0.600
R_{series} in Light [OHM]	0.5	0.5	1.2
I_0 in Dark [Amps]	8.8E-8	9.5E-8	?
A Factor in Dark	1.39	1.39	?
Isc Increase with AR	15.7%	15.4%	11.0%

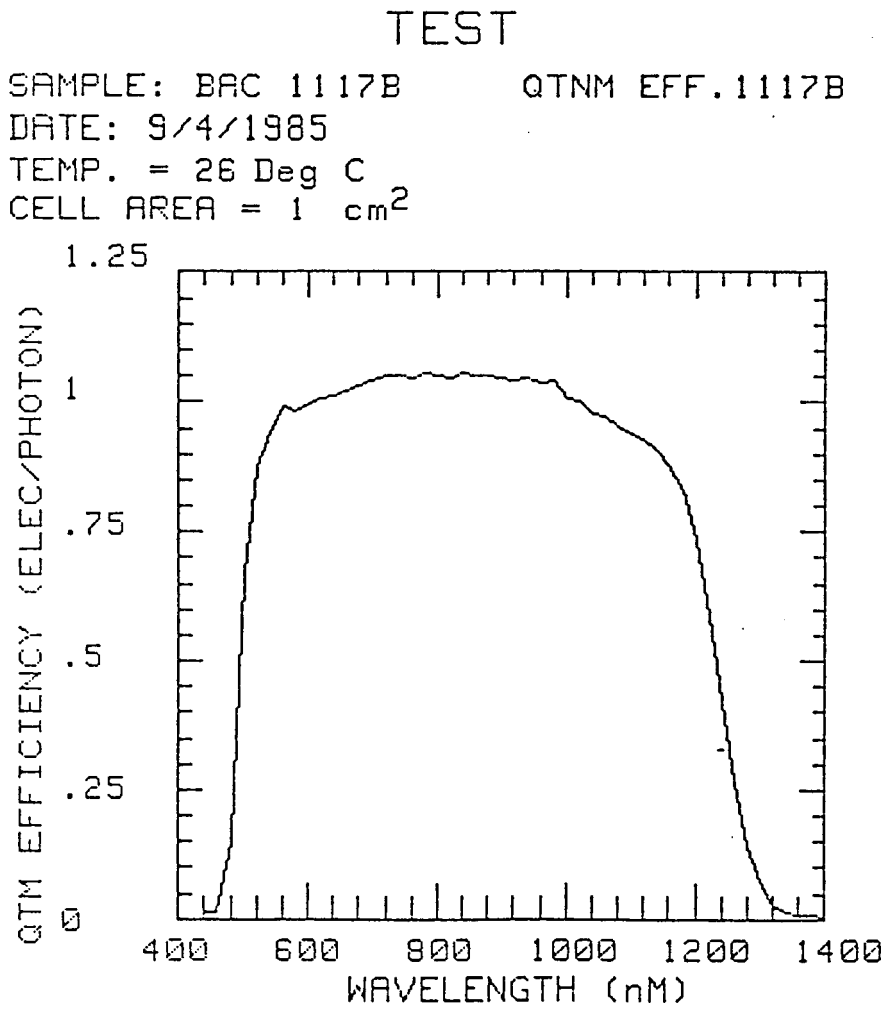

Figure 3.6-9 Spectral Response Curve For Cell 1117B After AR Coating.

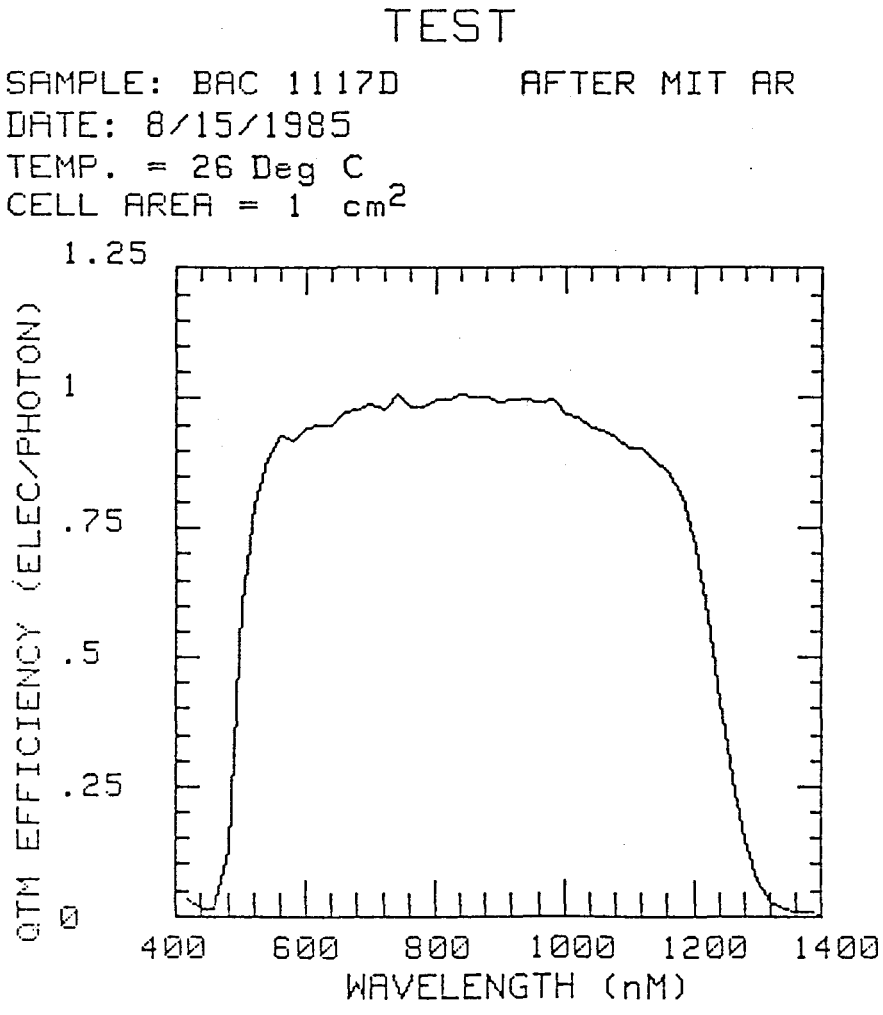

Figure 3.6-10 Spectral Response Curve For Cell 1117D After AR Coating

TEST
9/4/1985 10:29:09
BAC SAMPLE: 1117B
TEMPERATURE: 25.0 Deg C
UNIT CELL Area 1.000 cm^2
Total CELL Area 1.000 cm^2
No. cell in series = 1.00
No. of cell in parallel = 1.00
Base type is P type
REMARK: 30 MIN SOAK

CURVE#	INTENSITY (mW/cm^2)	EFFICIENCY (%)	VOC (Volt)	ISC (Amp)	VMAX (Volt)	IMAX (Amp)	FILL FACTOR
1	100.00	11.84	.4443	3.8664E-02	.349	3.390E-02	.6892
2	50.00		.4248	2.0705E-02	.336	1.827E-02	.6985
3	25.00		.4124	1.3547E-02	.331	1.180E-02	.6990
4	10.00		.3790	4.7701E-03	.304	4.081E-03	.6870

A_FAC= 1.2131 Io= 2.4732E-08 Amp SIGMA=1.298E-02

INTENSITY1 (mW/cm^2)	INTENSITY2 (mW/cm^2)	DELTA_I (Amp)	Rs (Ohm)
100.00	50.00	8.282E-03	.752
100.00	50.00	1.242E-02	.683
100.00	50.00	1.656E-02	.641
100.00	50.00	2.071E-02	.611
100.00	25.00	5.419E-03	.857
100.00	25.00	8.128E-03	.783
100.00	25.00	1.084E-02	.734
100.00	25.00	1.355E-02	.702
100.00	10.00	1.908E-03	1.230
100.00	10.00	2.862E-03	1.036
100.00	10.00	3.816E-03	.948
100.00	10.00	4.770E-03	.877

AVERAGE SHUNT Rsh= 89392.6 Ohm

Figure 3.6-11 I-V versus Intensity Data For Cell 1117B.

TEST
8/15/1985 10:35:13
BAC SAMPLE: 1117D
TEMPERATURE: 25.0 Deg C
UNIT CELL Area 1.000 cm^2
Total CELL Area 1.000 cm^2
No. cell in series = 1.00
No. of cell in parallel = 1.00
Base type is P type
REMARK: AFTER MIT AR

CURVE#	INTENSITY (mW/cm^2)	EFFICIENCY (%)	VOC (Volt)	ISC (Amp)	VMAX (Volt)	IMAX (Amp)	FILL FACTOR
1	100.00	11.89	.4437	3.9034E-02	.347	3.423E-02	.6863
2	50.00		.4231	2.0786E-02	.337	1.807E-02	.6929
3	25.00		.4094	1.3523E-02	.323	1.189E-02	.6937
4	10.00		.3746	4.6460E-03	.299	3.960E-03	.6793

A_FAC= 1.2630 Io= 4.4891E-08 Amp SIGMA=3.629E-03

INTENSITY1 (mW/cm^2)	INTENSITY2 (mW/cm^2)	DELTA_I (Amp)	Rs (Ohm)
100.00	50.00	8.315E-03	.690
100.00	50.00	1.247E-02	.630
100.00	50.00	1.663E-02	.597
100.00	50.00	2.079E-02	.566
100.00	25.00	5.409E-03	.794
100.00	25.00	8.114E-03	.704
100.00	25.00	1.082E-02	.661
100.00	25.00	1.352E-02	.630
100.00	10.00	1.858E-03	1.190
100.00	10.00	2.788E-03	1.000
100.00	10.00	3.717E-03	.900
100.00	10.00	4.646E-03	.843

AVERAGE SHUNT Rsh= 8782.7 Ohm

Figure 3.6-12 I-V versus Intensity Data For Cell 1117D.

Figs. 3.6-5 to 3.6-8 show I-V characteristics before and after the antireflection coating for two of the best cells. Table 3.6-7 summarizes the data for all of the six cells coated. It is clear that the effect of the AR has been just as expected. The highest current increases seen are consistent with decreases in reflection losses from the 17% of the bare CdZnS to 3-4% for the coated cells. These numbers are subject to error from several sources but the error in the integrated CdZnS reflectance cannot be greater than 1-2%. The lower current increases seen on some of the samples are caused by a combination of non-optimized layer thicknesses and SiO_x stoichiometry too close to x=1. Only small changes in Voc and curve fill factor are seen in most cases, as expected. We conclude therefore that reflection suppression was the only effect of the AR and that the magnitude of the effect is consistent with the simple optical model presented in this report.

Several of the cell efficiencies shown in Table 3.6-7 are greater than the previous best published values for $CuInSe_2$/CdZnS polycrystalline thin-film solar cells. Table 3.6-8 shows a detailed comparison of the two best new cells with the previous best $CuInSe_2$/CdZnS cell reported. Comparison of I-V characteristics before AR coating shows that the efficiency increase is due partially to the improved reflection suppression and partially to better fill factors. The small apparent decrease in current density before AR is believed to be an artifact due to changed simulator calibration. Spectral response and I-V versus intensity data were taken for several of the AR coated cell and are presented in Figs. 3.6-9 to 3.6-12. These data have been summarized and are discussed further in a paper prepared for and presented at the Eighteenth IEEE Photovoltaic Specialist Conference (16).

The spectral response curves for these new high efficiency cells show quantum yields (electron/photon) flat over most of the active band of the cells. In fact using the present calibration of the reference detectors in our system against a pyroelectric radiometer quantum yields slightly above 1.0 are indicated. These readings are however within the calibration error bars of the system for absolute measurement, which we estimate at +/-5%.

One possible source of error in both the efficiency and quantum yield measurements is the cell area used. Since the cell is formed by etching the sulfide film to define the cell area of 1 cm^2. This etch process leaves a rough edge and makes an exact measurement of the average dimensions difficult. In addition, at low intensities or in reverse

bias edge regions may contribute which do not when the cell is loaded at the peak power point. Such edge effects could therefore result in decreased fill factors at 100 mW/cm^2.

In order to evaluate any edge effects which might be present the two highest efficiency cells were measured using a totally different efficiency measurement technique from the normal. Instead of allowing the total radiation incident on the cell to be defined by the cell area, an aperture mask in the testing plane was used to define the total radiation incident. The incident radiation used for efficiency calculations then becomes the total radiation passing through the mask, with no corrections permitted for subsequent losses. To accurately reflect the characteristics of the cell under test requires the aperture must be close to the cell area in size, in close proximity to the cell under test, and of course completely opaque.

In our case a metallized polyester film with a 0.97 cm^2 square opening cut into it was used in direct contact with the cell. Electrical connections to the top pad were made through holes in the mask significantly smaller than the metallized pad itself.

Table 3.6-9 summarizes the results for the two cells. Both the decreased current density and increased fill factors are seen for the masked curves. The results are subject to some error because the mask and contact alignment are difficult and must be done under the solar simulator using a microscope. However the likely sources of error in this technique are all such as to decrease the resulting current density and efficiency. The indicated differences between masked and unmasked curves therefore should be considered as upper limits on the magnitude of the edge effect for the two devices.

Based on these results we find upper limits on the collection area at short circuit of 1.05 cm^2 for 1117B and 1.06 cm^2 for 1117D.

During this quarter several experiments were done in which the compositional grading of the $CuInSe_2$ was varied from the two layer structure normally used for the high efficiency cells. The major purpose of the work was to better control the properties of the selenide at the molybdenum/selenide interface and reduce or eliminate the suspected contact problems there. It was found that cells made with, for example, enhanced copper content in the selenide near the Mo contact frequently showed device characteristics equal to or better than normally prepared controls. However, it became

Table 3.6-9 Comparison of Masked and Unmasked I-V Measurements of Cells 1117B and 1117D.

	Eff (%)	Voc [volts]	Isc [mA]	FF	Jsc [mA/cm^2]	Jsc active area [mA/cm^2]
Cell 1117B						
Unmasked	11.79	.442	39.7	.692	39.7	41.6
Masked	11.46	.442	36.2	.694	37.4	39.2
Cell 1117D						
Unmasked	12.05	.441	39.4	.685	39.4	41.3
Masked	11.39	.441	36.3	.690	37.5	39.3

Notes:

1) Simulator Calibration approximately 100 mW/cm^2, Xenon Tester used.
2) Areas Assumed:

	Total	Active
Masked	0.970 cm^2	0.924 cm^2
Unmasked	1.00 cm^2	0.954 cm^2

3) Cells soaked under light at open circuit for approximately 30 minutes.

clear that the differences between these samples were primarily a function of the overall or averaged composition of the film. Adjustment of the copper profile, the primary variable used, inevitably resulted in changes in the average selenide composition. It was concluded therefore that it was not possible to sort out the effect of contact modifications from the effects of composition and bulk composition gradient variations in these experiments.

Some information has been presented previously on the changes in I-V characteristics resulting from overall selenide composition changes (8). The correlations of carrier type, resistivity, and material morphology with composition for these thin film $CuInSe_2$ cells are all well known. In order to sort out the effect of compositional profile variation from that of simple overall composition change it was decided to look at controlled composition changes using the normal two layer structure.

An extensive study of the oxygen effect on the $CuInSe_2$ has been made by R. J. Matson et al. at SERI (26) but again the effect of compositional variation was not explored.

A second series of substrates were made to determine the effect on both I-V and spectral response of a deliberate but small variation in $CuInSe_2$ composition around that composition presently considered optimum. An additional complication which must be introduced in the study is the effect of the post deposition heat treatments. These are done at 225°C in oxygen, usually for 5-10 minutes. The effect of this heat treatment on I-V parameters was discussed above but the spectral response data reported does not include the effect of composition.

Table 3.6-10 summarizes the characteristics of the four substrates used for the comparison. No cells were fabricated on substrate 1140 since the n-CdZnS on n-$CuInSe_2$ has frequently in the past been shown to give no useful photovoltaic devices. Morphology and hot probe results followed composition as expected from the EDX results in the table. CdZnS was used as the n-layer of the heterojunction and the window layer as usual. The characteristics are given in Table 3.6-10.

Table 3.6-10: Data Summary for Substrates 1140,1141, 1142,1143.

Preparation Dates

	Selenide	Sulfide
1140	11/27/85	none
1141	12/02/85	12/09/85
1143	12/04/85	12/09/85
1142	12/03/85	12/09/85

Selenide Composition Data
(using old calibration standard. See third quarter report.)
In atomic %

	Cu	In	Se
1140	20.8	29.3	49.9
1141	23.9	27.1	49.0
1143	24.3	26.2	49.5
1142	25.5	25.8	48.8

Hot Probe Results
all readings in nA.

	as made		after cell fab	
1140	100	"N"	n.a.	
1141	50-100	"P"	20-30	"P"
1143	80	"P"	80-120	"P"
1142	600-1500	"P"	300-1000	"P"

Selenide Thickness:
1140 3.5 microns
1141 3.3-3.6 microns
1143 3.6 microns
1142 3.5 microns
Standard two layer 1/3-2/3 structure

Sulfide Composition (for 1141,1142,1143)
Zn Content: approximately 0.15 (z in $Zn_zCd_{1-z}S$).
Thickness: 2.8-3.0 microns
two layer - first 0.4 micron undoped
remaining In doped
Sheet Resistance: 10-30 ohms/square

Table 3.6-11 summarizes the I-V data before and after heat treatment for this set of cells. The fill factors shown in the table are low for several reasons; however the major effect for the near optimum substrate was the overly long heat treatment time used (15 minutes). This is shown by the comparison with a similar cell in Table 3-2 which was given only 5 minutes heat treatment. The cells showed some current loss and change in the spectral response curve after 5 minutes, however 15 minutes was used for the spectral response comparison to increase the differences measured.

Table 3.6-11: I-V Data For Cells in Spectral Response Experiment.

Heat Treatment was 15 min at 225°C in flowing Oxygen

	Voc	Isc	Vmax	Imax	ff	Eff
Cell 1141D (Cu poor)						
before HT	.375	34.9	.266	27.8	.563	7.38
after HT	.408	32.8	.298	27.4	.611	8.16
Cell 1142D (Cu rich)						
before HT	.262	33.8	.176	23.5	.466	4.13
after HT	.285	33.4	.184	25.5	.494	4.70
Cell 1143D (Cu near optimum)						
before HT	.387	36.0	.282	28.2	.572	7.95
after HT	.429	34.1	.297	28.1	.572	8.37
Cell 1143C after 5 min 225°C HT in flowing Oxygen						
	.420	34.7			.636	9.28

Note: Optimum HT was approximately 5 min. Excessive heat treatment caused fill factors to drop.

Table 3.6-11 I-V Data For Cells in Spectral Response Experiment.

Heat Treatment was 15 min at 225C in flowing Oxygen

	Voc	Isc	Vmax	Imax	ff	Eff
Cell 1141D (Cu poor)						
before HT	.375	34.9	.266	27.8	.563	7.38
after HT	.408	32.8	.298	27.4	.611	8.16
Cell 1142D (Cu rich)						
before HT	.262	33.8	.176	23.5	.466	4.13
after HT	.285	33.4	.184	25.5	.494	4.70
Cell 1143D (Cu near optimum)						
before HT	.387	36.0	.282	28.2	.572	7.95
after HT	.429	34.1	.297	28.1	.572	8.37
Cell 1143C after 5 min 225C HT in flowing Oxygen						
	.420	34.7			.636	9.28

Note: Optimum HT was approximately 5 min. Excessive HT caused fill factor to drop.

Figs. 3.6-13 to 3.6-15 show the spectral response before and after HT for each of the three cells measured. Curves were taken at short circuit loading and the data is uncorrected for reflection or other losses. The primary effect of the HT is a loss in the long wavelength response for the two cells deficient in Cu. The corresponding loss in current is seen in the I-V data of Table 3.6-11 for these two cells.

Both the voltage increase and current decrease upon heat treatment are as have been previously reported. However for these recent cells the current loss after just 5 minutes was much less that seen earlier (5). The spectral response data shows no evidence supporting a deeply buried homojunction model for the $CuInSe_2$/CdZnS device. The spectral response data before HT shows no sign of collection loss at short wavelengths as would be expected for a junction buried deep in the selenide. The data does not however preclude such a model. The variation of the HT effect with composition is consistent with a compensation model, since the more intrinsic material should be more sensitive to diffusion of a compensating dopant.

One complication for this simple view is shown in Fig. 3.6-16, where the after HT curves for all three cells are superimposed. A systematic variation in the slope at the $CuInSe_2$ absorption edge is seen. This is explainable using just variation in minority carrier collection depth. However the variation in edge position seen in the experimental data implies a more complicated mechanism is also present. One possibility is the variation in optical absorption with composition of the $CuInSe_2$ as suggested by R. Noufi of SERI. At present this thesis remains untested and the true cause is unclear.

Further proposed work will concentrate on using the spectral response results from this and additional experiments to attempt an understanding of the depth dependence of the current loss mechanism.

3.7 Ion-Assisted Film Deposition

The inclusion of ions into thin-film deposition processes has become increasingly attractive. The ions, formed by ionization of the depositing atoms or by an ion gun which simply irradiates the depositing film (ion-assisted deposition) can significantly alter the film properties. The effects have ranged from enhanced substrate adhesion resulting from ion cleaning processes to structural and

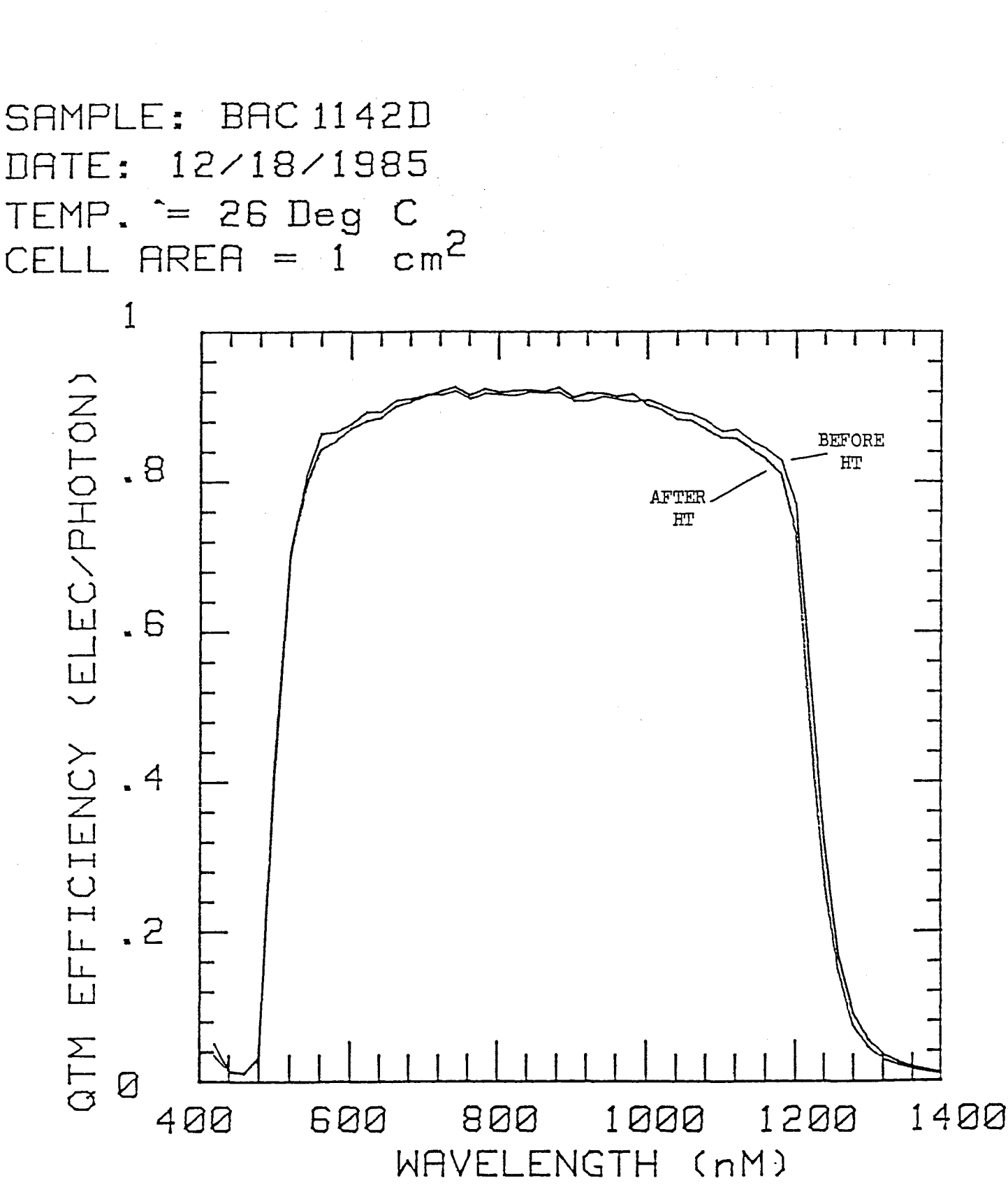

Figure 3.6-13 Spectral Response of Cu Rich Selenide Cell Before and After 15 minute, 225°C Heat Treatment in Oxygen.

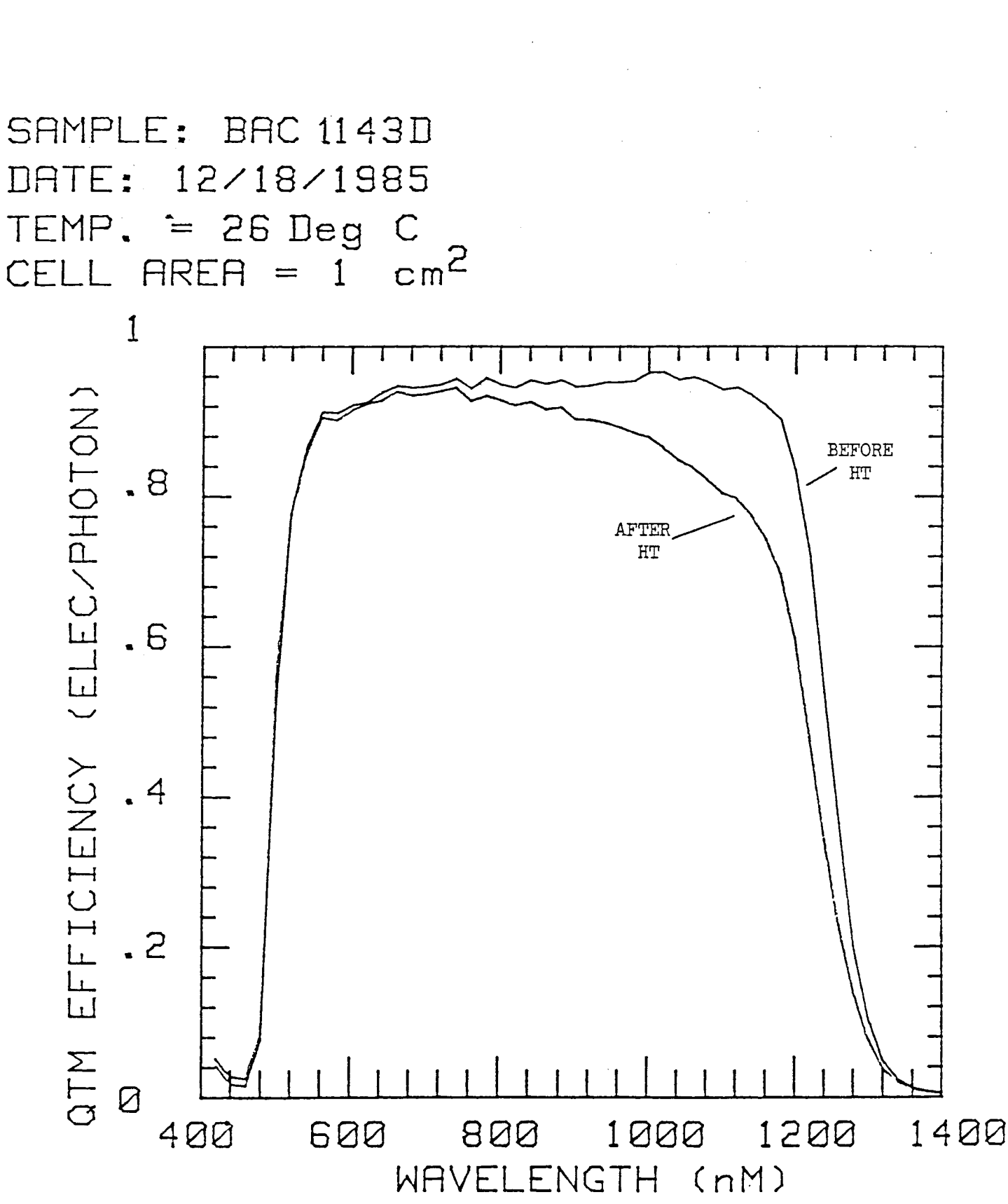

Figure 3.6-14 Spectral Response of Selenide Cell with Near-Optimum Copper Content, Before and After 15 Minute Heat Treatment.

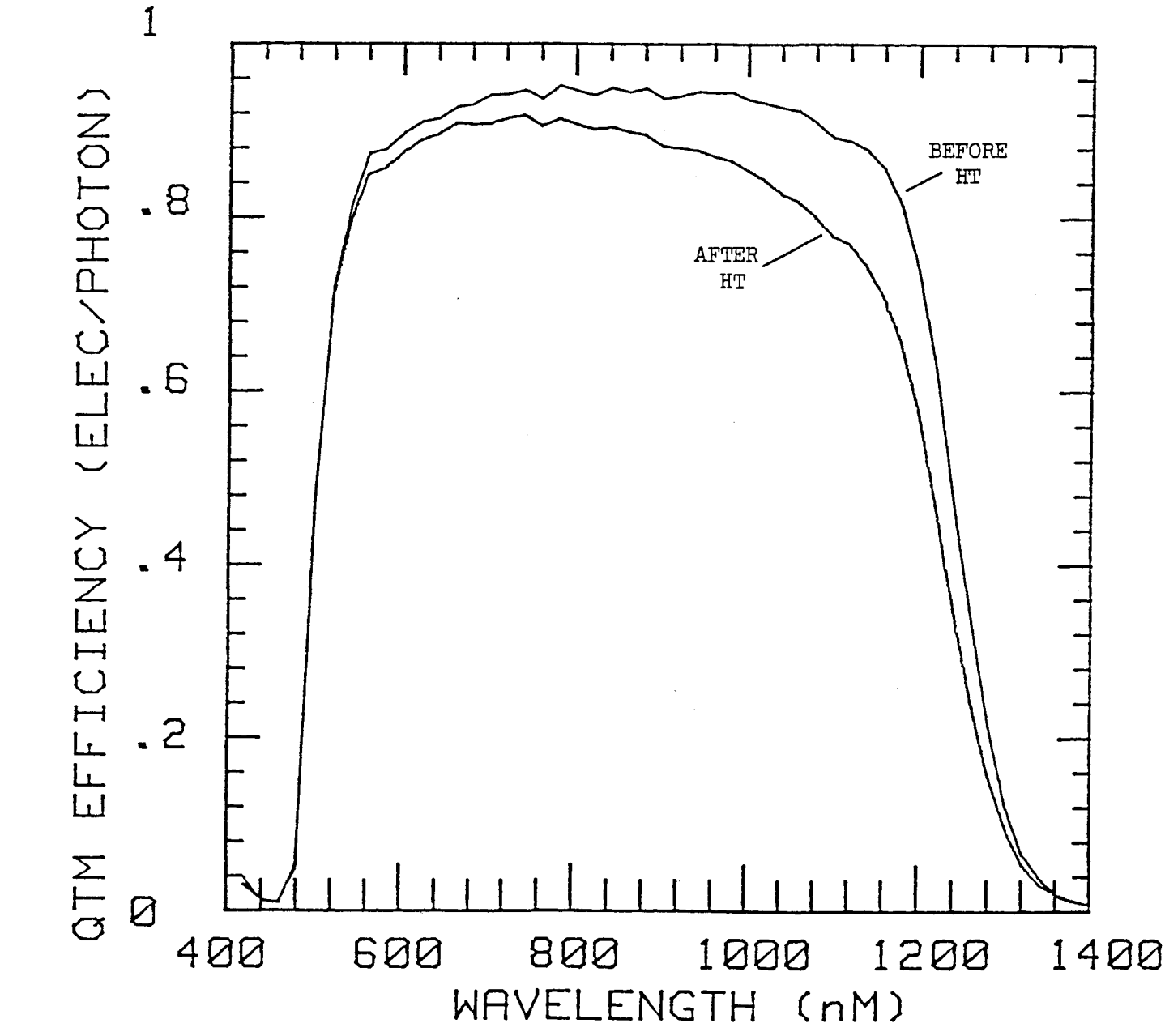

Figure 3.6-15 Spectral Response of Cu Poor Selenide Cell Before and After 15 Minute, ~225°C Heat Treatment in Oxygen.

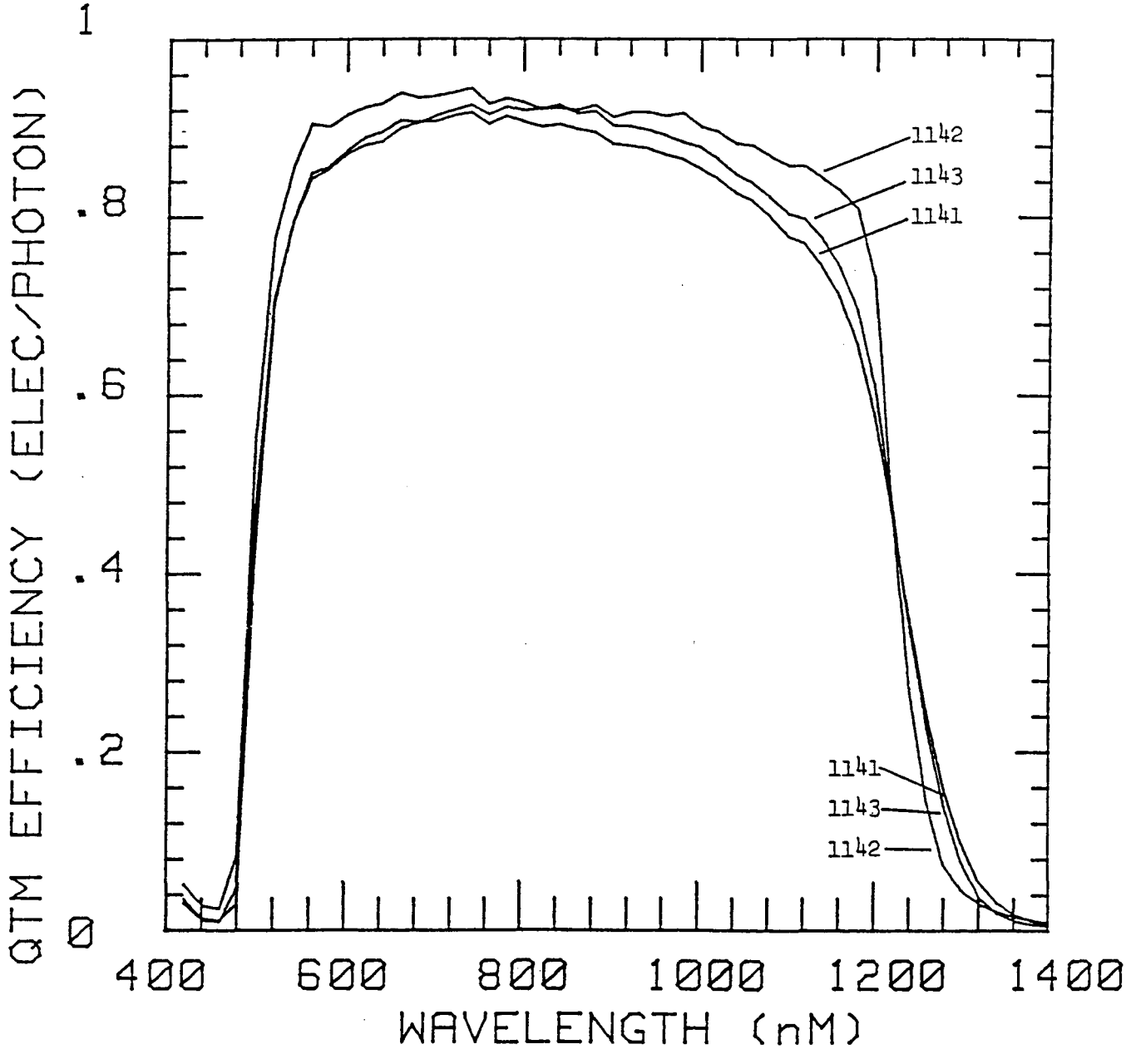

Figure 3.6-16 Comparison of Spectral Response Curves After Heat Treatment for Three Selenide Substrates With Different Compositions.

compositional variations. As would be expected, these variations have shown a strong influence on the optical and electrical properties of polycrystalline dielectric and semiconductor thin-films. It was the intent of this program task to determine whether the use of ions during the selenide and/or sulfide film depositions could be beneficial to the final cell characteristics.

The easily implemented technique of ion-assisted deposition was selected to research this technical area using an Ion-Tech Ion Beam Source equipped with divergent grids. The gun had a 2.5cm beam diameter at the exit of the source and operated at beam energies between 150 and 1500eV. The gun was installed first in the sulfide and later in the selenide film deposition chambers. Only argon was used as the ionization gas since this was believed sufficient to indicate the possibility of cell improvement by ion-assisted deposition. Thus, both CIS and CdS films were deposited while the film surface was being irradiated with argon ions. In addition, the ions were used to sputter clean and sputter etch the selenide film surface immediately prior to the sulfide deposition as well as the sulfide surface prior to aluminum film grid deposition. The sputter etching experiments were, however, very limited as they tended to increase the incidence of cells with shunting defects (selenide etching) and were not noticeable better than the standard RF sputter etch technique (sulfide etching).

The ion beam gun was mounted in the sulfide deposition chamber such that it was shielded from the thermal vapor sources and there was approximately a 13-inch spacing between the gun exit aperture and the center of the substrate holder. The ion beam impinged at an angle of about 45° from the substrate normal.

It was found experimentally that the gun voltage/current parameters measured at Ion Tech could be duplicated if the argon pressure indicated by the vacuum system digital ionization gauge was adjusted to $4.8\text{-}5.2 \times 10^{-5}$ torr. Consequently, all work with the gun was conducted at this gas pressure value and used the beam neutralization feature (immersed wire). By operating the gun under conditions of high acceleration voltages (450-500V), it was possible to sufficiently spread out the ion beam to cover a 4x4-inch substrate area with reasonable uniformity.

Proceeding the ion-assisted sulfide depositions, the technique was applied to indium oxide films. One near term approach for cell improvement concerned the use of a very thin sulfide film (~0.5 micrometers) covered with a

transparent but highly conductive film (< 50 ohm/square). The obvious choice for the transparent conducting film was ITO and, as described elsewhere in this report, a sputtering process was established to prepare ITO films with the required properties for this cell application. A strong disadvantage of ITO has been its electrical instability when exposed to temperature/time conditions such as those used in cell heat treatment. As an alternative, another film preparation program was run in parallel to the ITO development. The second study involved indium oxide films prepared by vacuum evaporation. The films were prepared by evaporating indium or indium oxide source materials at very low deposition rates in an oxygen environment.

It was determined that films of ~0.25 micrometers thickness could be formed at substrate temperatures below 175°C with sheet resistivities of less than 50 ohm/square, but the transparency was poor (<50%). While the low transparency was attributed to insufficient oxidation, the deposition conditions had been adjusted as far as possible to enhance oxidation, eg., 0.1nm/sec deposition rate and $3x10^{-4}$ torr oxygen partial pressure. Continuation of the indium oxide film preparation studies was, however, motivated by the fact that the films appeared stable under the cell heat treatment conditions. Early results from ion-assisted film deposition studies on indium oxide suggested the necessary improvements in optical transparency could be realized using this technique.

To reduce sputtering and ion damage, the ion-assisted depositions were carried out with a 600 to 200V beam of argon ions. The beam currents ranged from 5 to 20mA and the oxygen pressure from 1 to $2x10^{-4}$ torr. Again, very low deposition rates(0.1nm/sec) and substrate temperatures of 150-175°C were used. Optical transmission data from two ion-assisted film depositions and one deposition made without ions are shown in Figure 3.7-1. As can be seen, the transmittance of the two ion-assisted films was in the vicinity of 80-90% while the non I-A film was less than 30%. Thicknesses for all three films were approximately 280-290nm but the resistivities of the I-A deposits were much lower, ie., 40 ohm/square vs. 200 ohm/square. The low resistivities of the I-A films were, moreover, found to be unchanged by heating for 30 minutes at 225°C in an oxygen environment.

Unfortunately, the attractive optical and electrical properties of the I-A indium oxide films were not retained when the films were deposited over a CdS layer. The films again exhibited poor transparencies and high resistivities. In terms of improved cell performances, subsequent results

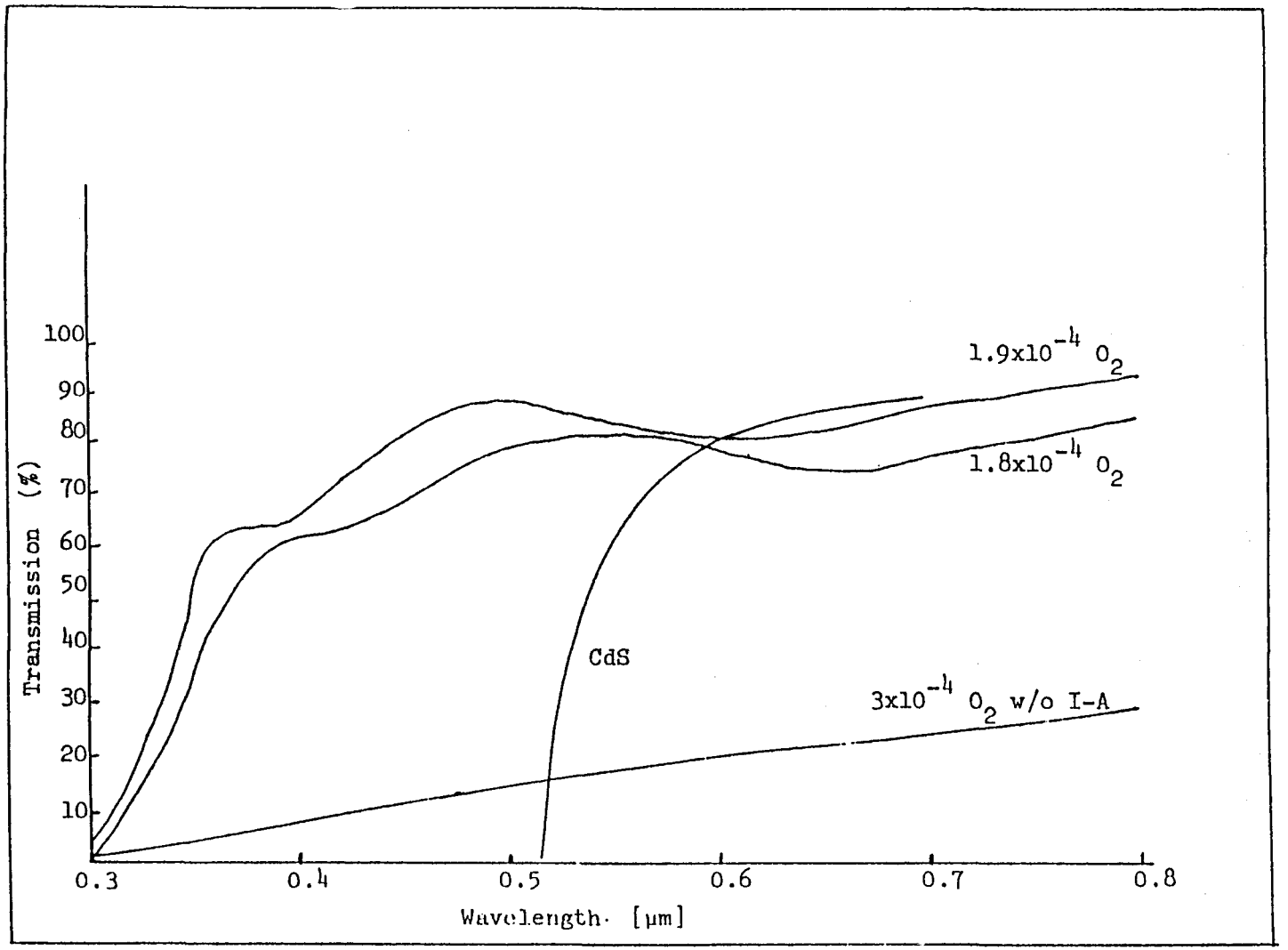

Figure 3.7-1 Optical Transmission of Ion-Assisted Deposited Indium Oxide Films.

with I-A sulfide and CIS films were also not apparent. Cell shunting was a recurrent problem and may suggest that these thin-film devices cannot withstand bombardment with highly energetic ions.

3.8 ITO Alternate Window Material

Reactive sputtered ITO has been investigated as a conductive window layer to establish whether a high efficiency device can be fabricated by using a thin (>50 nm) CdS layer to form a junction along with a ITO layer to act as a non-absorbing conducting layer. By using a thin sulfide layer in conjunction with a high bandgap conducting layer, the response of the device should be extended into lower wavelengths. Thus the device should produce a higher current and efficiency than a typical CIS/CdZnS:In solar cell.

ITO coatings with transparencies of 85% and resistivities of less than $5x10^{-4}$ ohm*cm have been deposited by DC magnetron sputtering in an atmosphere of Ar/O_2. During deposition, residual gas analyses were performed to calculate the percentage of oxygen consumed over a range of O_2 injection rates at three separate sputtering currents. Figure 3.8-1 shows the fraction of oxygen consumed during sputtering as a function of the oxygen injection rate. For each current level to the source, the fraction of oxygen consumed shows a maximum. At the maximum fraction consumption level, the coating has been found to posses the desired combination of low resistivity and high transparency. The resistivities indicated on the 300 milliamperes curve in figure 3.8-1 show that the minimum resistivity occurs at the oxygen fraction consumption peak. Also note that for low oxygen injection rates (less than 0.6 mtorr-liters/sec.), the coatings were optically opaque. At higher injection rates, the coatings possessed the desired transparency. Spectrophotometric analyses of a typical sample with a sheet resistance of $5x10^{-4}$ ohm-cm are shown in figure 3.8-2. Absorptance is seen for wavelengths of 1000 nm and higher with a shape characteristic of free carrier absorption.

Spectral response measurements of a solar device with a window layer of thin (50 nm) CdZnS and ITO (160 nm) were compared to a baseline sample with a window layer of thick (300 nm) CdZnS:In. Figure 3.8-3 shows these spectral response data. The device with the ITO window layer shows a shift in the short wavelength region from 520 to about 480 nm. This shift was attributed to the use of the transparent ITO conducting layer instead of a degeneratively doped layer of

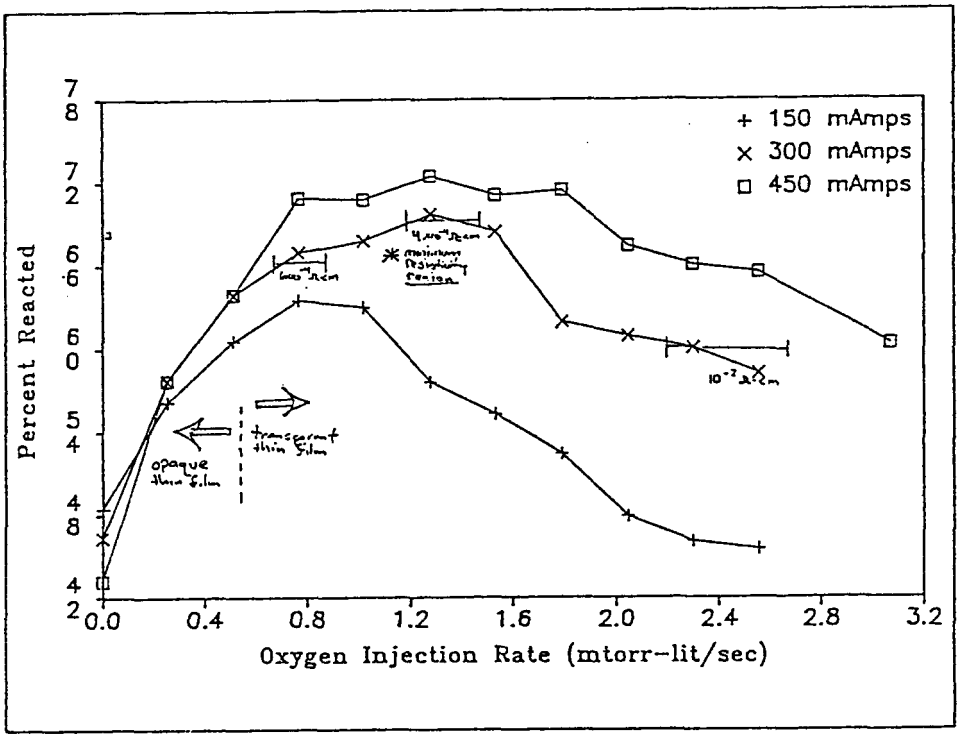

Figure 3.8-1 Oxygen Reaction Rate vs Injection Rate.

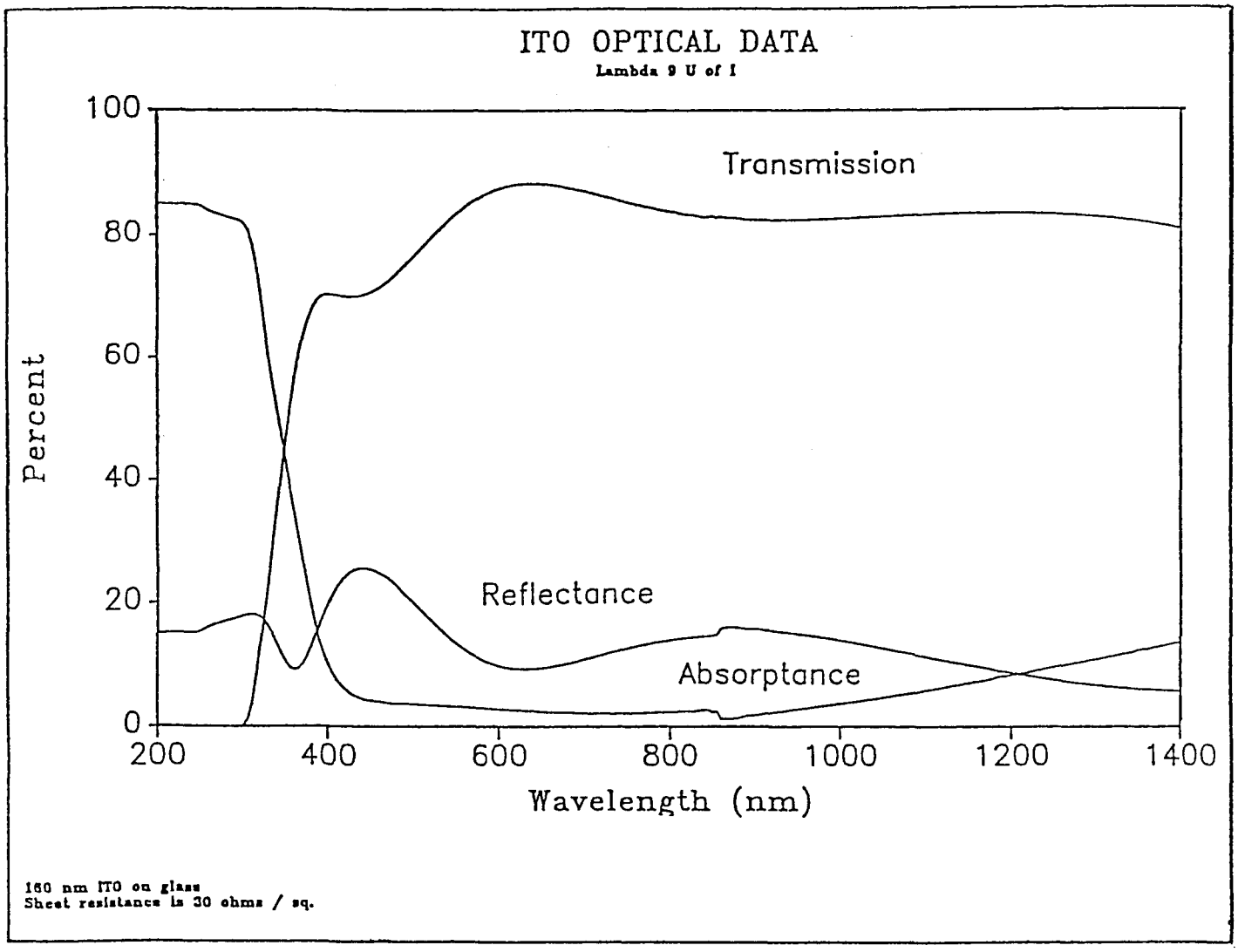

Figure 3.8-2 Photospectroscopy Analysis of Reactively Sputtered ITO on Glass. Analyses were conducted at the University of Illinois.

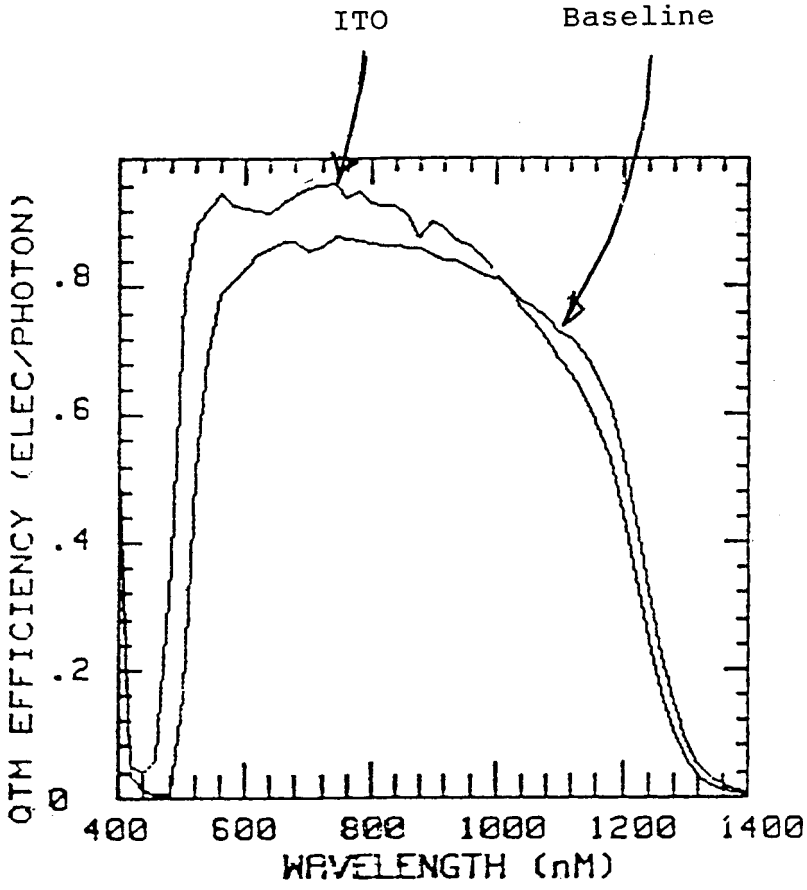

Figure 3.8-3 Quantum Efficiency Comparison of Baseline and ITO Coated CIS Solar Cell

CdZnS:In. The degenerate doping presumably shifts the sulfide bandgap by creating a high density of states near the conduction band. This was consistent with optical absorptance spectral data shown in figure 3.8-4. The doped sulfide was absorbing between 480 and 520 nm while the undoped sulfide was non absorbing. This difference in optical absorptance occurs at the same wavelengths as the noted difference in spectral response data. The spectral response and optical absorptance data clearly show that the use of a transparent conducting layer increases the collection bandwidth of the solar cell.

Devices fabricated with less than 50 nm of CdS (~ 10-30 nm) showed lower voltages and shunting due to leakage at areas of contact between the ITO and $CuInSe_2$.

The equipment used for the ITO studies was as follows: The deposition chamber consisted of three 40 x 40 x 10 cm cubicles which were connected end to end to form one long in-line system. Another 40 x 40 x 10 cm chamber served as a load lock. Figure 3.8-5 shows a schematic drawing of the vacuum system which illustrates the gas feed, pumping and substrate handling systems. By using the load lock, the substrate pallet could be loaded into the chamber without exceeding a pressure of 10^{-5} torr. Pumping was provided by a Leybold-Heraeus turbo-molecular pump with a nominal pumping speed of 450 liters/sec. The calculated pumping speed for the vacuum chamber for Argon and Oxygen was 150 and 160 liters/sec respectively. Substrates were placed face up onto a 30 cm^2 pallet which travels end to end through the vacuum chamber on rollers (See figure 3.8-5). The rollers rotate at a selected rpm which produces a pallet travel rate of typically 4 cm/min.

The sputtering target was a sintered oxide target composed of 98% Tin Oxide and 2% Indium Oxide. The target dimensions were 30 x 12 cm with a magnetron assembly which confines the sputtering plasma to an oval directly adjacent to the target. The power source was a high voltage DC supply. The target was mounted on the top of the chamber and sputtered in a downward direction. The heating assembly was mounted on the underside of the deposition chamber to heat the substrates from the backside and provide constant heating during deposition. Figure 3.8-6 shows a schematic drawing of the deposition station. During deposition, the pallet traveled between the target and heating assembly, thereby providing simultaneous deposition and heating. The in-line configuration allows uniform deposition over square parts that are 25 x 25 cm in dimension.

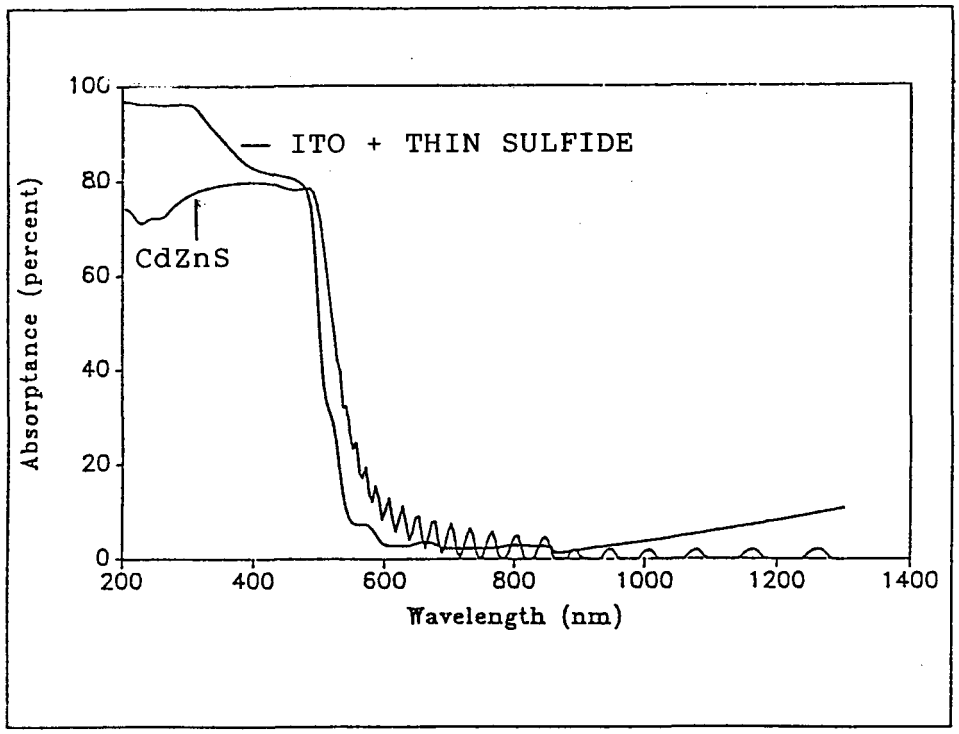

Figure 3.8-4 Absorptance of Window Layers

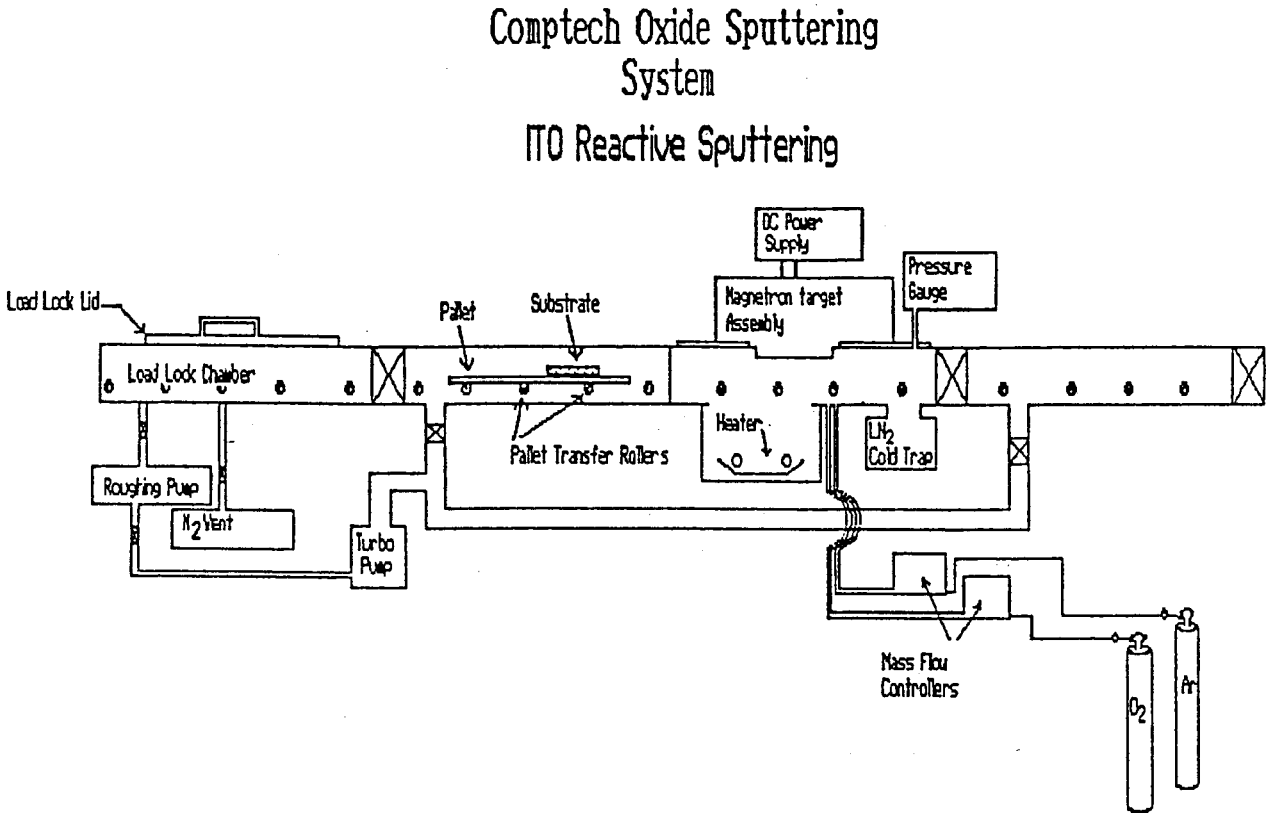

Figure 3.8-5 Schematic Drawing of the Vacuum Deposition System Used to Reactively Sputter ITO.

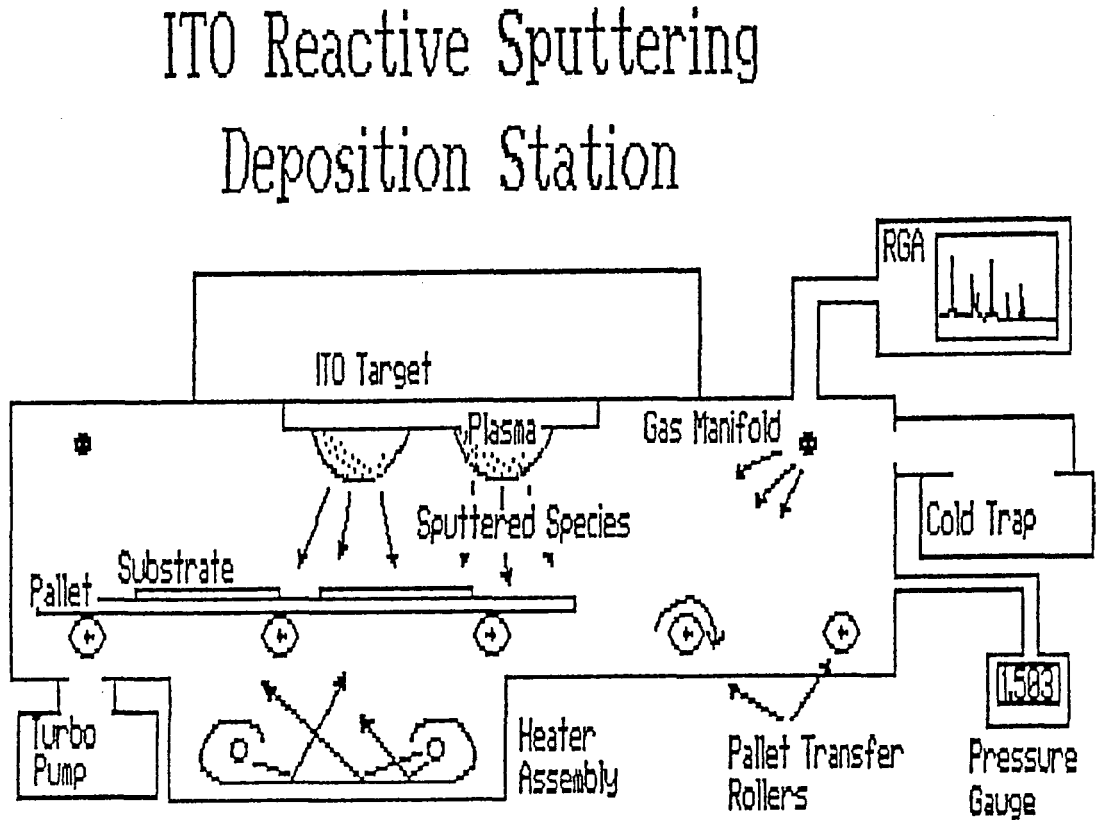

Figure 3.8-6 Schematic Drawing of the ITO Sputter Deposition Station

Argon and Oxygen were injected into the deposition chamber through a manifold and were controlled independently with MKS type mass flow controllers. During deposition, the pumping speed was decreased by pumping the chamber via a meter long, 15 cm diameter tube. The conductance losses in the tube reduced the Argon and Oxygen pumping speeds to 12.5 and 14 liters/sec respectively. A liquid nitrogen cold baffle was connected to the deposition chamber, which provided additional pumping to the system. Typical deposition parameters are listed in Table 3.8-1 below.

Table 3.8-1: ITO Deposition Parameters

Oxygen Injection Rate (torr-lit/sec)	1.4
Argon Injection Rate (torr-lit/sec)	21
Heating power (Watts)	500
Pallet Travel Speed (cm/min)	4.0
Pumping Speed (lit/sec)[Ar]	12.5
Pumping Speed (lit/sec)[O_2]	14.0
Magnetron Current (Amps)	0.3
Magnetron Voltage (Volts)	300
Deposition Rate (nm/min)	40
Target to Substrate Distance (cm)	4.0
Ar Partial Pressure (mtorr)	1.5
O_2 Partial Pressure (mtorr)	0.2
Background Pressure (torr)	10^{-6}
Ultimate pressure (torr)	2×10^{-7}

4.0 Conclusions and Proposed Plans for Further Work

The detailed conclusions have been included in the discussion of each major topic and are contained in the summary.

As a result of the work performed in this contract the following have been identified as the major areas for further development:

$CuInGaSe_2$ Materials and Device Development
- Higher Ga Fraction Content Films and Devices
- FF Loss Mechanism in High Ga Content Films
- Lower Substrate Temperature Processes

$CuInSe_2$ Materials and Device Development
- Extrinsic Doping Studies
- Composition Gradient Optimization
- Stoichiometric Film Preparation
- Methods for Improved Process Control

Activated Deposition Processes
- Alternate Se Source Development

ZnO and $CdSnO_4$ Window Layer Development

Antireflection Coatings for High Efficiency Cells

Basic Measurements
- Optical Characterization of $CuInSe_2$ cell layers
- Spectral Response Enhancements
- Voltage Contrast Imaging
- Variable Temperature and Scanned Photoluminescence
- X-Ray Diffraction Studies
- EXAFS and Raman Spectroscopy

5.0 REFERENCES

1. R. A. Mickelsen and W. S. Chen, "Improved Semiconductors for Solar Cells $CuInSe_2$", Final Report, Contract E(49-18)-2459, August, 1977.

2. R.A. Mickelsen, W. S. Chen, and B. Selikson, "Cadmium Sulfide/Copper Ternary Heterojunction Cell Research," Final Report, Contract EG-77-C-03-1458, October 1978.

3. R. A. Mickelsen and W. S. Chen, "Cadmium Sulfide/Copper Ternary Heterojunction Cell Research", Final Report, Contract XJ-J-8021-1, August, 1982.

4. Y. R. Hsiao, W. S. Chen, R. A. Mickelsen, J. M. Stewart, V. Lowe, L. C. Olsen and A. Rothwarf, "$CuInSe_2$/CdS Thin-Film Solar Cell Development", Final Report, Contract XE-2-02038-1, May, 1983.

5. R. A. Mickelsen, W. E. Devaney, W. S. Chen, Y. R. Hsiao, J. M. Stewart, L. C. Olsen, and A. Rothwarf, "Cadmium Sulfide/Copper Ternary Heterojunction Cell Research", Final Report, Contract ZL-3-02184-1, September, 1984.

6. W. E. Devaney, R. A. Mickelsen, W. S. Chen, J. M. Stewart, L. C. Olsen and A. Rothwarf, "Cadmium Sulfide/Copper Ternary Heterojunction Cell Research", First Quarter Report, Contract ZL-4-04068-1, February, 1985.

7. W. E. Devaney, R. A. Mickelsen, W. S. Chen, J. M. Stewart, L. C. Olsen, and A. Rothwarf, "Cadmium Sulfide/Copper Ternary Heterojunction Cell Research", First Semi-Annual Report, Contract ZL-4-04068-1, April, 1985.

8. W. E. Devaney, R. A. Mickelsen, W. S. Chen, B. J. Stanbery, J. M. Stewart, L. C. Olsen, and A. Rothwarf, "Cadmium Sulfide/Copper Ternary Heterojunction Cell Research", Third Quarter Report, Contract ZL-4-04068-1, August, 1985.

9. W. E. Devaney, R. A. Mickelsen, W. S. Chen, B. J. Stanbery, J. M. Stewart, L. C. Olsen and A. Rothwarf, "Cadmium Sulfide/Copper Ternary Heterojunction Cell Research", First Annual Report, Contract ZL-4-04068-1, November, 1985.

10. W. E. Devaney, R. A. Mickelsen, W. S. Chen, B. J. Stanbery, Y. R. Hsiao, J. M. Stewart, A. Rothwarf. "Cadmium Sulfide/Copper Ternary Heterojunction Cell Research", Fifth Quarter Technical Progress Report, March,1986.

11. W. S. Chen, J. M. Stewart, B. J. Stanbery, W. E. Devaney, and R. A. Mickelsen, "Development of Thin Film Polycrystalline $CuIn_{1-x}Ga_xSe_2$ Solar Cells", Proc. of 19th IEEE Photovoltaic Specialists Conf., 1987, in press.

12. R. A. Mickelsen, B. J. Stanbery, J. E. Avery, W. S. Chen, and W. E. Devaney, "Large Area $CuInSe_2$ Thin-Film Solar Cells", Proc. of 19th IEEE Photovoltaic Specialists Conf., 1987, in press.

13. J. M. Stewart, "Some Health and Safety Concerns in the Research and Production of $CuInSe_2$/CdZns Solar Cells", Solar Cells, 19 237 (1987)

14. R. A. Mickelsen, W. S. Chen, "Development of Thin-Film $CuInSe_2$ Solar Cells", in the Proceedings of the 7th International Conference on Ternary and Multinary Compounds, September, 1986. S. K. Deb & A. Zunger, Eds.; Published by Materials Research, 1987.

15. J. M. Stewart, W. S. Chen, W. E. Devaney, R. A. Mickelsen, "Thin Film Polycrystalline $CuIn_{1-x}Ga_xSe_2$ Solar Cells" in the Proceedings of the 7th International Conference on Ternary and Multinary Compounds, September, 1986. S. K. Deb & A. Zunger, Eds.; Published by Materials Research Society, 1987.

16. W. E. Devaney, R. A. Mickelsen, W. S. Chen, "Recent Improvements in $CuInSe_2$/CdZnS Thin Film Solar Cell Efficiency" Proc. Eighteenth IEEE Photovoltaic Specialists Conference, Las Vegas, NV. (1985).

17. W. A. Miller, "Current Transport in CdZnS/$CuInSe_2$ Solar Cells", Ph.D. Dissertation, Joint Center for Graduate Studies, Washington State University, 1984.

18. M. N. Ruberto, "Transient Capacitance and Open Circuit Voltage Measurements on the $CuInSe_2$/CdS Solar Cell", Masters Thesis Drexel University, 1986.

19. E. C. Demetriou, "Admittance Spectroscopy on $CuInSe_2$/CdS Solar Cells", Masters Thesis, Drexel University, 1986.

20. W. Arnt, H, Dittrich, F. Pfisterer, and H. W. Schock, 6th European Photovoltaic Solar Energy Conference, London 1985, p1.

21. H. Neff, P. Lange, M. L. Fearheiley, and K. J. Bachmann, Appl. Phys. Lett. 47 (10), 15 November 1985, p. 1089.

22. K. J. Bachmann, Annual Report, SERI Contract No. XL4-04041-1, 1986.

23. R. J. Matson, R. Noufi, R. K. Ahrenkiel, R. C. Powell, D. Cahen, Solar Cells, 16, 495, 1986.

24. A. Gopinath et al, "Voltage Contrast A Review," Scanning Electron Microscopy/1978/Vol. 1, pp. 375-380.

25. J. R. Sites, "$CuInSe_2$ Photovoltaic Diodes", Final Report, Contract XF-1-1237-1, June 1984.

26. R. J. Matson, C. R. Herrington, R. Noufi, and R. C. Powell, "EBIC Studies of Junction Formation and the Role of Oxygen in Thin Film CdS/$CuInSe_2$ Solar Cells", Proc. of the 18th PVSC, Las Vegas, NV (1985).

27. F. H. Pollak and R. Tsu, "Raman Characterization of Semiconductors Revisited", Proc. SPIE Vol. 452, F. H. Pollak and R. S. Bauer, eds, pp. 26-43 (1983).

28. J. N. Gan, J. Tauc, V. G. Lambrecht, M. Robbins, Phys. Rev. B13, (1976).

29. P.M. Nikolic, S. M. Stojilovic, Z. Petrovik, M. Dimitrijevick, Proc. VI Yugoslav Symp. Phys. Cord. Matter, 98 (1978).

30. H. Neumann, R. D. Tomlinson, W. Kissinger, and N. Argerinos, Phys. Stat. Solidi B, 118, K51 (1983).

31. G. C. Papavassilou, J. Mol, Struct. 79, 1086 (1983).

32. J. F. Scott and T. C. Damen, Optic Comm., 5,410 (1972).

33. R. Rossetti, S. Nakahara, and L. E. Brus, J. Chem. Phys., 79, 1086 (1983)

34. J. P. Vander-Ziel, A. E. Meixner, H. M. Kasper, and J. A. Ditzenberger, Phys. Rev. B9, 4286 (1974).

35. H. Kunzel and K. Ploog, "The Effect of As_2 and As_4 Molecular Beams on Photoluminescence of Molecular Beam Epitaxially Grown GaAs", Appl. Phys. Letter 37 (4), pp. 416-418.

36. L. W. Kapilar, C. W. Litton, and G. C. Clark, "On the Design and Characterization of a Novel Arsenic Cracking Furnace Utilizing Catalytic Decomposition of AsH_3 to Yield a Purely Monomeric Source of Arsenic for Molecular Beam Epitaxial Growth of GaAs", J. Vac. Sci. Technology B2 (2) pp. 280-284.

37. C. T. Foxon and B. A. Joyce, Surf. Sci 50, 434 (1975); 64, 293 (1977).

38. Jasprit Sirgh, "Role of Arsenic (As_2, As) in Controlling the Quality of GaAs Grown by MBE, Theoretical Studies", J. Vac. Sci. Tech. B2 (2) pp. 276-280.

39. Y. K. Rao, "Composition of Liquid-Saturated Selenium Vapor", Met. Trans. B. (14B), June 1983, pp. 308-311.

40. A. G. Schrott, PhD Dissertation, University of Washington, 1982.

41. W. Simon, International Journal of Mass Spectrometry and Ion Physics, 12 (1973), pp. 159-174.

42. R. P. H. Chang, et al, "Plasma-Enhanced Beam Deposition of Thin Films of Low Temperatures", J. Voc. Sci. Tech B1 (4), pp. 935-942.

43. A. Rockett, et al, "A Low-Energy, Ultrahigh Vacuum, Solid-Metal Ion Source for Accelerated Ion Doping During Molecular Beam Epitaxy", J. Voc. Sci. Tech. B2 (3), pp. 306-313.

44. H. A. Macleod, Thin-Film Optical Filters (American Elsevier Publishing Company, Inc., New York, 1969).

45. O. S. Heavens, Optical Properties of Thin Solid Films (Dover Publications, Inc., New York, 1965).

6.0 Appendices

6.1 Appendix A - Report Distribution List

Scot P. Albright
Photon Energy, Inc.
13 Founders Blvd.
El Paso, TX 79906

Robert H. "Bud" Annan
U.S. Department of Energy
PV Energy Technology Division
Forrestal Building,
1000 Independence Ave., S.W.
Washinton, D. C. 20585

Bulent M. Basol
ISET
8635 Aviation Blvd.
Inglewood, CA 90301

Robert W. Birkmire
Institute of Energy Conversion
University of Delaware
Newark, DE 19716

Eldon Boes
P. O. Box 5800
Sandia National Laboratory
Albuquerque, NM 87185

Richard H. Bube
Dept. of Materials Science & Engg.
Stanford University
Stanford, CA 94305

Ting L. Chu
Electrical Engineering Department
Southern Methodist University
Dallas, TX 75275

Ed DeMeo
P.O. Box 10412
Electric Power Research Institute
Palo Alto, CA 94303

Satyen K. Deb
SERI M/S 16/3
1617 Cole Blvd.
Golden, CO 80401

Walter E. Devaney
Boeing Electronics
High Tech Center
Box 24969, MS 9Z-80
Seattle, WA 98124 6269

Charles F. Gay
ARCO Solar, Inc.
P. O. Box 2105
Chatsworth, CA 91313

Roger B. Gillette
Boeing Electronics
High Tech Center
Box 24969,MS 9Z-80
Seattle, WA 98124

Lloyd Herwig
PV Energy Systems Division
U. S. Department of Energy,
CE 352
1000 Independence Avenue SW
Washington, D.C. 20585

John F. Jordan
Photon Energy, Inc.
13 Founders Blvd.
El Paso, TX 79906

Vijay K. Kapur
ISET
8635 Aviation Blvd.
Inglewood, CA 90301

Larry L. Kazmerski
SERI M/S 16/3
1617 Cole Blvd.
Golden, CO 80401

Richard J. Matson
SERI M/S 16/3
1617 Cole Blvd.
Golden, CO 80401

John D. Meakin
Institute of Energy Conversion
University of Delaware
Newark, DE 19716

Peter V. Meyers
Ametek Applied Materials Lab
352 Godshall Drive
Harleysville, PA 19438

Reid A. Mickelsen
Boeing Electronics
High Tech Center
Box 24969, MS 9Z-80
Seattle, WA 98124 6269

Richard L. Mitchell
SERI M/S 16/1
1617 Cole Blvd.
Golden, CO 80401

Rommel Noufi
SERI M/S 16/3
1617 Cole Blvd.
Golden, CO 80401

James E. Phillips
Institute of Energy Conversion
University of Delaware
Newark, DE 19716

Morton B. Prince
PV Energy Systems Division
U. S. Department of Energy
CE 352
1000 Independence Avenue SW
Washington, D.C. 20585

Ajeet Rohatgi
Georgia Institute
of Technology
Dept. of Electrical Engineering
Atlanta, GA 30332-0420

T.W. Fraser Russell
Institute of Energy Conversion
Univeristy of Delaware
Newark, DE 19716

James R. Sites
Dept. of Physics
Colorado State University
Ft. Collins, CO 80523

Richard J. Stirn
Jet Propulsion Lab
S12-103
4800 Oak Grove Drive
Pasadena, CA 91109

Jack L. Stone
SERI M/S 16/3
1617 Cole Blvd.
Golden, CO 80401

Tom Surek
SERI M/S 16/1
1617 Cole Blvd.
Golden, CO 80401

John A. Thornton
University of Illinois
Coordinated Science Laboratory
1101 W. Springfield Avenue
Urbana, IL 61801

Harin S. Ullal
SERI M/S 16/1
1617 Cole Blvd.
Golden, CO 80401

Ken Zweibel
SERI M/S 16/1
1617 Cole Blvd.
Golden, CO 80401

J.W. "Bill" Yerkes
Boeing Electronics
High Tech Center
Box 24969, MS 7J-06
Seattle, WA 98124-6269

6.2 Appendix B - List of Research Participants

J. E. Avery	-	CIS Cell Fabrication
R. M. Burgess	-	Photoluminescence Measurements
A. F. Burnett	-	Sputtered Film Deposition and Cell Fabrication
W. S. Chen	-	Cell Analysis and Modeling
D. Collier-Kerstetter	-	Cell Patterning and Fabrication
W. E. Devaney	-	Cell Fabrication and Device Analysis
G. Henderson	-	Grid Deposition
C. L. Isakson	-	Device Measurement
F. W. Lytle	-	EXAFS Measurements
R. A. Mickelsen	-	Cell Fabrication and Material Analysis
E. L. Miller	-	Voltage Contrast Measurements
R. A. Murray	-	Film Deposition
B. J. Stanbery	-	Raman Measurements, SE Source and Large Area Cell Development
J. M. Stewart	-	CIGS Film Deposition
G. Wolff	-	Technician

6.3 Appendix C: EXAFS THEORY AND MEASUREMENTS

C-1: Determination of Chemical Composition by X-ray Absorption.

When a beam of monochromatic x-rays passes through a thin layer of material, dx, the fraction of the incident beam absorbed is

$$dI/I = -\mu_L\, dx \qquad (1)$$

where u_L is the linear absorption coefficient. If u_L is constant, integration gives

$$I = I_0 \exp(-\mu_L x) \qquad (2)$$

where x is the thickness, and I, I_0 are the transmitted and incident intensities. This may also be expressed in terms of u, the mass absorption coefficient, where $u = u_L/\rho$ and ρ = density

$$I = I_0 \exp(-\mu\rho x) \qquad (3)$$

or

$$I = I_0 \exp(-\mu C) \qquad (4)$$

where the units are u_L=cm^{-1}, u=cm^2gm^{-1}, xρ=C=gm*cm^{-2}, x=cm and ρ=gm/cm^3.

When an elemental absorption edge is measured the size of the absorption discontinuity is proportional to the amount of that element present in the following way.

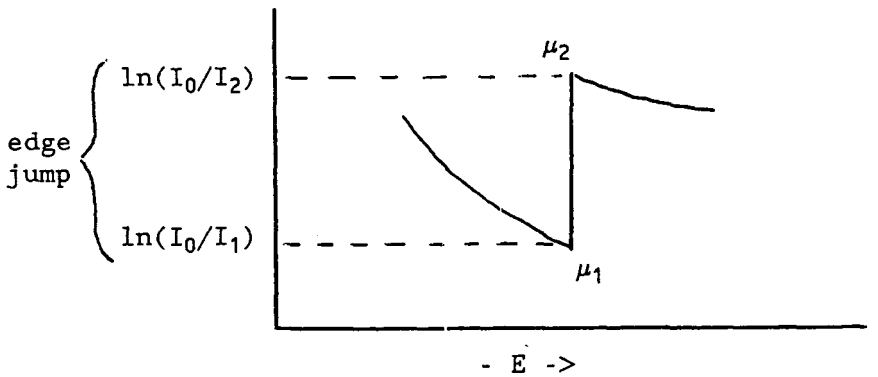

$\ln(I_0/I)$ can be accurately measured and u_1, u_2 are tabulated. Then, since thickness and density are constant over the edge,

$$I_1 = I_0 \exp(-\mu_1 \rho x) \qquad I_2 = I_0 \exp(-\mu_2 \rho x)$$

$$\ln(I_0/I_1) = \mu_1 \rho x \qquad \ln(I_0/I_2) = \mu_2 \rho x$$

$$\text{edge jump} = \ln(I_0/I_2) - \ln(I_0/I_1) = \rho x(\mu_2 - \mu_1)$$

$$\rho x = C = \text{edge jump}/(\mu_2 - \mu_1) \qquad \text{gm cm}^{-2}$$

Conversely, if the thickness or density is known the corresponding quantity may be determined.

As a test case consider the data on a nominal 5 μm thick Cu foil (The true thickness is not known).

$$x = \text{edge jump}/\rho(\mu_2 - \mu_1)$$

$$= 1.24 \; / \; [8.94 \; (288.9 - 37.9)]$$

$$= 5.5 \; \mu\text{m}$$

This method is unique as to the high degree of specificity. There are no corrections to the data necessary for the presence of other elements in the sample. Also the physical state of the sample is immaterial.

The presence of a substrate material makes the measurement of the edge jump less accurate by contributing a high background level of absorption. If too thick, the measurement becomes impossible.

For the available solar cell data on samples 850B and 850C the substrates were too thick to measure the edge jump for any elements except In. The other data on solar cells P548M and P662M was satisfactory except that the absorption data for In was not measured. The following analysis on the Cu, Ga, Se data for P548M and P662M illustrates the technique although In must be obtained by difference.

Table 1 lists the mass absorption coefficient data obtained from the McMaster tables. Table 2 lists the measured edge jumps for the elements Cu, Ga, and Se in solar cells P548M and P662M along with the thickness as obtained by Wen Chen. The absorption cross section was calculated using eq.(4) except for In. If it is assumed that the thickness determination is accurate and the density is equal to that of $CuInSe_2$, ρ=5.77, then the total absorption cross section for each solar cell is ρx or $12.7*10^{-4}$ gm/cm^2 and $20.2*10^{-4}$ gm/cm^2 for P548M and P662M, respectively. The In concentration can then be estimated by difference.

Table 1. Tabulated Absorption Cross Sections*

Element	ρ, gm/cm^3	u_1, cm^2/gm	u_2, cm^2/gm	Δu
Cu	8.94	$3.61*10^1$	$2.87*10^2$	251
Ga	5.90	$2.89*10^1$	$2.14*10^2$	185
Se	4.79	$2.18*10^1$	$1.50*10^2$	129
In	7.28	7.20	$4.51*10^1$	37.9

*W.H. McMaster et.al.,"Compilation of X-ray \Cross Sections", UCRL-50174, May 1969

The cross sections are claimed to be accurate to 1%.

The accuracy of the measured absorption cross section values in Table 2 is about +/- 10% and was limited by the relatively high absorption of the alumina substrate. On a suitably thin substrate the absolute accuracy could be improved to +/- 1%. In order to compare to the EDX chemical analyses we compare the mass fraction by EDX and by X-ray absorption in Table 3. These results must be qualified by the fact that both quantities in the product ρx are not known accurately and the In values were obtained by difference. Note that one additional measurement on In will allow the mass fraction of all the elements to be determined independent of ρx. The high values for Se appear to be significant.

Table 2. Measured Absorption Edge Data

	Edge Jump		Absorption Cross Section, C [gm/cm^2]	
	P548M	P662M	P548M	P662M
Cu	.055	.085	$2.19*10^{-4}$	$3.39*10^{-4}$
Ga	.023	.015	$1.24*10^{-4}$	$0.81*10^{-4}$
Se	.100	.148	$7.75*10^{-4}$	$11.5*10^{-4}$
In	not determined		Areal Density $1.51*10^{-4}$ (estimated by difference)	$4.50*10^{-4}$
Thickness, x*	2.2μm	3.5μm		
Areal Density			$12.7*10^{-4}$ (determined from product, ρx using ρ=5.77 gm/cm^3)	$20.2*10^{-4}$

* supplied by Wen Chen

Table 3. Comparison of Chemical Analysis by EDX and X-ray Absorption

	MASS FRACTION			
	by EDX		by X-ray Absorption	
	P548M	P662M	P548M	P662M
Cu	.184	.184	.17	.17
In	.188	.296	.12	.22
Ga	.122	.0504	.098	.041
Se	.505	.469	.61	.57

C-2: Elemental Depth Profile by X-ray Absorption Spectroscopy

In addition to normal transmission mode X-ray absorption spectroscopy the sample may be rotated to a position which is at an angle to the X-ray beam. Then the fluorescent X-rays or electrons emitted from the surface can be measured. Both signals will be proportional to the X-ray cross section and have the useful property that they probe different sample

depths. Fluorescent X-rays sample the entire X-ray penetration depth and are a very useful method to obtain data on thick samples. The technique is illustrated in Fig.1. Detection limits of 10^{13}-10^{14} atoms/cm^2 are possible.

It is possible to combine fluorescent X-ray detection with electron-yield detection using the detection scheme shown in Fig.2. The face of the sample is enclosed within a He-filled chamber which has a grid for detecting electrons. Electrons arise from a thin layer of the sample surface as shown by the "Universal Curve" of range vs energy in Fig.3. Furthermore electrons of different energies have different ranges, hence sampling depths. The electron spectrum emitted from a thick sample consists of a few high energy electrons from Auger and photoelectric events and a flood of low energy, inelastically scattered (a few eV) electrons. From Fig.3 note that the lowest energy electrons have ranges of ~100 A, while electrons of 10-500 eV have a range 210 A. It is possible to operate the detector to take advantage of this range vs energy phenomenon. Changing the bias on the collecting grid from positive to negative will collect only positive He ions. Since the He ions can be created only by electrons with sufficient energy to exceed the ion pair production energy of 30 eV, a much thinner surface layer of the sample can be measured.

For the elements Cu, Ga, and Se solar cells P548M and P662M were measured by absorption (A), fluorescent X-rays (F), total electron yield (e) and positive He ion yield (p). We used this data to obtain a rough profile of each element within the solar cells. For these 2.2-3.5μm thick cells the A and F techniques sample the entire cell with no appreciable differences expected between them. It was shown above that the absorption jump as measured by A could be used as a measure of the total amount of the element present. A similar determination could be made with F of corrections were made for the self absorption by all the elements in the sample of the fluorescent X-rays detected in the measurement as is done in the usual X-ray techniques for chemical analysis. Similar theories for electrons of various energies could also be developed but would require an accurate knowledge of the electron spectrum and distribution of elements in the sample. However, without this knowledge it is still possible to use the e and p data in the qualitative sense of Fig.3 and detect non-uniformity in depth of specific elements within the top tens (p) or hundreds (e) of Angstroms of the sample surface.

The data is given in Table 4 where each edge jump has been normalized by the respective transmission mode edge jump in order to remove the concentration difference between the two

solar cell samples. If data was available on a reference compound near to the composition of the solar cells and of uniform composition throughout then the values in Table 4 could be placed upon an absolute basis. As it is the uniform trend of edge jumps greater than that of the A technique simply reflects the generally increased sensitivity of the F, e and p techniques. Since solar cell P548M appears to be generally more uniform in composition than P662M, and in the absence of absolute standards, the ratio P662M/P548M is calculated in order to demonstrate the non-uniformity with depth of the samples, particularly P662M.

Table 4. Normalized Absorption Edge Jumps For Absorption(A), Fluorescence (F), e-yield (e) and Positive Ion Yield (p).

Element	Measurement Technique	Normalized Edge Jump P548M	Normalized Edge Jump P662M	Ratio P662M/P548M	Mass Fraction Ratio
Cu	A	1	1	1	1.0
	F	10.7	13.8	1.3	
	e	15.0	9.6	.64	
	p	11.9	11.9	1.0	
Ga	A	1	1	1	.41
	F	13.6	8.2	.60	
	e	3.4	2.6	.76	
	p	2.9	2.0	.69	
Se	A	1	1	1	.93
	F	3.3	3.9	1.2	
	e	3.4	5.7	1.7	
	p	2.7	.52	.2	

This is shown graphically in Fig.4 where the ratio P662M/P548M is plotted vs the log of the escape depth approprite for the e and p techniques. The escape depth can be roughly identified as depth below the solar cell surface. Se has the largest concentration variation. P662M is Se depleted near the surface and significantly enriched ~100 A deep. The average concentration (mass fraction) ratio as determined by EDX is also given in Table 4 and indicated in

Fig.4. It is clear that the technique is sensitive to significant changes in element concentration in the region near the surface.

C-3: Recommendation

Even in the absence of complete data on the solar cell samples or of good data on adequate reference standards, this discussion illustrates the utility of the technique for absolute chemical analysis and for depth profiling of element concentration. The following recommendations for future work would place the technique on an absolute basis as to element concentration and depth sampled by the various techniques:

1. Obtain data for all elements present in stochiometric, uniform $CuInSe_2$, $CuIn_xGa_{1-x}Se_2$ etc.
2. Prepare thin sample of each element covered by overlayers of known thickness of the other elements so that escape depths can be measured for the e and p techniques.

C-4: Determination of Structure Parameters with the EXAFS Technique: Introduction

The separation in energy of the core level absorption edges for different elements allows the separate determination of structure for each of the separate elements on a complex material such as $CuInSe_2$. A good critical review of the EXAFS method is that of Lee et al (1). During the x-ray absorption event the ejected photoelectron can backscatter from nearby atoms with an neutral state-scattered state interference. This interference is the cause of the extended x-ray absorption fine structure (EXAFS). In the single scattering approximation the EXAFS function is:

$$X(K) = \sum_j A_j(K) \sin[2KR_j + \delta_j(K)] \qquad (1)$$

Where the summation extends over j coordination shells. K is the photoelectron wave vector, $K = 2\pi/\lambda_j$; R_j is the distance from the absorbing atom to the atoms on the jth shell and $\delta_j(K)$ is a phase shift due to the fact that the photoelectron is traversing the potential wells of both the absorbing and scattering atoms . The factor $A_j(K)$ is an amplitude factor for the jth shell and contains

$$A_j(K) = (N_j/KR_j^2)F_j(K) \exp(-2\sigma_j^2K^2) \qquad (2)$$

where N_j is the number of atoms in the jth shell, σ_j is the root mean square deviation of the outeratomic distance about R_j and $F_j(K)$ is the electron backscattering function for the jth atom. $F_j(K)$ depends on the kind of atom responsible for the scattering and allows the identification of the kind of atom creating the EXAFS scattering. It is equal to the overall envelope of the EXAFS function. Fourier transformation yields

$$\Phi_n(R) = (1/2\pi)^{1/2} \int_{K_{min}}^{K_{max}} K^n X(K) \exp(2iKR)dK \qquad (3)$$

$\Phi_n(R)$ is like a radial distribution function modified by the $1/R^2$ term. The K^n weighting term allows emphasis of either the low K or high K part of the data. $\Phi_n(R)$ has peaks located at the radial distances of the atoms in the structure minus a phase shift which was not included in the Fourier transform. It is useful to select a region of the transform, the first coordination shell for example, and back transform it to K-space. This function has the more simple representation.

$$K^nX_1(K) = K^nA_1(K) \sin [2KR_1 + \delta_1(K)] \qquad (4)$$

where subscript 1 refers to the first coordination shell. This function can be fit to the back transformed data when A(K) and $\delta(K)$ are known. To a good approximation each kind of atom will always scatter the same so the A(K) function may be determined from reference materials containing the desired backscattering atom. The phase shift $\delta(K)$ contains a part due to both the (a) absorbing and (b) backscattering atoms so that

$$\delta_{(ab)} = \delta_a + \delta_b$$

This term can also be evaluated from a reference compound which contains the a-b bond.

Experimental determination of A(K) and $\delta(K)$ from compounds near to the composition of the unknown produces the most accurate determination of structure parameters. In the absence of an experimental determination Teo and Lee (2) have calculated and tabulated these quantities for all the elements.

C-5: Analysis of Solar Cell EXAFS Data

Our initial data represents a cursory effort in very limited

time in an attempt to demonstrate experimental feasibility. It should not be viewed as the optimum possible with carefully chosen reference compounds and solar cell samples. Table 5 is a matrix listing the samples, the type of EXAFS measurement and the elements measured to date. We are most limited now by the one type of measurement on the small piece of $CuInSe_2$ Crystal. Our highest priority in future measurements is good data on a suite of reference compounds.

TABLE 5: Matrix of XAS Measurements to date

	Type of Measurement				
Sample	A	F	e	p	Elements
850B	*In Only	X	-	-	Cu, In, Se
850C	*In Only	X	-	-	Cu, In, Se
P548M	X	X	X	X	Cu, Ga, Se, no In**
P662M	X	X	X	X	Cu, Ga, Se, no In**
$CuInSe_2$ crystal	-	X	-	-	Cu, In,Se

* Substrate too thick for other elements

** Requires different monochromator crystal than was available at the time.

The analysis proceeds by first placing the absorption spectrum on the energy scale of the photoelectron, i.e., $E_{x\text{-}ray}-E_K$ = Energy where E_K is the core level bonding energy. The K-absorption spectrum for Cu metal is shown in Figure 5A. In order to normalize the data to a per atom basis and extract the X(K) function a curve-following spline routine is drawn through the EXAFS to approximate the slope of the absorption curve. It is then subtracted from the EXAFS wiggles producing a function which oscillates about zero which is then divided by the edge jump and converted to K units, $K = 2\pi(2mE)^{1/2}/h$. Thus

$$X(K) = (\mu-\mu_o)/\mu_o$$

Where μ_o represents the absorption of the free atom without any near neighbors. The edge jump and near edge are obtained by extrapolating the pre-edge curve underneath the absorption edge and evaluating the edge jump at E=0. The edge jump is the vertical jump between the pre-edge extrapolation and the spine curve through the EXAFS. The near edge curve is obtained by subtracting the curve defined by the pre-edge extrapolation and dividing by the edge jump. This results in a near edge curve which always has an edge jump of unity. The Cu EXAFS is shown in Fig. 5B. Near edge data of the Cu edge on solar cells is shown in Fig. 6.

The Fourier transform is then observed as in eq. (3) resulting in Figs 5C and 6. The coordination number and disorder are contained in the relative amplitudes and modulation of the EXAFS function. In order to see the effect of coordination number (3) note the data in Fig. 7 where the coordination number changes from 2 for Se to 4 for Ge to 8 for Fe and 12 for Ni. The effect of thermal disorder (4) is shown by the EXAFS transforms and first shell back transforms for Cu as a function of temperature in Fig. 8. From a series of measurements as a function of temperature the thermal disorder of a sample can be determined and separated from static disorder (5).

The reverse transform of the first radial distribution peak produces a damped sine wave which can be fit to eq. (4) using an interactive non-linear, least squares fitting routine. Examples of fits to the solar cell data are given in Figs. 9 and 10. Note that the Se data (bottom, Fig. 10) was fit with the sum of 2 Cu at 2.40 and 2 In at 2.61A.

Data for elemental Se, Cu and In were used for F(K). The phase shifts Cu-Se, In-Se, Ga-Se, Se-Cu, Se-In and Se-Ga were obtained from the calculated values of Teo and Lee (2). A selection of these are shown in Fig. 11. These limit the accuracy of the bond distance determination to $\pm$.04A absolute and $\pm$.01A, relative. Accurate, experimental phase shifts could improve this to $\pm$.01A absolute and $\pm$.005A relative. The fitting results for the solar cell data are summarized in Table 6. The bond distance values are near to those reported for $CuInSe_2$ (6) where Cu-Se = 2.40, In-Se = 2.60, and Cu-In = 4.08A. There is an indication that introduction of Ga increases all the bond distances slightly. The disorder results show that all of the bonds in 850C, which was annealed in 0_2 at 225°C for 20 min., are slightly more disordered than in 850B. This could be the result of an

oxide phase disrupting the lattice. Since it would be expected to be more concentrated on the surface e and p measurements might detect it.

Table 6: Results of Fitting Preliminary EXAFS Data With Calculated Phase Shifts

Sample	Bond Type	Coor. No*	Bond Distance, A**	Relative Disorder, A^2
850B	Cu-Se	4	2.41±.04A	.00282^s
	In-Se	4	2.61	- .00057^s
	Se-Cu	2	2.40	- .00587^c
	Se-In	2	2.61	- .0155^i
850C annealed in O_2	Cu-Se	4	2.41	.00305^s
	In-Se	4	2.61	- .00015^s
	Se-Cu	2	2.40	- .00584
	Se-In	2	2.62	- .0148^s
P548M	Cu-Se	4	2.42	.00274^s
	Ga-Se	4	noisy data	
	Se-Cu,In,Ga	not possible to fit with available reference data		
P662M	Cu-Se	4	2.42	.00286^s
	Ga-Se	4	2.43	- .00097^s
	Se-Cu,InGa	not possible to fit with available reference data		

* Stochiometric value of coordination number was assumed

** The error of ±.04A is absolute error. Relative error is ±.01A

s Disorder relative to Se-Se bond in hexagonal Se at 25°C.

c Disorder relative to Cu-Cu bond in Cu metal at 25°C.

i Disorder relative to In-In bond in In metal at 25°C.

Examples of the Fourier transforms for each element in the solar cells are given in Figs. 12 and 13. In Fig. 12A it is evident that the presence of Ga in the cell greatly decreases the height of the 2nd coordination shell of Cu. This peak at

~4A is due to In and Ga (when present in the sample) neighbors. The difference in the bond lengths Cu-In and Cu-Ga introduces static disorder which causes the peak to decrease. The split Ga peak in Fig. 12B is the result of noisy data which can be improved upon. The complicated Se peak in Fig. 13A is the result of two different bond lengths in the 1st coordination shell to Cu and In as noted. The back transform of this peak was fit in Fig. 10 bottom. The lack of 2nd neighbor peaks around In (Fig. 13B) and Ga (Fig. 12B) is the result of structural disorder. Measurements as a function of temperature could separate this into its thermal and static components.

It is clear that the element by element structural investigation possible with EXAFS results in incredible structural detail. But what does it all mean? Beginning the investigation it is not possible to yet predict the sensitive parameters related to solar cell performance. But rest assured, new data will eventually result in increased understanding. Solar cells work because of their band structure. The arrangement of atoms determines the band structure.

C-6: Recommendations for Future Work

The first measurements should be complete A,F,e and p type data for all reference compounds. Samples on hand and their diffraction results are shown in Tables 7 and 8. Also data will be obtained for metal In and Ga, samples of which are available. This suite of data will allow more accurate evaluation of solar cell data on hand plus all future data.

Three types of measurements on solar cells would be informative.

a) A depth profile survey for solar cells selected for a range of performance variables.

b) A measurement of EXAFS as a function of temperature for each of the elements in a solar cell, perhaps comparing one with Ga and one without. This will allow determination of thermal and static disorder.

c) A depth profile and characterization of the Mo layer on the back side of the solar cell. Strip the active layer from the alumna and then examine both surfaces.

Table 7: Comparison of Measured X-Ray Diffraction Parameters with Powder File Data

Cu_2Se

File		Measured (6-06801)	
d	I	d	I
3.31	.80	3.33	.9
		2.88	.1
2.03	1	2.02	1
1.73	.30	1.729	.8
1.44	.10	1.434	.3
1.32	.07	1.317	.2
1.173	.13	1.171	.4
1.105	.05	1.105	.2

Ga_2Se_3

File		Measured (5-0724)	
d	I	d	I
3.14	1	3.14	.8
2.73	.07	2.70	.1
1.91	1	1.919	1
1.64	.29	1.639	.8
1.35	.10	1.354	.4
1.25	.10	1.244	.6
		1.211	.1
1.107	.10	1.106	.8
1.047	.06	1.046	.6

In_2Se_3

File	
d	I
4.77	.91
3.44	.41
3.12	1
2.64	.26
2.21	.35
2.08	.35
2.00	.70
1.85	.24
1.76	.15
1.69	.18

Table 8: Measured X-Ray Diffraction Parameters for Cerac $CuInSe_2$ and two Solar Cells

$CuInSe_2$		P548M		P662M	
d,A	I	d,A	I	d,A	I
3.31	1	3.28	1	3.32	1
		2.23	.41	2.23	.37 ?
2.03	.52	2.00	.41	2.03	.27
1.735	.29	1.712	.20	1.732	.15
1.441	.07	1.575	.07	1.431	.04
1.322	.09	1.280	.11	1.313	.05
				1.278	.04
		1.232	.06	1.232	.03
1.176	.11	1.152	.06	1.166	.05

? This line is not explained. It is not from the alumina backing.

References:

1. P. A. Lee, P. H. Cotrin, P. Eisenberger, and B. M. Kincaid, Rev. Mod. Phys. 53, 769 (1981).

2. B. Y. Teo and P. A. Lee, J. Am. Chem. Soc 100, 2815 (1979)

3. F. W. Lytle, D. E. Sayers and E. A. Stern, Phys. Rev B11, 4825 (1975).

4. R. B. Gregor and F. W. Lytle, Phys. Rev B20, 4902 (1979).

5. E. C. Morques, D. R. Sandstrom, F. W. Lytle and R. B. Gregor, J. Chem. Phys. 77, 1027 (1982).

6. R. W. G. Wyckoff, "Crystal Structures", Vol. 2, P338 Interscience, 1963.